Experimental studies of microplasmas from diamond substrates

Thesis

Experimental studies of microplasmas in diamond substrates

Department of Physical Sciences

Faculty of Science

The Open University

Milton Keynes

United Kingdom

MK7 6AA

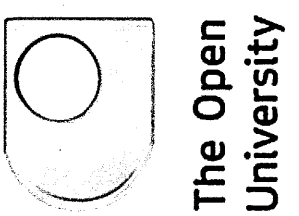

Thesis submitted by

Sébastien Mitea, BSc (Honours)

for the degree of

Doctor of Philosophy

September 2014

DATE OF SUBMISSION : 30 SEPTEMBER 2014

DATE OF AWARD : 4 AUGUST 2015

ProQuest LLC.
789 East Eisenhower Parkway
P.O. Box 1346
Ann Arbor, MI 48106 – 1346

Abstract

The birth of the new field of Microplasma Physics, at the turn of the century, follows decades of miniaturization of plasma sources. The empirical Paschen law from the early twentieth century ensures that increasing the pressure allows a reduction in the reactor dimensions and vice versa. However stable operation of a direct current microscopic discharge had been elusive, until the end of the 1990s.

At microscopic dimensions the importance of surface reactions is magnified, emphasizing the role of the reactor materials. Diamond, obtained synthetically by Chemical Vapour Deposition, offers unprecedented versatility and robustness. By selecting, during deposition, between insulating and semiconducting thin films, diamond-based micro-reactors were fabricated and operated for the first time. The ignition conditions were similar to results reported with other microplasma sources, in argon and helium at pressures ranging from a few torr to atmospheric pressure. The same abnormal and normal glow modes were obtained by comparing the V-I characteristics with those obained with more common microplasma reactor materials.

The dielectric spacer was shown to drive heat transfer through the reactor. Its role on the microplasma was studied via gas temperature measurements. Measurements in diamond were compared with glass-based results. Occupying opposite ends of the thermal conductivity spectrum, they led to significantly different results. Owing to the excellent thermal conductivity of diamond, gas temperature decreased with reactor diameter. That is, heat transfer through the dielectric pre-

vailed over that through the gas phase. To the contrary, glass-based microdischarges were hotter at smaller diameters, when heat conduction through the dielectric was too poor.

Finally, diamond outlived glass and is poised to become a material of choice for microplasma research. Indeed, no diamond-based reactors suffered any failure from the microplasma operation, showing signs of long lifetime.

Contents

List of Figures

List of Tables

Acknowledgements

The journey to the present thesis was demanding on several fronts and rewarding on many others. Never have I received so much support and kindness and never have I failed so much to show my gratitude and return my attention. Completing this thesis is my first, modest acknowledgement of all the efforts and sacrifices that were made *around* but not *by* me.

I will start by expressing my gratitude to and admiration for my supervisors Mark Bowden and Prof. Nicholas Braithwaite for their patience, unwavering support and flexibility in all situations.

I am especially grateful for the precious advice offered by Yvonne Sutton.

I would like to thank my consortium partners Paul May, Neil Fox, Judy Hart, Monika Zeleznik, Robert Stevens and Chantal Fowler for making it possible.

I thank my fellow students, office and lab mates for making the experience simultaneously more fun and more profound: Maria Duffy, Danny Barthaud, Vicky Bending, Ziad El Otell, Chris Mansell, Vytas Masteika.

I feel forever indebted to my parents, Marie-Claire, Sam & Arlette, Jonathan & Jennifer, Thomas for ensuring that my absence was felt a bit less at home.

Simultaneously I owe an immense gratitude to those who ensured that I felt at home in Milton Keynes: Chris Nelson and his family, Pooja Sinha, Sunitha Pangala, Ani, Zdeněk Mašín and Gemma Emerton.

Juan Pablo Llaguno, for our discussion on our way to Trafalgar Square, that day in 2009.

Finally, my deepest gratitude and admiration go to Audrey Magal and Hannah Mitea for their amazing patience and understanding. This thesis is dedicated to them.

Chapter 1

INTRODUCTION

For more than a century, research into plasmas and gas discharges has enriched scientific understanding and driven significant technological progress. This promises to continue with the advent of miniaturized plasma sources, called *microplasmas* or *microdischarges*. This chapter provides a concise introduction to the field of plasma physics and sets the scope for the research reported in this thesis.

The chapter is divided as follows. Section 1.1 briefly describes the plasma and its research context. Fundamental concepts are introduced in Section 1.2 *Plasma Physics*, with the microplasma studies in mind. Section 1.3 *Microplasma Physics and Recent Research* discusses this emerging field and the background to the current research. This introduction finally outlines the main topic of this thesis: *Diamond-Based Experimental Studies* of microplasma.

1.1 What Is a Plasma?

A plasma is an ionized gas, which can occur in stars, fusion reactors as well as discharge light tubes, barcode scanning devices, plasma television pixels,... to name just a few. This vast parameter space is of particular interest to this work. Those examples range from astronomical expanses down to microscopic volumes. Similarly,

gas temperatures can be a few Kelvin for cryoplasmas [Noma et al., 2008] to solar values. Despite tightly limiting dimensions, the realm of microplasmas offers a rich interplay of scientifically fascinating interactions. Some basic classification will help appreciate them.

The *plasma* is defined as a quasi-neutral ensemble of charged particlces in dynamic equilbrium within a neutral gas environment. The *ionization fraction*, x, quantifies the fraction of charged and neutral particles (n_g):

$$x = \frac{n_i}{n_g + n_i} \tag{1.1}$$

with the density of ions, n_i, assumed to be equal to the electron density, n_e. In the first two highest energy examples above, x approaches 1. But in the electrical discharges of interest to us, it can be as low as 10^{-5}. An example is the CF_4 plasma used to etch silicon for microelectronics fabrication [Lieberman and Lichtenberg, 2005]. The central role of the charged particles is obvious from the fact that mostly neutral systems behave as a plasma.

A critical distinction exists between the different sources of energy to ionize (some of) the gas atoms. The fusion plasmas in the introductory paragraph derive this energy from intense heat. As a result, very energetic collisions cause a high level of ionization and perfect coupling between all species, charged or not. In our laboratory gas discharges the main mechanism for plasma ignition is the ionization collisions with neutral atoms of electrons accelerated in the applied electric field. The higher mobility of electrons leads to a very different distribution of energy among all particles.

Further differentiation of electrical discharges is associated with a custom in the

usage of energy units. It is conventional to express the energy of a charged particle in electronvolts (eV). To a temperature T in K corresponds an energy equivalent k_BT — with Boltzmann's constant, $k_B = 1.38 \times 10^{-23}$ J K^{-1}. From the correlation $eV = k_BT$, 1 eV is therefore associated with $T = 11605$ K. Conversely a temperature can be expressed in eV. For room temperature this gives $k_BT_{\text{room}} = 0.026$ eV. Only a factor of e distinguishes between a particle distribution described in eV or V. The former is often simply referred to as a voltage and is the adopted standard in this work.

Two representative types of plasma are the arc and the glow discharge. The former encompasses among other things lightning, arc welding devices and sparks. Due to a single temperature for electrons, ions and neutrals, it is labelled *thermal*. The latter, found in discharge tubes, is reminiscent of the natural glow of Northern (or Southern) Lights or Aurorae Borealis (or Australis). In these cases the electron energy ranges from a few eV to the applied voltage whereas ions and neutrals maintain temperatures below a couple thousand Kelvin. This state of affairs is referred to as a *non-equilibrium* or *non-thermal* plasma.

The non-thermal *glow discharge* is a case study in the organization of the electric field in the bulk and at the boundary of the plasma. It was first obtained by passing current through low pressure gas tubes. Early versions of these discharge tubes were called Geissler tubes, after the German glass-blower who invented them in 1855 [Kitsinelis, 2010a]. This development triggered intensive studies in gas discharges. The neon tubes used for brightly lit outdoor signs can be thought of as their modern equivalent.

The characteristic geography of the glow discharge consists of bright and dark regions, represented in Fig. 1.1 from [Braithwaite, 2000]. The products of ionization and excitation reactions emit light when the parent atoms return to lower energy

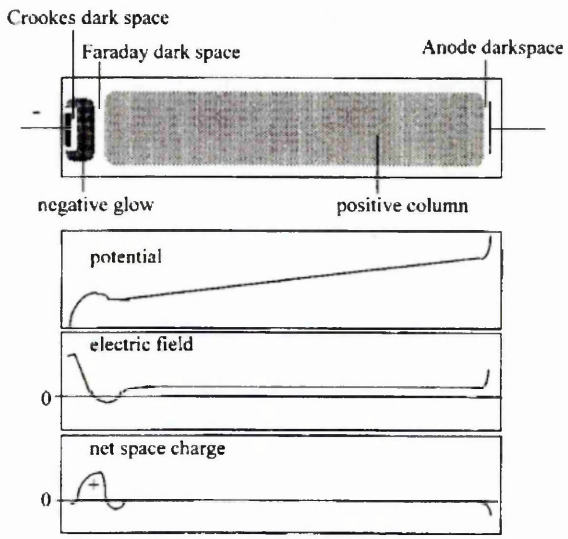

Figure 1.1: The structure of a glow discharge; with the shading intensity matching the light intensity [Braithwaite, 2000].

levels. The visible structure therefore maps the space charge regions, as explained below and illustrated in the graphs under the figure. The ignition and sustainment of a direct current (DC) glow discharge were described by [Townsend, 1900] in terms of:

- the exponential increase — so-called *avalanche* — of electrons resulting from ionization collisions in the inter-electrode gap
- the electron emission induced by ion-bombardment of the cathode

Most of the potential drop between the electrodes actually occurs in the dark region called the *cathode fall* or *sheath*[1]. The resulting high electric field causes a significant increase in electron energy. The exponential density of positive ions peaks at the edge of the sheath. Inside the high field sheath, high velocity electrons (ejected from the cathode) and ions (about to bombard the cathode) can hardly recombine. In the adjacent *negative glow*, intense ionization-recombination and excitation-relaxation take place; explaining its brightness. In the *Faraday dark space*, the build-up of negative space charge and ensuing increase in electric field

[1]Termed the Crookes dark space in Fig. 1.1.

magnitude is necessary to re-accelerate the electrons and sustain the next region. The *positive column* is a uniform, quasi-neutral region. It will expand as long as the electrodes are spaced out, provided that the voltage is sufficient to sustain it. The situation is different when the electrodes are brought too close together. The electrode sheaths persist and the negative glow tends to remain the same size; irrespective of the separation. However the positive column can be confined so much that it ceases to exist. The *anode fall* conserves electrons inside the plasma, only allowing the most energetic ones to the anode; ensuring the viability of the quasi-neutral plasma. Understanding plasma phenomena therefore requires consideration of self-organization together with the role of the confining boundaries.

Going back through history, basic and applied plasma physics research have been closely linked. The "father" of the field, Irving Langmuir, was the first to "use the name *plasma* to describe this region containing balanced charges of ions and electrons" [Langmuir, 1928]. He was then working at the General Electric Company on improving the incandescent lamp through the use of noble gas. Earlier, the inventor of that lamp in 1879, Thomas Edison, had himself stood on the shoulders of giants in the area of ionized gases generated by thermionic emission [Kitsinelis, 2010b]. Sir Humphrey Davy's spectacular first demonstration of the arc plasma between two carbon rods in 1801 in front of the Royal Society had led to the birth of electrical lighting.

More recently, microelectronics and the whole of Information Technology were made possible thanks to an improved understanding of plasma physics. The study of materials processing with plasma (e.g. etching, sputtering and thin film deposition) is epitomized by the standard work "Principles of plasma discharges and materials processing" by [Lieberman and Lichtenberg, 2005]. The importance of these topics is confirmed by the adoption of this book as the reference for students and researchers alike.

This section put the plasma into context and described some conventions about its constituting particle populations. One of several types of discharges, the structure of the glow discharge was introduced. A brief history of plasma physics and its impact on science and technology finally set the stage for the current research.

1.2 Plasma Physics

The theoretical framework will now be laid out for later scientific discussions. Key plasma physics concepts are explained, with definitions and figures taken from the aforementioned reference ([Lieberman and Lichtenberg, 2005]), unless otherwise stated. The objective is to inform the subsequent introduction to microplasma physics. Gas phase reactions are introduced, followed by surface interactions and ending with charged particles behaviours. In each case the focus is on the regimes of relevance to microplasma physics.

1.2.1 Gas Phase

A discussion on plasma physics is aptly started with the kinetic theory of gases. The number density of non-interacting particles described by a Boltzmann distribution is given by

$$n_g = \frac{133\,p}{k_B T} \tag{1.2}$$

where, from now on, the pressure, p, is expressed in torr. For typical pressures between 1 torr and 760 torr (atmospheric pressure) at room temperature, $T = 300$ K, the gas density is 3×10^{22} m^{-3} $< n_g <$ 2×10^{25} m^{-3}. The charged particle population originates from this neutral population.

The average distance between collisions, or *mean free path*, is given by

$$\lambda_{\mathrm{el}} = \frac{1}{n_g \sigma} \tag{1.3}$$

for the case of a point-size particle colliding with a gas atom and

$$\lambda_{\mathrm{el}} = \frac{1}{4 n_g \sigma} \tag{1.4}$$

for the case of similar sized atoms colliding. Elastic collisions are assumed here between hard spheres of cross-sectional area $\sigma = \pi r^2$ and radius r. The factor of four is required to account for the size of the projectile atoms as well as the targets [Braithwaite, 2000]. Substituting for n_g above and the radius of an argon atom, $r = 1.5 \times 10^{-10}$ m, yields $0.1\ \mu\mathrm{m} \lesssim \lambda_{\mathrm{el}} \lesssim 100\ \mu\mathrm{m}$ for the pressure regimes of interest to microplasma research. The micrometer therefore seems like an appropriate scale to describe interatomic collisions in this thesis.

The frequency of interatomic collisions can now be calculated, making use of the mean speed of atoms

$$\bar{v} = \sqrt{\frac{8 k_B T}{\pi M}} \tag{1.5}$$

Inserting the value for the mass of argon atoms, $M = 40 \times 1.67 \times 10^{-27}$ kg, yields $\bar{v} \approx 4 \times 10^2\ \mathrm{m\ s^{-1}}$. The collision frequency takes the form

$$\nu = \frac{\bar{v}}{\lambda_{\mathrm{el}}} \tag{1.6}$$

with values of 4 MHz at 1 torr and 3 GHz at atmospheric pressure.

There follows from the above that the operating pressure and power affect the spatial distribution of a plasma. The collisions inside a gas discharge will generate

heat. Once a temperature gradient is established, the gas density will vary and result in a local pressure gradient. In a gas this translates into a flow of particles. The spatial distribution of the plasma will therefore be determined by the input power and the operating pressure.

The various relevant types of interactions between particles are now presented. Binary collisions are by far the most common, the type of which determines the energy and distributions among the electrons, ions and neutrals [Chapman, 1980]. In *elastic* collisions, an electron can transfer a maximum fraction of 10^{-4} of its energy to an atom. But an atom can transfer all of its kinetic energy to a similar mass atom. In *inelastic* collisions an electron can transfer virtually all of its energy to an atom whereas two atoms can exchange at most half of their kinetic energy. The identity of the interacting particles is therefore as important as their respective energies. This leads to the next topic on the origin and fate of the charged particles.

The main **sources of charged particles** of interest to us are as follows:

1. *Electron-impact ionization* is the major source. An electron transfers energy into the creation of another electron, expressed by

$$e^-_{\text{fast}} + \text{Ar} \rightarrow \text{Ar}^+ + 2e^-_{\text{slow}} \tag{1.7}$$

with typical ionization energies of a few tens of eV; e.g. 15.7 eV for the case of argon.

2. *Metastables* are excited atoms for which electric dipole radiation[2] is forbidden. These are excited by a combination of direct electron impact

$$e^-_{\text{fast}} + \text{Ar} \rightarrow \text{Ar}^* + e^-_{\text{slow}} \tag{1.8}$$

[2]by far the dominant de-excitation mechanism at low pressure and still important in higher pressure systems.

and relaxation reactions in which atoms in higher energy states relax into their metastable levels. With their relatively long lifetimes (milliseconds to seconds) they offer a two-step ionization alternative, called *Penning ionization.* An atom, A, and a metastable, B*, interact to ionize the former, as in

$$A + B^* \rightarrow A^+ + B + e^- \tag{1.9}$$

Metastables can also be ionized by electron impact in a similar process to that shown in Eq.1.7. They are obviously closer to their ionization threshold than ground state atoms. Examples of energy thresholds are 11.5 and 11.7 eV in argon.

3. *Photoionization* by a photon with energy $h\nu$ is expressed by

$$A^{(*)} + h\nu \rightarrow A^+ + e^- \tag{1.10}$$

with typical energies in the ultraviolet band.

(4.) *Charge transfer* is an important process in which an electron from a neutral atom transfers to a positively charged ion by collision of the latter with the neutral atom

$$A + A^+ \rightarrow A^+ + A \tag{1.11}$$

The rate at which this reaction occurs increases with pressure but it does not result in the net creation or loss of charge.

The **loss of charged particles** is dominated by the following reactions:

1. *Three-body recombination* is the process whereby ions and electrons recombine

via collision with a third body

$$e^- + A^+ + M \rightarrow A + M \tag{1.12}$$

where M is required for conservation of momentum. The third body might also be a surface atom facing the plasma, in which case the reaction is written

$$e^- + A^+ + S \rightarrow A + S \tag{1.13}$$

The surface reaction occurs at a much higher rate than the volume process; all incoming positive ions in the energy range 10–1000 eV are neutralized.

2. *Radiative recombination* is a similar process, in which the extra energy and momentum are carried away by a photon:

$$e^- + A^+ \rightarrow A + h\nu \tag{1.14}$$

It is however so unlikely that it is usually ignored.

The above reactions are ranked according to their *rate coefficients.* This is related to the cross-section, which was simplified to the cross-sectional area of the atoms, σ (Eq.1.4 on page 17). However charged particles add an element of probability. For instance, the outcome of electron impact (elastic or excitation/ionization collisions) depends on its kinetic energy (for the reaction timescale) and the local electric field (for its final approach).

The *rate coefficient* incorporates an effective cross-sectional area and the particle velocity. The collision frequency (Eq.1.6) can be expanded to

$$\nu = \frac{v}{\lambda_{el}} = n_g \, \sigma \, v$$

where the mean free path Eq.1.3 was taken in order to focus on electron projectiles.

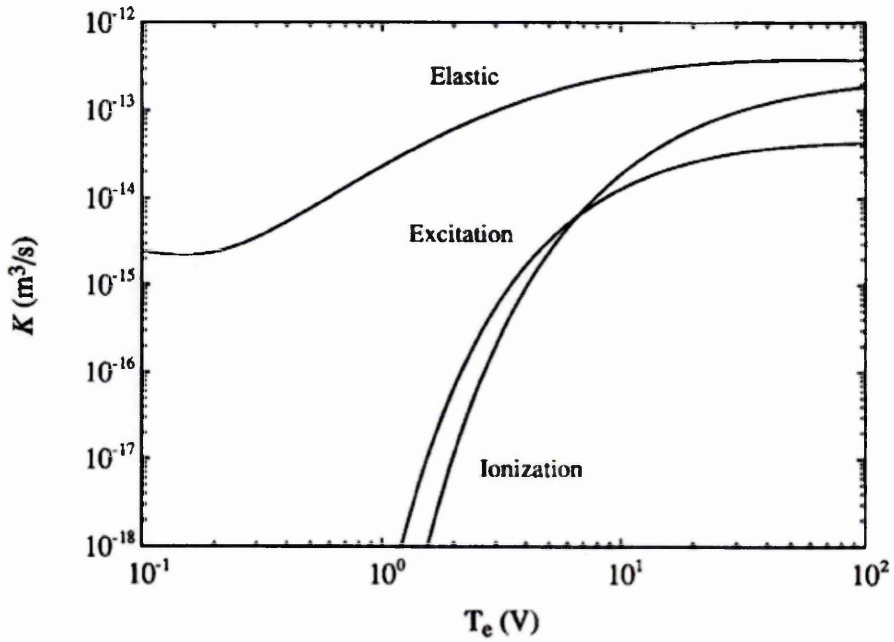

Figure 1.2: Elastic, excitation and ionization rate coefficients for electrons in argon as a function of electron energy [Lieberman and Lichtenberg, 2005].

The rate coefficient, K, expresses the volume rate of a reaction:

$$\nu = n_g K \tag{1.15}$$

A plot of K against the particle energy[3] gives a visual classification of the various reactions for the particle and gas under study. In Fig. 1.2 the rate coefficients for electrons in argon show that elastic collisions occur at all energies, increasing in rate with the electron energy. The excitation and ionization of the gas only take place beyond certain thresholds.

1.2.2 Surface Interactions

Among the various plasma-surface interactions, the most determinant are secondary electron emission, bombardment by neutrals or ions, and sputtering. Other processes, such as etching and film growth, can occur in principle. But these are not

[3]More precisely the voltage equivalent of its temperature, from Section 1.1.

relevant for microplasma physics and we shall focus on the three most important interactions.

Secondary electron emission plays an essential role in the creation (ignition) and stability of the discharge. The mechanism involves the collision of positive ions with the cathode surface, as mentioned earlier and originally described by [Townsend, 1900] for a DC glow discharge. Electron-ion recombination indeed occurs for virtually all incoming positive ions (Eq. 1.13).

The surface emission of electrons is due to *Auger emission*. Considering electrons at the Fermi level within the surface of a metal electrode, the minimum potential barrier for their emission is the *work function*, $\mathcal{E}_\phi$, of the material, as illustrated in Fig. 1.3(a). This diagram also shows the closely spaced (grey region) electron energy levels from zero at the bottom of the conduction band up to the Fermi energy, $\mathcal{E}_F$. In Fig. 1.3(b), an incoming ion within an atomic radius, a_{eff}, of the metal surface offers a potential well $\mathcal{E}_{\text{iz}}$; its ionization potential. A tunneling electron with energy $\mathcal{E}_e$ would neutralize the ion by entering either:

- an excited level, via

$$e^- + \mathrm{A}^+ + \mathrm{S} \rightarrow \mathrm{A}^* + \mathrm{S}$$

  Unless A^* is a metastable, it would then emit a photon upon de-excitation from its level $\mathcal{E}^* \approx \mathcal{E}_{\text{iz}} - \mathcal{E}_e$.

- the ground state, thereby allowing the (Auger) emission of a second electron if $\mathcal{E}_{\text{iz}} - \mathcal{E}_{e1} > \mathcal{E}_{e2}$.

The ignition and maintenance of a DC discharge therefore depend on $\mathcal{E}_{\text{iz}}$ for the gas and the cathode's work function. For the noble gases argon and helium, $\mathcal{E}_{\text{iz}}$ are 15.7 eV and 24.5 eV, respectively. Metastables can also readily trigger secondary electron emission if $\mathcal{E}_* > \mathcal{E}_e$. Example of metastable energies are 11.5, 11.7

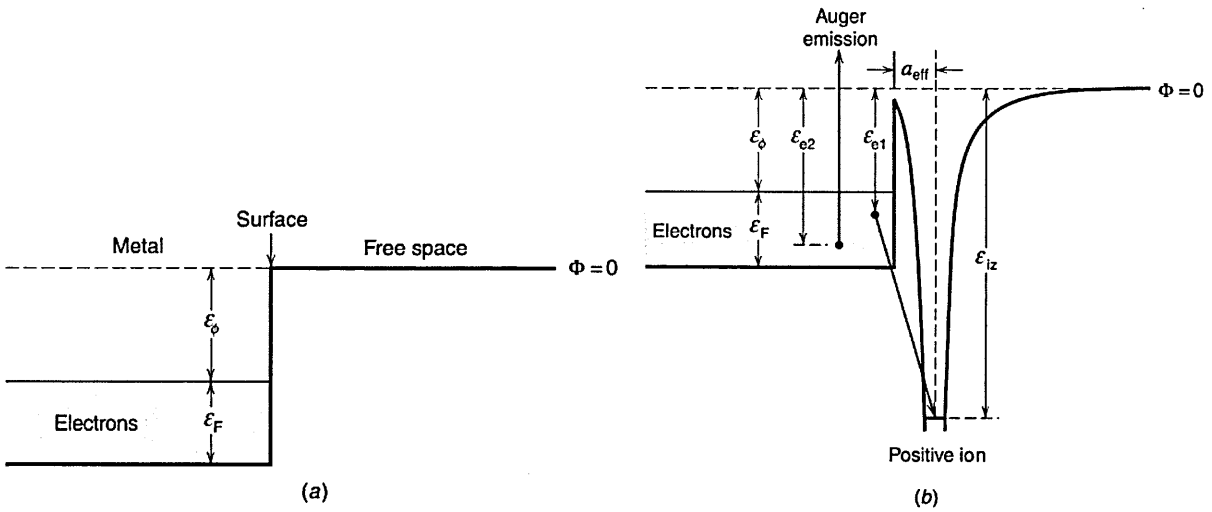

Figure 1.3: Work function, $\mathcal{E}_\phi$, Fermi energy, $\mathcal{E}_F$, and secondary electron emission by Auger emission [Lieberman and Lichtenberg, 2005].

eV for argon and 19.8, 20.6 eV for helium. As for the cathode material, typical work functions are 5.1 eV for gold [Lakits et al., 1990], 4.3 eV for molybdenum [Lieberman and Lichtenberg, 2005] and 4.9 eV for tantalum [Hagstrum, 1953]. The secondary emission coefficient, γ, indicates the number of secondary electrons created per incident ion. For 100 eV ions grazing a molybdenum surface, $\gamma_{Ar^+} = 0.115$ and $\gamma_{He^+} = 0.274$.

Heavy particles can also *sputter* the wall material. High voltage sheaths, which connect the plasma with confining surfaces, can accelerate ions to material-removing energies; particularly at the cathode, with the highest voltage. The sputtering yield, γ_{sput}, gives the number of surface atoms removed per incident ion. The threshold for this reaction is at $20 - 50$ eV, rapidly increasing in the hundreds of eV. Sputtering consists in the surface penetration by heavy ions followed by a cascade of energy transfer collisions between the (sub-)surface atoms in the impact region. With Ar^+ at 600 V, typical values are $\gamma_{sput} = 1.18$ for gold and $\gamma_{sput} = 0.32$ for tungsten.

In addition to particle exchanges, heat transfer is a critical interaction at the plasma-wall interface. Firstly, by affecting the balance of charged particles, gas rarefaction induces discharge instability[4]. Secondly, the operating temperature of the gas determines the choice of material and lifetime of the reactors. The last point raises the issue of thermal compatibility, describing how the differential thermal expansion of the constituent materials can affect the mechanical stability of the microdischarge device. Thirdly enhanced sputtering of the wall materials by the applied heat affects both the wall stability and the purity of the microdischarge (again leading to charge imbalance hence instabilities). Finally the relative importance of competing heat transfer routes vary with the operating parameters; size, pressure, input power. From the above, heat transfer is therefore critical for improving the operating conditions as well as for fundamental understanding of the microplasma-reactor interactions.

In *Joule heating*, energy from the electric field, E, is converted to heat by electrons in elastic collisions with the gas. The power per unit volume deposited in that way into the discharge is given in [Fridman and Kennedy, 2004]:

$$P_{\text{in}} = \sigma E^2 = \frac{n_e e^2 E^2}{m_e \nu_{\text{el}}} \tag{1.16}$$

with the conductivity, σ, and electron-neutral elastic collision frequency, ν_{el}. In steady state, this will equal the output power density:

$$P_{\text{out}} = n_g c_p (T - T_0) \nu_T \tag{1.17}$$

with the specfic heat per atom, c_p, the gas discharge temperature, T, the ambient temperature, T_0, and the heat transfer rate, ν_T. Heat transfer out of the discharge occurs by conduction and convection. For a cylindrical discharge of radius, R, and

[4]Discussed in the next section.

length l, these two mechanisms are expressed by

$$P_{\text{out}} = \frac{8k(T - T_0)}{R^2} + \frac{2u\ n_g c_p\ (T - T_0)}{l} \tag{1.18}$$

with the coefficient of thermal conductivity, k, and gas flow velocity, u.

1.2.3 Charged Particles' Behaviour

The initial stage of a plasma is the *breakdown* of the gas, during which free charge carriers are released to create a conductive pathway. Our focus is on DC discharges between two electrodes of fixed polarity: the positive anode and negative cathode. The *breakdown voltage*, beyond which plasma *ignition* occurs, can now be defined, based on the description by [Townsend, 1900].

On the one hand electrons are accelerated by the applied voltage and multiply exponentially by ionization. After a displacement, x, in the direction of the electric field, electrons go from an initial number, N_0, to

$$N = N_0\ \exp\left(\frac{x}{\lambda_{iz}}\right) = N_0\ \exp\left(\alpha x\right) \tag{1.19}$$

where λ_{iz} is the mean free path for electron impact ionization collisions. This mechanism is sometimes described in terms of α, the number of electrons produced per unit length per travelling electron. This phenomenon is referred to as an *electron avalanche*. On the other hand, secondary electron emission occurs by Auger emission at the cathode, with the corresponding γ coefficient.

To be self-sustaining, the α and γ mechanisms must balance all the particle losses; at the walls as well as in the volume of the plasma. This can be expressed in terms of the position-dependence of the electron flux, $\Gamma_e(x)$, and ion flux, $\Gamma_i(x)$ over the thickness of the cathode sheath ($0 \leq x \leq d$). From the continuity of charge and the definition of secondary electron emission ($\Gamma_e(0) = \gamma\ \Gamma_i(0)$) the following

relationship is obtained:

$$\alpha d = \ln\left(1 + \frac{1}{\gamma}\right) \tag{1.20}$$

For a linear electric field $E = V_b/d$, the breakdown condition, V_b, becomes

$$V_b = \frac{Bpd}{\ln Apd - \ln\left[\ln\left(1 + \frac{1}{\gamma}\right)\right]} \tag{1.21}$$

where A and B are determined experimentally, with the typical values for:

- argon: $A = 11.5$ cm^{-1} torr^{-1} $B = 176$ V cm^{-1}torr^{-1}
- helium: $A = 2.8$ cm^{-1} torr^{-1} $B = 77$ V cm^{-1}torr^{-1}

The importance of the relationship between pressure, p, and electrode separation, d, is illustrated by the *Paschen curve*, a plot of V_b against pd. According to the graph of Eq.1.21 in Fig. 1.4, V_b is maintained by keeping the product pd constant. The curve minimum represents the most efficient conditions for electron induced ionization. To the left of the minimum, a smaller d reduces the distance allowed for establishing sufficient electron avalanche. This is similarly hindered by the reduced density of neutral targets for electrons at lower p. As a result the Paschen curve rises steeply left of its minimum. On the other hand an increase in p gradually limits the mean free path hence the highest energy achieved by the electrons. At larger d the discharge requires a higher voltage to cross the inter-electrode gap. The last two phenomena translate into a small gradient to the right of the curve minimum.

The choice of gas and cathode material are both determinant for the ignition a discharge. For a given gas the lower V_b is obtained with the lower $\mathcal{E}_\phi$. In Fig. 1.4, the value of 4.3 eV for molybdenum versus 5.1 eV for gold yields a smaller V_b for the former. Auger emission, driving secondary electron emission at the cathode, was shown to depend on $\mathcal{E}_{\text{iz}}$. This is consistent with the low V_b in noble gases, with high

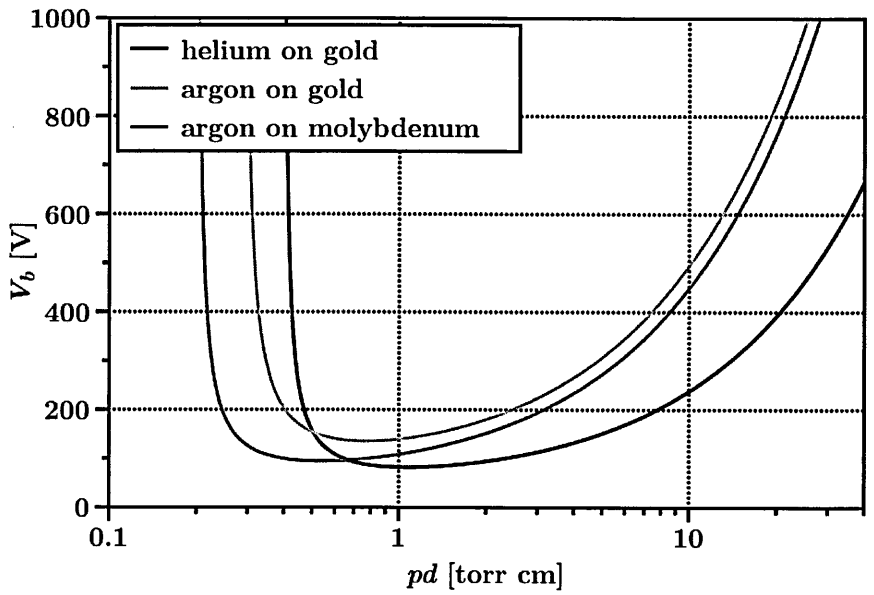

Figure 1.4: Paschen curve (Eq.1.21) in argon and helium with gold or molybdenum cathodes.

$\mathcal{E}_{\rm iz}$: 24.5 eV in helium and 15.7 eV in argon. These two gases are commonly used in plasma studies, including in this thesis.

Different discharge stages or modes are identified by their voltage-current or V-I characteristic. Fig. 1.5 shows the general relationship between discharge current and applied voltage for a non-equilibrium plasma. Going from left to right on the diagram, the applied voltage in the first gradually increases the α and γ contributions until they are self-sustaining. In this *Townsend discharge* the current increases by charge multiplication rather than acceleration; hence the voltage does not increase. The *differential resistance*, $\mathrm{d}V/\mathrm{d}I$, is zero there. The current densities are not yet sufficient to modify the vacuum electric field. In the *glow discharge*, charge and current densities are so high that the sustaining voltage drops and the electric field is controlled by the reactor geometry (e.g. Fig. 1.1). The *normal mode* maintains a negative to zero V-I slope and constant current density. Increasing I requires plasma growth on the cathode. When this becomes impossible, a higher V is needed to increase I (positive slope) in the so-called *abnormal mode*.

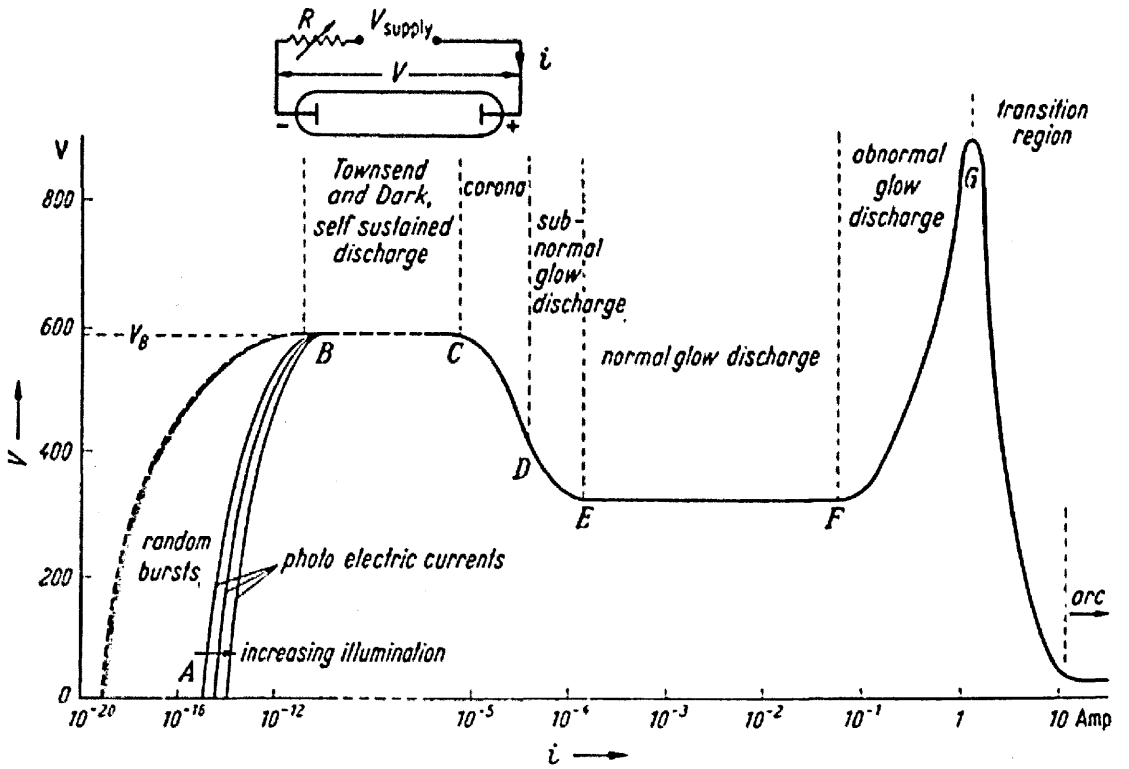

Figure 1.5: Voltage-Current (V-I) characteristic of electrical discharges [Lewin, 1965]. The inset shows the corresponding circuit diagram.

At higher current, the discharge transitions from a glow to an arc. An excess or shortage of charged particles jeopardizes the *plasma stability* [Kunhardt, 2000]. In a self-sustained discharge the steady state is expressed in terms of the earlier generation and loss rates, G and L:

$$G\, n_e = L\, n_e \tag{1.22}$$

Though not mentioned so far, the reduced electric field, E/n_g, is decisive. For instance it directly affects T_e via $\lambda_{\mathrm{el}} \propto 1/n_g$. Instabilities are:

- electronic: G/L imbalance leads to local space charge gradients
- thermal: heating causes gas rarefaction hence E/n_g increase

The current density and increased T_e conspire to further enhance the instabilities.

This can lead to a glow-to-arc transition; often fatal for the reactor.

The charged particles influence each other over a characteristic length: the *Debye length*. This process helps explain the establishment of sheaths and space charge regions (as in Fig. 1.1) while maintaining the overall plasma quasi-neutrality. Any electrically floating surface exposed to the plasma rapidly acquires a negative charge, owing to the relative fluxes of electrons, Γ_e, and ions, Γ_i:

$$\Gamma_e = \frac{n_e \bar{v}_e}{4} \quad \gg \quad \Gamma_i = \frac{n_i \bar{v}_i}{4} \tag{1.23}$$

following from $T_e \gg T_i$ and the higher electron mobility[5]. The potential, ϕ, around the resulting space charge, ρ, obeys Poisson's equation:

$$\nabla^2 \phi = -\frac{\rho}{\varepsilon_0} = -\frac{e}{\varepsilon_0}(n_i - n_e(x)) \tag{1.24}$$

with $\varepsilon_0 = 8.85 \times 10^{-12}$ F m^{-1} is the permittivity of free space. The parentheses describe an excess of ions in the near-wall region. Indeed, electrons are depleted by repulsion while ions are assumed too little mobile to change n_i. Electrons are assumed in thermal equilibrium, with the Boltzmann relation

$$n_e = n_0 \exp\left(\frac{e\phi}{k_B T_e}\right) \tag{1.25}$$

that can be substituted into Eq. 1.24, before simplifying to

$$\nabla^2 \phi = \frac{e^2\, n_0\, \phi}{\varepsilon_0\, k\, T_e} \qquad \text{with} \qquad \phi = -\phi_0 \exp\left(\frac{|x|}{\lambda_{\mathrm{De}}}\right) \tag{1.26}$$

[5]Given by $\mu = e/m\nu_{\mathrm{el}}$, where $m_e \ll m_i$ and ν_{el} is the elastic collision frequency.

The Debye length, λ_{De}, is that over which the plasma remains quasi-neutral:

$$\lambda_{\mathrm{De}} = \sqrt{\frac{\varepsilon_0 \, k_B T_e}{n_0 \, e^2}} \tag{1.27}$$

Typical Debye lenghts are in the micrometer scale. In the pressure range from 1 to 760 torr, the mean free path was earlier given for argon at 0.1 μm $\lesssim \lambda_{\mathrm{el}} \lesssim$ 100 μm. As for charged particle interactions, substituting in Eq.1.27 typical values of $T_e = 4$ eV and $n_e = 10^{16}$ m^{-3} from [Lieberman and Lichtenberg, 2005] yields $\lambda_{\mathrm{De}} =$ 0.14 mm for low-pressure glow discharges. In conditions of microdischarge operation (next section) the relevant values are $n_e = 10^{20}$ m^{-3}, similar T_e [Kushner, 2005] and $\lambda_{\mathrm{De}} \sim 1$ μm. This offers a transition into the realm of micrometer-sized plasmas, where the theoretical limit of quasi-neutrality is approached.

This section presented the necessary background theory on plasma physics. Inside the volume and at the surface of a laboratory electrical discharge, the main processes were discussed. Typical figures and phenomena relevant for this thesis were put forward. From the above, the micrometer scale stands out as particularly interesting.

1.3 Microplasma Physics and Recent Research

Some of the aforementioned plasma phenomena take on a particular importance in the context of microplasma. The role of dimension and reactor geometry are explained in this section. A background literature review is provided, that will be useful for later analyses. The section concludes with characteristic parameters and behaviours of interest to the current research. This will give the scope of our diamond-based research in the last section.

Even though miniaturization is an ancient plasma physics topic, the acceptance of Microplasma Physics as a field in its own right results from recent breakthroughs. It has been known since [Paschen, 1916] that increasing pressure should allow a decrease in size and vice versa. Gas discharges started to be intensively researched in the 1950's for display applications. What follows is based on the topical review by [Boeuf, 2003]. As an example, the Plasma Display Panels found in television sets are an expression of the current stage of that technology. A typical pixel consists of a noble gas discharge operated at 500 torr inside a 100-μm gap. Most applications involve the operation of electrodes covered with an insulator — in Dielectric Barrier Discharge configuration — which requires AC current. While DC pixels were also investigated, the first report of the stable operation of a microscopic high pressure DC plasma arrived in [Schoenbach et al., 1996]. This marked the birth of Microplasma Physics, epitomized by the creation in 2003 by Professor Tachibana (Kyoto University, Japan) of the biennial series of "International Workshops on Microplasmas". Probably, the difference with the past research was that the scientific endeavour regained its freedom from any preconceived technological outcome. All the major plasma conferences now boast dedicated microplasma sessions. Additionally numerous review papers have illustrated the cross-disciplinary appeal of microplasma research and technology [Tachibana, 2006, Becker et al., 2006, Foest et al., 2006, Iza et al., 2008]. Applications have already been realised. Most recently, the research team of Profs J. G. Eden and S.-J. Park (University of Illinois, USA) have commercialized microplasma-based light sources and water purification tools[6]. The concepts introduced in the first parts of this chapter will now serve to introduce this lively field of microplasma physics.

[6]Eden Park Illumination (http://edenpark.com) and EP Purification, Inc., respectively.

1.3.1 Confining Dimensions

In a microplasma more than in any larger discharge, the reactor dimensions determine the operating conditions. The Paschen curve was earlier shown to link the breakdown voltage and *pd*. This is based on the assumption that the governing self-sustaining mechanisms are (i) the electron avalanche and (ii) ion-induced secondary electron emission at the cathode.

The successful operation of a DC non-thermal microplasma near atmospheric pressure by [Schoenbach et al., 1996] has triggered multiple research and technology perspectives. Figure 1.6 represents a cross-section of their original device. A mica insulator (250 μm thick) separated molybdenum electrodes. A 700-μm diameter blind cavity housed the microdischarge, which was operated at hundreds of volts. Several criteria confirmed the non-thermal nature of Townsend and glow discharges:

- visual: diffuse or glow-like, but not filamentary like an arc
- electrical: the *V-I* characteristic of Townsend, normal and abnormal glow modes
- thermal: the electron energies required for ionization — several eV — would exceed the melting temperatures of the materials if coupled with the heavy particles; below 2000 K for mica and 3000 K for molybdenum

Microscopic discharges have existed for decades, namely used in the pixels in plasma television panels. The major difference was that at least one electrode was covered with an insulating layer; precluding DC operation and ignition/sustainment by the two mechanisms cited above. Microplasmas have now been operated in AC, RF (13.56 MHz), microwave and with all the power supply variants of "macro"-plasmas, via capacitive[7] or inductive[8] coupling [Iza et al., 2008]. The new micro-

[7]Breakdown of a gaseous dielectric between opposite electrode polarities.
[8]Operation by induction with a driving electrode often outside the reactor.

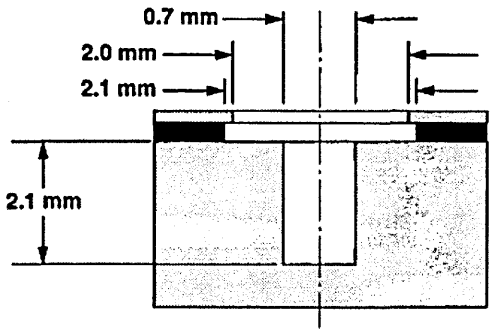

Figure 1.6: First microplasma molybdenum-mica-molybdenum device from [Schoenbach et al., 1996] with dimensions.

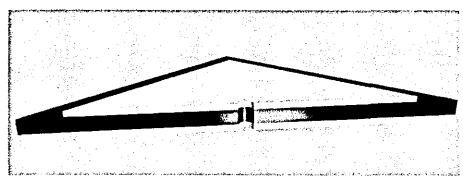

Figure 1.7: Cross-section (not to scale) through the diagonal of a square MHCD device, showing the electrodes (yellow) either side of the dielectric (black) as well as the through hole.

plasma offers the possibility to study microscopic replicas of the non-thermal low pressure glow discharges that have been of so much interest, e.g. in the work of [Lieberman and Lichtenberg, 2005].

The *pd* (Paschen) relationship is supported in general, but significant electric field enhancements are notable microplasma peculiarities. A Paschen curve was experimentally obtained in argon for several electrode materials by [Sismanoglu et al., 2010]. Their source was a microhollow cathode discharge (MHCD) (Fig. 1.7); basically a through-hole version of the "original" model (Fig. 1.6). Their device consisted of 100-μm thick metal foils separated by a 250-μm thick mica spacer and a hole 200 μm in diameter. Their curve in Fig. 1.8 is reminiscent of the theoretical graph in Fig. 1.4. As expected, the lowest work function (increased Auger emission) of aluminium leads to the lowest V_b; the converse is true for nickel.

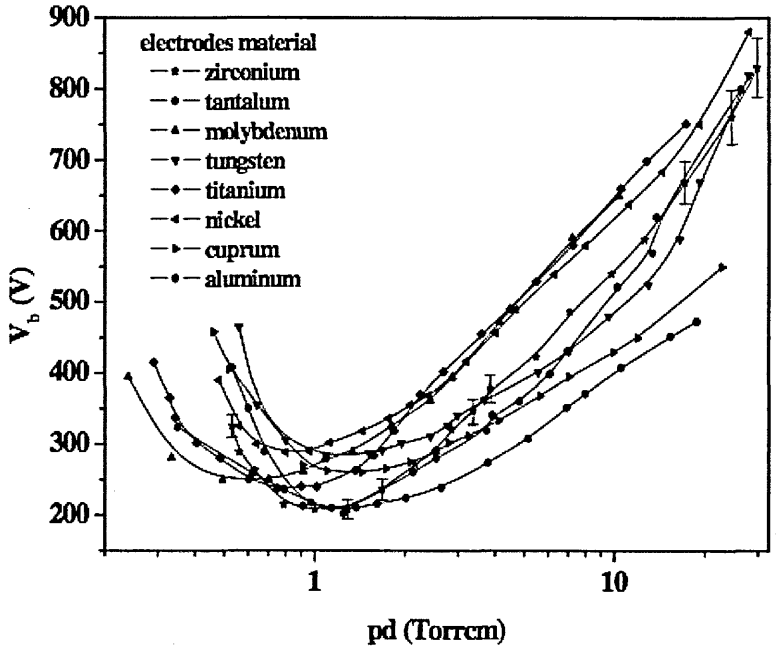

Figure 1.8: Paschen curves in a 200-μm diameter argon MHCD with fixed d = 250 μm and various electrode materials [Sismanoglu et al., 2010].

The Paschen law fails for low pd, i.e. to the left of the minimum V_b. With the close electrode proximity, dx, the applied voltage, dV, significantly enhances the electric field, E_x, in a microplasma: $E_x = -\mathrm{d}V/\mathrm{d}x$. This, along with electrode surface roughness, has long been linked to a higher electron extraction by so-called ion-enhanced *field emission* [Llewellyn Jones and Morgan, 1951]. Experiments with $d \leq 40$ μm [Slade and Taylor, 2002] or ≤ 20 μm [Sismanoglu and Amorim, 2008], placed the importance of this effect at the smaller dimensions only.

Very steep potential gradients and high pressure lead to high charged particles densities [Kushner, 2005], reflected in the current densities. In fact the typical power per volume in a microplasma, in the MW cm^{-3} to GW cm^{-3}, is similar to what is found in a fusion plasma rather than in low pressure centimetre-sized discharges (W cm^{-3}). Under these conditions a "macro"-plasma should contract into an arc by positive feedback of electric and thermal instabilities [Kunhardt, 2000]. The stable non-thermal microplasma may therefore be the result of strong stabilizing mechanisms that are yet to be understood.

The confining vessel sets the surface-to-volume ratio and controls the competition between gas and surface processes. Indeed that ratio is 1:1 for common (centimetre-sized) plasmas versus 300:1 in a microplasma. As an example, heat transfer may become important through the dielectric when it is a few orders of magnitude thicker than the electrodes in an MHCD reactor.

The gas temperature increase with current was modelled in argon by [Kushner, 2005], in agreement with experimental results from [Penache et al., 2002]. Gas rarefaction due to heating — from 360 K at 0.15 mA to 1100 K at 4 mA — was responsible for the increased current density via high E/n_g. Indeed, the electron multiplication mechanisms at the cathode did not match the current density increase.

Besides the dimensions, the shape of the reactor plays a determining role in microplasma physics. This is now explained, along with a thorough description of the specific geometry of interest to our research.

1.3.2 Reactor Geometry

The reactor geometry affects the microplasma behaviour. Gas and plasma effects due to heating or electric field distribution are different in blind and through-hole geometries[9]. This differential confinement can also enhance certain surface and volume reactions, intensifying the effects of miniaturization highlighted previously. This is particularly true of one geometry.

For decades the *hollow cathode discharge* (HCD) has benefited research and technology, and its microplasma version, called the *microhollow cathode discharge* (MHCD) is being explored for applications by many groups. Its main parameters are displayed for the general cross-section of the cylindrical[10] cathode cavity in Fig.1.9.

[9] As in Figs. 1.6 and 1.7, respectively.

[10] The important geometrical criterion is actually to have cathode falls facing each other.

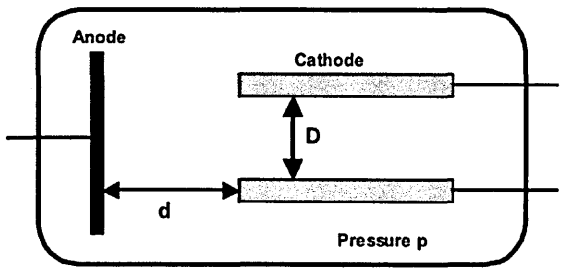

Figure 1.9: Cross-section of the hollow cathode discharge (HCD) geometry with the main parameters [Kogelschatz et al., 2005].

Diametrically opposite cathode falls give rise to a radial potential distribution which enhances the electric field once space charges develop inside the hole. Unlike plane parallel electrodes, radially accelerated electrons that reach a cathode region are reflected back into the plasma. As they oscillate, these *pendulum electrons* make more inelastic collisions. This helps limit instabilities since any charge build-up would quench the oscillation-driven ionization [Kogelschatz et al., 2005].

This geometry favours high electron energies. [Gill and Webb, 1977] measured their energy distribution in a 15 torr helium, 8 mA HCD at the cathode sheath-negative glow interface. Fig.1.10 represents the signal intensity received at a retarding field analyzer, as a function of the retarding voltage. The following energy groups were identified:

- a "beam" of electrons with energies corresponding to the cathode fall
- beam electrons after a single inelastic collision; the second peak occurs after a separation equivalent to the first excitation potential of helium.
- high-energy electrons in the long tail; more than in linear geometries
- electrons with energies similar to those in the bulk of the plasma, at the distribution maximum

An extra pD relationship depends on the cathode opening diameter, whereas the anode shape is irrelevant. For 0.1 torr cm $< pD <$ 10 torr cm the discharge

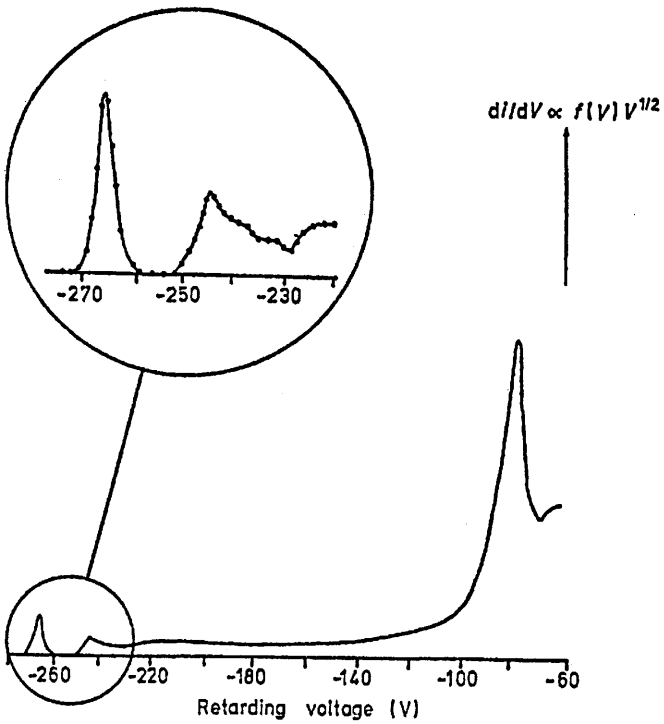

Figure 1.10: Electron energy (in terms of voltage of a retarding field analyzer) for a HCD in 15 torr helium at 8mA [Gill and Webb, 1977].

develops in stages [Kogelschatz et al., 2005]. In the low current, diffuse, Townsend mode the electric field resembles that in the absence of a plasma. It grows into the hole at higher current, forming a virtual anode.

In the *hollow cathode mode* the plasma and power densities increase inside the negative glow [Kushner, 2004] translated in a negative V-I slope. The efficiency of the MHCD was detected by [Frame et al., 1997] in the emission spectrum of neon. The intensity of high energy Ne^+ states (indicated by asterisks in Fig. 1.11), which require energies above 30 eV, was attributed to *beam* electrons. At higher pressure T_e decreases in higher-frequency collisions and cancels the hollow cathode effect. The spectrum at 200 torr was identical to emission from a plasma column. The role of opposite cathode regions was confirmed by [Moselhy and Schoenbach, 2004] when they operated an MHCD-like reactor with a flat (zero-depth) cathode flush

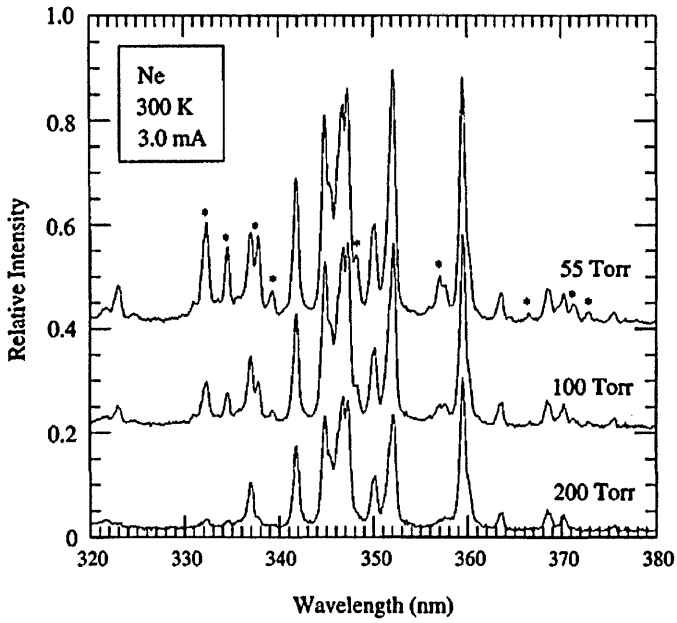

Figure 1.11: Neon UV emission in a 400-μm diameter MHCD. High energy Ne^+ states (asterisks) signal the hollow cathode mode [Frame et al., 1997].

with the dielectric. In the absence of radially oscillating electrons, this forced the abnormal mode, with positive V-I. Microplasmas are strong UV emitters, but the related mechanisms are further enhanced by the concave MHCD shape.

The incurved geometry enhances species retention and efficiency. An example is the metal-ion laser described in [Lieberman and Lichtenberg, 2005] and based on the HCD. Beam electrons ionize noble gas atoms, which drive the main ionization reaction of metal atoms via charge-exchange. The metal ions are the major source of secondary emission and sputtering. Noble gas metastables also contribute to the high energy levels of metal ions and are "more effectively retained by the concave geometry of the HCD" [Gill and Webb, 1977]. The latter tested the efficiency of beam electrons by measuring the dependence of ionization rates on metal vapour concentration. It took 10% in the HCD and only 0.1% in a linear geometry to observe ionization decrease; explained by the consumption of electrons in low metal ionization potentials.

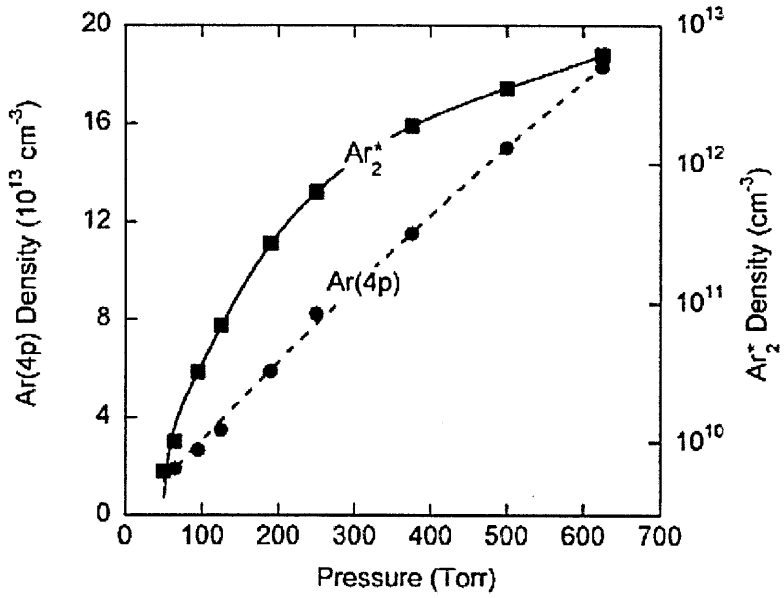

Figure 1.12: Pressure dependence of an excited argon atom emitting visible light (left-hand axis) and an excimer (right) [Kushner, 2005].

Strong UV emission follows from high pressure and energies, which foster three-body reactions and stepwise processes. The lifetime of species like metastables, e.g. Ar_m^*, is longer than the inter-collision time. The excited dimers (or *excimers*), Ar_2^*, produced as follows emit in the UV

$$Ar_m^* + 2Ar \rightarrow Ar_2^* + Ar \tag{1.28}$$

with a strong p-dependence. Indeed in their MHCD model [Kushner, 2005] showed that metastable density "scales with the square of the Ar density", while the excited state Ar(4p) emits in the visible and scales linearly (Fig. 1.12).

It is clear that microplasmas, in various geometries, have distinct operating regimes that are often governed by the role of the enclosing surfaces. This in turn affects the operating characteristics of the discharge, which is the subject of the next section.

1.3.3 Operating Characteristics

Certain operating characteristics of the microplasma, particularly the MHCD, are described here, that will be of interest for the analysis of our results.

Microplasmas can be operated in both normal and abnormal glow modes. As is the case for any glow discharge in the normal mode, the plasma maintains a constant current density at higher power by expanding over the cathode surface. With the cathode covered up or intentionally limited, [Dufour et al., 2008] turned a helium MHCD to abnormal mode.

The cathode sheath shrinks with pressure. This general plasma behaviour was confirmed in MHCD's in experiments [Lazzaroni et al., 2010] and a simulation [Kushner, 2005]. The former took Ar^+ emission (427.752 nm) to indicate the peak ion density at the cathode sheath edge, that shifted towards the walls of a 400-μm diameter MHCD at higher pressure and compressed the sheath (Fig. 1.13, left-hand side). The right-hand side shows the maxima of ionization by electron beams move towards a 300-μm diameter cathode (illustrated with the rates S_{ebeam} in $\mathrm{cm}^{-3}\ \mathrm{s}^{-1}$).

The various microplasma stages introduced earlier for operation at 0.1 torr cm $< pD <$ 10 torr cm were illustrated by [Schoenbach et al., 1997]. In argon at 56 torr, a central plasma column grew with increasing I inside a 200-μm diameter MHCD. The initially negative V-I curve — consistent with a hollow cathode mode — turned flat at high current, during cathode-side expansion. At 250 torr the microplasma started as a diffuse ring, with positive resistivity — consistent with a Townsend mode. It only developed into a column inside the hole at higher I. At 896 torr, the microplasma was radially asymmetric for the entire current range.

This review of microplasma fundamentals emphasized the dependence of various

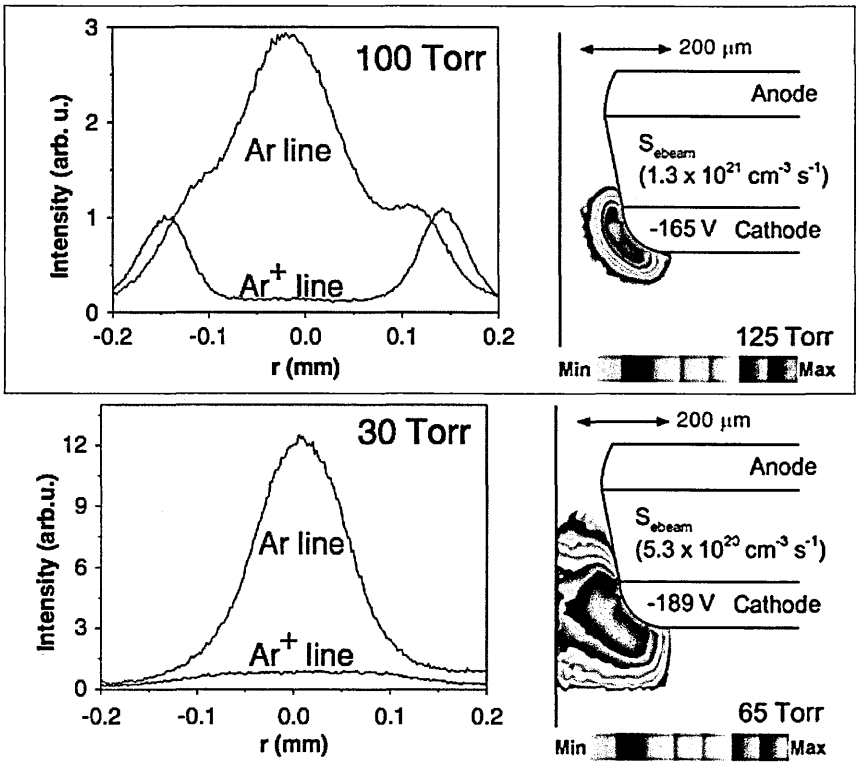

Figure 1.13: Radial profile of the negative glow inside an MHCD: (left [Lazzaroni et al., 2010]) measuring the Ar^+ emission and (right [Kushner, 2005]) modelling ionization rates by beam electrons (in cm^{-3} s^{-1}).

reactions on the size and shape of the reactor. As a special case, the MHCD provides a convenient tool for further exploration of this topic. In particular, the focus of this thesis is on the role of materials (electrode and dielectric) on various aspects of microplasma operation. The next section concludes our introduction with the motivation and scope for research in diamond-based devices.

1.4 Diamond-Based Experimental Studies

This section first introduces the motivation for studying the role of materials on microplasma characteristics then sets the scope for temperature studies.

1.4.1 Influence of Different Materials

The dielectric material affects the electrical characteristic of the microplasma. *V-I* curves for MHCD's based on thin films of aluminum oxide (Al_2O_3), boron nitride (BN) or barium titanate ($BaTiO_3$) were obtained by [Park and Eden, 2003]. Other conditions like pressure, p, and dielectric thickness, d, were also varied. For 50-μm diameter devices, the abnormal glow mode was obtained in alumina (Al_2O_3)[11] at 0.1 mA $\leq I \leq$ 0.4 mA, BN[12] at 0.08 mA $\leq I \leq$ 0.25 mA and $BaTiO_3$[13] 0.15 mA $\leq I \leq$ 0.4 mA at 400 torr or above 0.25 mA at 800 torr. With a thicker Al_2O_3 layer (200 μm) the abnormal glow mode occurred only at 600 torr whereas from 700 to 1200 torr the discharge transitioned from Townsend (negative *V-I*) to normal glow (flat curve). That the most significant change is due to a thicker dielectric is not surprising. Indeed, with all three materials chosen for their thermal properties, the latter must be determining in driving heat transfer. A better understanding of the heat transfer routes inside a microplasma therefore requires experimental characterization of the temperature conditions.

Silicon-based devices offer interesting electrical, thermal and fabrication characteristics. Established semiconductor processing techniques have successfully been adapted, namely by the groups of Profs J. G. Eden and S.-J. Park (University of Illinois, USA) and R. Dussart (GREMI, Université d'Orléans, France). The advantages cited are its high thermal conductivity (148 W m^{-1} K^{-1}), melting temperature (1685 K) and resistance to ion sputtering [Frame et al., 1997, Dussart et al., 2010]. As a semiconductor, silicon enables more stable operation as well as a *distributed resistive ballast* for an array of microplasma in parallel. Compared to metal electrodes, it allowed more homogeneous discharges and stability over a wider range of conditions [Portsel et al., 2009]. The negative *V-I* slope or indeed any instability

[11] $d = 120$ μm, $400 \leq p \leq 1100$ torr
[12] $d \sim 30$ μm, $500 \leq p \leq 1100$ torr
[13] $d = 100$ μm

can potentially lead to unsustainable current levels. Ballast resistors are therefore placed in series with the (micro)plasma, or indeed each reactor in an array of several microplasmas. Using a semiconductor like silicon offers the same single safeguard for all the reactors in the same substrate [Shi et al., 1999].

Several limitations of silicon devices were nevertheless highlighted. A typical lifetime limiting failure includes the vaporization or sputtering of the nickel thin film, often used as the anode material [Park et al., 2001, Dussart et al., 2010]. Both conducted DC operation of MHCD-like devices with a blind cathode. When the hollow silicon was used as the cathode, the devices were unstable or failed as well. Further tests suggested that silicon sputtering and redeposition contributed to short-circuits and eventually failure [Kulsreshath et al., 2012]. Finally, semiconductor fabrication techniques are indeed successful but they involve numerous steps. Combined with the various layer materials, this is detrimental to both operation (e.g. surface short-circuits) and study (plasma contamination).

Enhancing the electron emission of the cathode material can improve the performance of microplasma devices. In [Park et al., 2004] carbon nanotubes, selected for their high field emission properties, were grown on the surface of the nickel cathode of a DC operated MHCD. The ignition and operating voltages were lowered, meanwhile increasing the output power. Alternatively, a high-γ material can be envisaged to enhance electron emission.

Now, before outlining the potential of diamond for addressing the above issues, we present the scope for investigating temperature conditions.

1.4.2 Temperature Studies

Temperature effects influence both the operation and study of a microplasma. While discussing the role of dielectric on the mode of microplasma operation, heat transfer appeared a good candidate to characterize the different materials. And even though silicon is favoured for its thermal properties, it is evident that its lifetime — perhaps owing to wide ranging thermal characteristics in the various materials making up a reactor — is determined by heat related reactions. More generally, there is a lack of background data on how repeated exposure of reactors to thermal conditions of a microplasma affect the reproducibility of experimental results. It also brings into question the significance of the customary assumption of a cathode fixed at room temperature in microplasma models, e.g. [Kushner, 2005, Boeuf et al., 2005].

Microplasma can be operated at a wide range of gas temperatures. For an argon microplasma, [Penache et al., 2002] obtained experimental values by diode laser atomic absorption spectroscopy. In a hole 300 μm in diameter through a sandwich of copper-Kapton®-copper (130–50–130 μm thick), at constant 0.1-W input power, the gas ranged from about 400 K at 40 torr to 1100 K at 300 torr. In a 200-μm diameter MHCD with molybdenum-mica-molybdenum (100–250–100 μm thick), [Sismanoglu et al., 2010] derived the gas temperature from two methods: based on the emission line profile of OH and Ar. Considering the different uncertainties of the two methods, the values ranged from 460 to 640 K for $7 < I < 15$ mA at ~ 230 V — 1.6–3.5 W — at atmospheric pressure. These lower temperatures were attributed to the 700-sccm flow of argon; reporting static gas values around 2000 K.

Assessing the relative importance of the gas and confining wall materials for heat transfer requires the systematic study of gas temperatures in a variety of such materials. The range of coefficients of thermal conductivity, k, covered by the current research is illustrated in Table 1.1. It also contains values for typical dielectric and

Table 1.1: Thermal conductivity, k, of some materials used in microplasma devices (in **bold** for this research).

Material	k / W m^{-1} K^{-1}	References
Kapton® †	0.12	DuPont [kap, 2006]
Glass	1.38	[Incropera and DeWitt, 1996]
Alumina	36	[Incropera and DeWitt, 1996]
Silicon	148	[Incropera and DeWitt, 1996]
Copper (pure)	401	[Incropera and DeWitt, 1996]
Diamond‡	2050	[Wörner et al., 1996]

electrode materials reported in the microplasma literature. Some electrode materials are listed, although dielectrics are typically thicker by orders of magnitudes in an MHCD. The latter are therefore expected to play a role in the heat transfer competition between solid and gas.

The above literature review has underlined the critical role of the wall materials and highlighted the need for further research in this area.

1.4.3 Outline of this Thesis

The background in this chapter has shown evidence of the rapid development of the newly established microplasma research. The increased understanding in fundamental aspects of microdischarge behaviour has been demonstrated in the literature, conferences and technological breakthroughs. However the effect of device materials on the operating characteristics remains underinvestigated, despite its overwhelming influence in microplasma physics.

The research reported in this thesis addresses two topics mediated by the walls and/or electrode materials: the influence of semiconductivity and the competing heat transfer modes inside MHCD reactors. Their systematic study was conducted inside micro-devices based on diamond obtained by Chemical Vapour Deposition (CVD).

Chapter 2 provides additional background that will be necessary in the subsequent discussion chapters. The CVD process, conducted within our research consortium, will be described in detail along with the properties of the resulting material. An established technique for gas temperature measurement will finally be described, which is based on the discharge emission spectrum.

The experimental methods and equipment employed in this research are presented in Chapter 3, along with the computer program used to extract temperature values from the spectroscopic data.

Chapter 4 reports on the first operation of diamond-based microplasma. A brief description of the fabrication by our consortium partners is followed by results and discussions about electrical and optical characterization at various pressures, dimensions and gases.

In Chapter 5, the focus will be on the interface between the microplasma and the dielectric with an emphasis on heat transfer. For that reason, the reported experiments will concern temperature studies conducted with reactors based on two materials at opposite ends of the thermal conductivity range: diamond and glass.

Chapter 2

RESEARCH BACKGROUND

This thesis focuses on the characterization of microdischarges operated inside diamond-based reactors. In this chapter, the background required for the research presented in later chapters is introduced. The topics include synthetic diamond, microplasma modelling and the basis of one important experimental technique.

Section 2.1 *CVD Diamond* discusses the essential properties of this versatile material and their control during fabrication. Finally, Section 2.2 *Gas Temperature Measurements* describes an established technique based on the study of the emission spectrum from traces of N_2.

2.1 CVD Diamond

This section explains the *chemical vapour deposition* (CVD) of diamond. The description will concern its essential properties and how they can be tailored, e.g. to optimize the microplasma reactors for this research. The precise conditions determine the type and hence the properties of the resulting thin film. These ultimately determine the function of the diamond layer, i.e.: electrode or dielectric. The versatility of CVD is now further described.

2.1.1 Chemical Vapour Deposition

Chemical vapour deposition (CVD) is a technique for depositing thin films of many different materials and is the standard technique for controllably depositing layers of diamond. Applied for decades, it is however in the 1980's that prospective technological and scientific progress simultaneously motivated the development of a "standard model" for its description. It is still the matter of adjustments and re-evaluations but it remains the accepted theory on which the following explanations are based.

Diamond CVD can be summarized as the activation of a carbon-containing gas (e.g. methane) in order to deposit a thin film of diamond on a substrate. The dissociation of the hydrocarbons to release carbon atoms is conducted by hydrogen [Ferro, 2002]. For this reason the gas mixture inside the reactor chamber is required to contain an excess of hydrogen, typically in the ratio 1% CH_4/H_2. Energy is needed to dissociate H_2 into reactive H atoms. The latter react at the solid surfaces, with the carbon precursor gas or recombine into H_2. Within the gas, the most important reaction is the creation of the methyl radical, CH_3, which plays a driving role in the growth of the diamond film. At the surface, various hydrocarbons are added to the surface (adsorbed) while others, along with hydrogen atoms, are subtracted (desorbed). As long as the right conditions are maintained, this results in the construction of diamond crystals. The steady state between all the reactions, hence the net deposition of carbon on the surfaces, is therefore controlled by a set of surface and volume conditions, including the substrate temperature.

Common sources for the activation energy are plasma enhanced CVD (PECVD) and the hot filament method [Butler et al., 2009]. In the former, a plasma is generated inside the deposition reactor right above the substrate. This energetic environment drives the dissociation of hydrogen, mainly via electron impact excitation

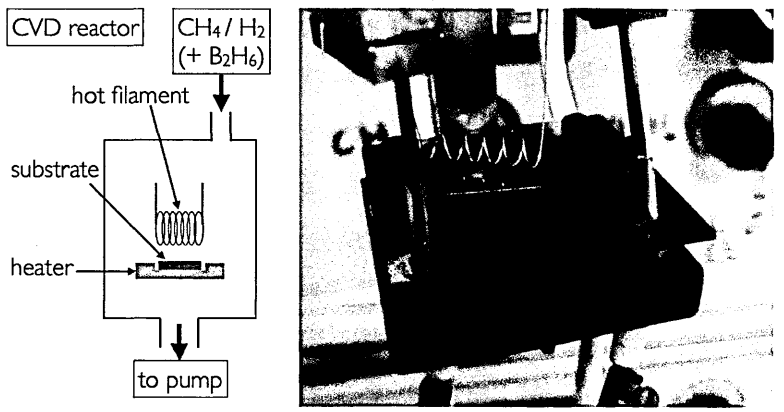

(a) (b)

Figure 2.1: (a) Diagram of the chemical vapour deposition of diamond. (b) Photograph (taken from the current research) of the substrate holder/heater outside the reactor chamber. A diamond wafer lies underneath the filament.

or collisional energy transfer. Indeed collisions are frequent at the typical operating pressure of 20 torr. With the hot filament, H_2 is thermally dissociated at its surface, which is maintained at a temperature above 2300 K. Materials with a high melting point are thus used, e.g.: tungsten (3683 K) or tantalum (3269 K). The hot filament method is illustrated in Fig. 2.1. Part (b) depicts a holder, about 5×5 cm^2, that heats the substrate to optimize diamond deposition. The system (used in this research) was taken out of the CVD reactor, the controls of which are visible in the background. Underneath the filament lies a commercially available diamond wafer on top of which another layer of diamond was grown. The substrate and the filament are separated by a couple of millimetres. All the surface and volume reactions depend on a complex set of coupled parameters such as the energy distribution for the various populations $(T_e, T_{\text{gas}}, T_{\text{H}}), n_{\text{H}}$ or the dominant hydrocarbon species present. Different methods of energy input act differently on those parameters; resulting in various rates of diamond deposition. Nevertheless, typical values are between 0.1 and 10 μm per hour [Ashfold et al., 1994].

2.1.2 Thin Film Diversity

Diamond is not the only thin film obtained during CVD. Carbon, whether naturally occurring or synthetic, exists in very different phases. For the state of thermodynamic equilibrium, they occupy distinct pressure-temperature regions on a phase diagram. Graphite is found in the region corresponding to the conditions of interest here. It is thus *thermodynamically stable* under these conditions. Diamond has a higher mass density, with $\rho = 3513$ kg m^{-3} versus 2260 kg m^{-3} (at 293 K), which is consistent with its creation in high pressure, high temperature environments [Ashfold et al., 1994]. However, it takes so long to convert to graphite under standard conditions of pressure and temperature that, to all intents and purposes, it is also stable. It is said to be *kinetically stable.* Not all carbon atoms would necessarily take on either of these two crystal structures. From now on, the remaining arrangements will together be referred to as *amorphous carbon.* In a *diamond* thin film the three phases can actually cohabit.

The three main forms of carbon give rise to an extremely vast range of basic properties. Graphite is conductive and slippery (it is used as a lubricant). Every atom is covalently bonded to three neighbours, forming a sheet of hexagonal rings; this is actually *graphene.* In the third dimension, these sheets are stacked, held together by weaker van der Waals interactions; explaining the slippery nature. Diamond is an insulator and the hardest known material. Every atom is covalently bonded to four neighbours in a three-dimensional cubic crystal structure. Both phases have similar thermal properties whereas amorphous carbon has a thermal conductivity $k \approx 2$ W m^{-1} K^{-1} a thousand times smaller. The coefficient, k, can be thought of as the sum of the contributions from free electrons, k_e, and vibrational states of the crystal lattice, k_l [Incropera and DeWitt, 1996]. In non-metals k_l is dominant, and highly dependent on the regularity of the lattice; hence the lower thermal conductivity in the amorphous structure.

The selective growth of diamond is controlled by the substrate temperature [Ferro, 2002]. Diamond CVD is possible over a wide range of temperatures but in practice temperatures in the range 1200–1400 K are used. Lower temperatures lead to low deposition rates while higher temperatures favour graphite deposition. The actual process of selection is based on the preferential etching of graphite versus diamond by hydrogen. Concurrently, the most abundant radical in the gas, H, combines with a surface H. H_2 is desorbed above 1098 K [Butler et al., 2009], thereby enabling a strong C-C bond to be completed by CH_3. Further desorption and bond reconstructions gradually build up the three-dimensional diamond structure.

Multiple nucleation sites lead to the growth of *polycrystalline* diamond [Ashfold et al., 1994]. The film is thus made up of many diamond crystals with varying orientation and size. This is evident from the scanning electron micrograph in Fig. 2.2(a). It depicts a thin film that was deposited on a silicon substrate (not visible), with a 5-μm scale in the bottom right corner. All cubes appear to have sides a couple of μm. Such films with crystal dimensions in the micrometer range are called *microcrystalline*. In single crystal diamond a single lattice is maintained throughout the sample. But it is more challenging to grow via CVD. Sometimes (synthetic or natural) single crystal diamond is implied when the superlative properties of diamond are described. However certain studies have focused on polycrystalline CVD diamond, which show promising applications [Sussmann, 2009] and share many of those properties, e.g. thermal conductivity [Wörner et al., 1996] (see Table 1.1).

The size of the diamond crystals is controlled by the substrate temperature and the partial pressure of CH_4 [Ashfold et al., 1994]. This dependence on the deposition conditions is represented in Fig. 2.2(b). The ordinate gives the ratio of CH_4 to the total CH_4+H_2, ranging from 0.1 to 100 %. On the abscissa the substrate

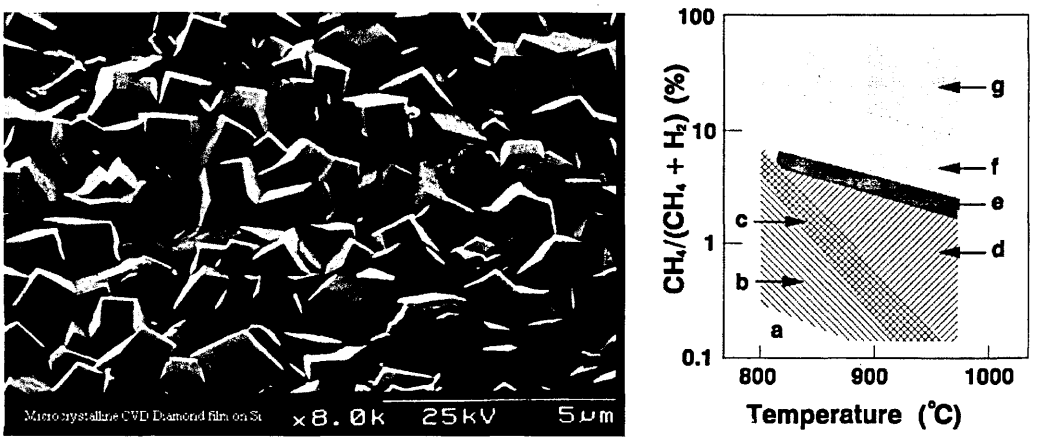

(a) (b)

Figure 2.2: Polycrystalline diamond thin films [Ashfold et al., 1994]. (a) Microcrystalline diamond. (b) Film type dependence on growth conditions.

temperature goes from 800 to 1000°C. At constant temperature, increasing the relative amount of CH_4 leads to the deposition of microcrystalline diamond thin films (regions **b**, **c**, **d**, **e**) varying in their dominant crystal orientation. In region **f** the film consists of nanocrystalline diamond — i.e. with sizes in the nanometer range — and graphite. Regions **a** and **g** correspond to a negligible presence of diamond. A similar evolution in the film structure could be obtained by increasing the temperature at constant CH_4 concentration. During CVD, microcrystalline diamond is columnar, i.e. its crystals grow perpendicularly to the deposition plane. Moreover the grain size increases the further away from the substrate.

The film structure at the boundaries between the crystals is a determining factor for the various films' properties [Isberg, 2009, Garrido, 2009]. Microcrystalline diamond has higher thermal and electrical conductivities than the nanocrystalline one. As mentioned above, other forms of carbon can exist in the film. While graphite is pervasive in nanocrystalline diamond, a relatively low graphite content exists in microcrystalline films; mostly concentrated at the boundaries between the crystals. The grain boundaries are also the site of defects. They can take the form of pinholes

or be regions of high impurity concentration. The latter can come from contamination of the processing gas or from intentional doping of the film in order to change its electrical behaviour, as explained next.

2.1.3 Semiconducting Diamond

This section describes how diamond thin films can be made *semiconducting*, fundamentally changing the properties and hence the applications of the deposited layer. The preceding discussion focused on the deposition techniques and film properties of *insulating* diamond. Co-existing forms of carbon were shown to follow from CVD, though the process can be optimized to obtain mainly diamond. Even then, the resulting crystal structure was further controlled by the deposition conditions. As was the case for insulating films, the properties of a semiconducting diamond film can be finely controlled through the parameters of the CVD process.

Adding atoms of the appropriate dopant species to the gas phase initiates extrinsic semiconductivity. In a semiconductor, the bandgap designates the forbidden electron energy levels that separate the valence band from the conduction band. Diamond is a so-called *wide bandgap semiconductor*. Its insulating character follows from the 5.47 eV barrier to conduction facing the electrons in its valence band. As a comparison, electrons need only surmount 1.12 eV in silicon; room temperature corresponds to a thermal excitation of 0.026 eV. Impurity atoms incorporated into the crystal structure offer additional energy levels to the semiconductor. The latter becomes *p-type* when the so-called *acceptor* dopant atoms have fewer valence electrons and the majority charge carriers are positive *holes*. In an *n-type* semiconductor, the extra electrons of the *donor* dopants drive conduction.

Boron is the main (p-type) dopant for diamond. Starting with the CVD methods introduced earlier, the only requirement is the addition of a few percent of

diborane, B_2H_6, into the gas mixture. Upon dissociation, diborane will release the atoms and enabling B-doping of diamond. The energy for activating conduction in the B-doped layer is reduced to 0.37 eV. With its smaller atomic radius, boron fits into the tight diamond structure. But for donor atoms to the right of carbon in the periodic table, the converse poses a challenge to the development of n-type doping [Ashfold et al., 1994].

The conductivity of diamond is controlled during CVD via boron concentration and crystal structure. At very high concentrations, metallic-type conduction is achieved [Isberg, 2009]. Indeed, beyond a level of 10^{21} cm^{-3} the conduction is not thermally activated anymore. Rather, it resembles conduction in a metal, with zero activation energy. A typical value for the resistivity ρ is 10^{-3} Ω cm for microcrystalline diamond. For comparison, graphite has $7 \times 10^{-6} < \rho < 4 \times 10^{-5}$ Ω cm. Nanocrystalline diamond has the lowest conductivity, due to the larger density of grain boundaries. The crystal structure controls the carrier mobility. A typical value for single-crystal CVD diamond is 3800 cm^2 V^{-1} s^{-1} [Kasu, 2009]. However in microcrystalline diamond it falls to 1200 cm^2 V^{-1} s^{-1}, which is comparable to silicon (1450 cm^2 V^{-1} s^{-1}) [Bruzzi, 2009]. The majority carriers are holes in diamond and electrons in silicon.

In electronic device applications, the breakdown voltage and the quality of the electrode contacts with the outer electrical circuit are of paramount importance. Ideally ohmic contacts are sought for, in which resistance is independent of the applied voltage. This can be achieved through metallization of a heavily doped diamond layer with carbide forming metals. For the latter the list includes Ti, Zr, Hf, V, Nb, Ta, Cr, Mo, W [Ferro, 2002]. Other metals with the required electrode properties are added on top of that, which do not react with carbon but bond with the above elements. The list includes: Cu, Ag, Au, Zn, Cd, Hg, Ga, In, Tl, C(graphite), Ge,

Sn, Pb. The resulting contacts combine electrode and adhesion quality, a common example being gold-on-titanium (Ti-Au) [Bruzzi, 2009]. In terms of breakdown, due to its wide bandgap, the maximum sustained electric field is around 10^8 V/m [Kasu, 2009]. This obviously benefits diamond-based insulating layers. But it is also essential for diamond electrodes since a high breakdown voltage widens the operating window in which no short-circuit would damage them.

The thermal properties of CVD diamond make it all the more apt for microelectronics applications [Kasu, 2009]. It shows negligible temperature increase during operation. At 1 W input power, the rise was less than for any other semiconductor. And when forced to operate at high temperature, the carrier mobility was not affected. The carrier (hole) mobility actually becomes temperature independent above the threshold boron concentration cited above [Isberg, 2009].

2.1.4 Fine Control of Surface Properties

The previous section focused on properties of diamond films that are controllable during film growth. These are mainly related to the nature and structure of the crystal atoms inside the bulk of the layer. Further electronic properties are linked to the surface conditions. This section discusses the surface properties of the deposited films and how they can be controlled.

Surface properties affect the electron emission characteristics of the diamond film. Secondary emission by Auger emission — introduced in Chapter 1 along with its coefficient, γ — is mediated by the ionization potential of incoming ions, $\mathcal{E}_{\text{iz}}$. It was shown to play a key role in plasma ignition and stability. The condition for it to occur is:

$$\mathcal{E}_{\text{iz}} > 2(\mathcal{E}_g + \chi) \tag{2.1}$$

$\mathcal{E}_g$ is the semiconductor bandgap: the energy difference between the conduction band minimum and the valence band maximum. χ is the electron affinity: the energy barrier for an electron escaping from the conduction band minimum. The right-hand side corresponds to the energy barrier for extracting two electrons from the surface; one neutralizing the ion and one net electron released into the plasma.

Electron emission depends on the type of *termination* of the diamond surface. This designates the non-carbon atoms that complete the free carbon bonds at the end of the CVD process. An electric dipole moment results, perpendicular to the surface, due to the difference in electronegativity of the bonded atoms. It can either impede (positive χ) or favour (negative χ) the emission of an electron. For instance hydrogen, less electronegative than carbon, leads to *negative electron affinity* of the surface. The converse occurs with oxygen, the other usual termination for CVD diamond. The significance of electron emission is evident in plasma display panels (PDP). MgO is usually the high-γ material of choice for coating the electrodes in each pixel, thereby enhancing their performance. [Bachmann et al., 2001] reported on the higher γ for H-terminated films compared with MgO.

H-termination actually represents an alternative source of (surface) conduction to "standard" hole (bulk) conduction described above [Kasu, 2009]. As a result of the negative χ, a current channel is set up with holes as charge carriers. Whereas bulk conduction was seen to rely on the crystal structure, surface conduction depends on the state of the H-layer; i.e. atoms *adsorbed* on — i.e. attaching to — the surface can modify its electronic properties, intentionally or not. For instance O-termination can be used instead, in order to inhibit conduction on specific regions of a microelectronic circuit. H-termination simply consists in exposing a surface to H plasma prior to air.

2.2 Gas Temperature Measurements

This section explains an established technique for measuring the gas temperature in a plasma via emission from N_2, a technique that is used to determine gas temperature in the microplasma studies presented in Chapter 5 *MICROPLASMA-DIELECTRIC INTERFACE*. In this method, emission from vibrational and rotational transitions in N_2 is used to determine vibrational and rotational temperatures for the molecule, and the rotational temperature is then taken as being representative of the molecule's translational temperature.

This explanation starts with a discussion of the rotational and vibrational excitation of molecules in a plasma environment. Next, the N_2 *second positive system* is described. Finally the coupling of its UV emission to the temperature of the background gas is presented, which is the key to using this technique as a remote temperature diagnostic tool.

2.2.1 Rotational and Vibrational Excitation

The notation used in the upcoming paragraphs is best explained by way of an example. A transition of interest in N_2 occurs between the states C $^3\Pi_u$ and B $^3\Pi_g$. The orbital angular momentum is indicated for molecular states with an upper case greek letter [Lieberman and Lichtenberg, 2005], e.g.: Σ, Π, Δ for $\Lambda = 0, 1, 2$, respectively. The upper case roman letter distinguishes between electronic states, increasing in energy with alphabetical order. The ground state is conventionally labelled X. The multiplicity, $2S+1$, is obtained from the total spin, S, and written as the superscript prefix to the greek letter. The wavefunction of a homonuclear molecule like N_2 can either conserve or change its sign when describing the situation of interchanged nuclei. The symmetry of the invariable wavefunction is highlighted by the subscript g, from the German word for even: *gerade*. The antisymmetric wavefunction receives

the subscript u, for *ungerade*: odd. A selection rule forbids any transition between two even or two odd states.

In addition to their electronic states, molecules possess vibrational and rotational energy states. The respective symbols and typical magnitudes of the energy separation between these states are $\Delta\mathcal{E}_v \sim 0.2$ eV and $\Delta\mathcal{E}_J \sim 0.01$ eV, to be compared with $\mathcal{E}_e$ in the eV range [Lieberman and Lichtenberg, 2005]. Fig. 2.3(a) — reproduced from [Herzberg, 1950] — is an energy level diagram for two electronic states A and B, showing their respective vibrational (v'' and v') and rotational (J'' and J') states. The above three scales of energy are highlighted with three double arrows increasing in length from rotational, vibrational through to electronic transitions.

Focusing on emission spectroscopy, an electronic transition occurs between (a certain vibrational level of) an excited state and *a range of* vibrational levels in the lower state. By convention the upper and lower vibrational states are respectively described by v' and v''. For instance a group of transitions with $v' = 0 \rightarrow v'' = 1, 2, 3, 4$ would translate into four emission peaks. Their separation corresponds to $\Delta\mathcal{E}_v$ and their wavelength increases with v''. Each vibrational *band* consists of a fine rotational structure resolved at $\Delta\mathcal{E}_J$.

If the upper and lower vibrational quanta have similar magnitudes, bands form characteristic *sequences* with constant $\Delta v = v' - v''$ [Herzberg, 1950]. An example is displayed in Fig. 2.3(b), reproduced from [Bayram and Freamat, 2012]. The lower diagram in Fig. 2.3 shows various transitions in the UV region for the N_2 *Second Positive System* (SPS); the topic of the next section. They are grouped in sequences, with the corresponding Δv indicated above and energy levels on the right-hand side. The peaks in the spectrum on top of it match the underlying arrows and are labelled with the values of $v' - v''$.

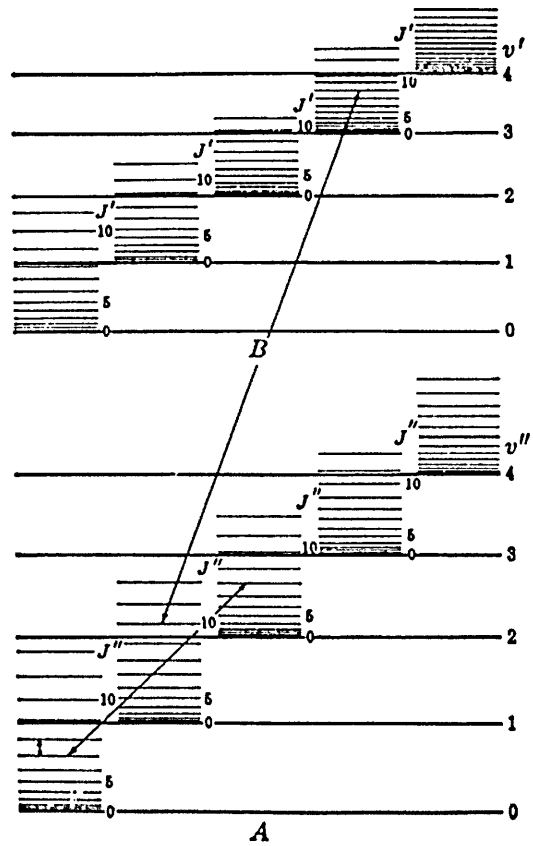

(a)

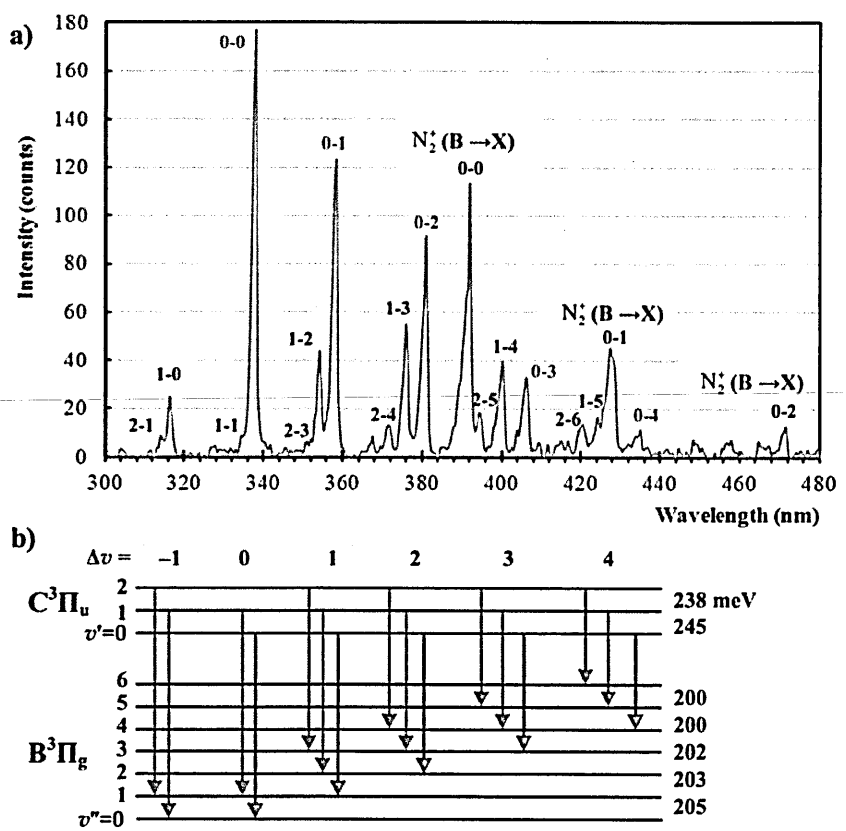

(b)

Figure 2.3: (a) Energy level diagram for electronic states A and B with their vibrational (v'' and v') and rotational (J'' and J') states [Herzberg, 1950]. (b) Constant Δv sequences from N_2 SPS [Bayram and Freamat, 2012].

When taking into account the rotational states in vibrational (de-)excitation, the selection rules lead to grouping in so-called *branches* [Herzberg, 1950]. As outlined earlier, a peak (more precisely a vibrational band) in Fig. 2.3(b) is made up of electronic, vibrational and rotational contributions:

$$\nu = \nu_e + \nu_v + \nu_r$$

The first two terms are constant for a given band. For the rotational quantum number J, the selection rule is $\Delta J = -1, 0, 1$ and gives rise to three series of lines, respectively the P, Q and R branches. Expanding the ν_r term above into rotational terms of the upper (F') and lower (F'') states yields:

$$\nu = \text{constant} + \left\{ \begin{array}{ll} F'(J-1) & \text{(P branch)} \\ F'(J) & \text{(Q branch)} \\ F'(J+1) & \text{(R branch)} \end{array} \right\} - F''(J) \qquad (2.2)$$

The branching creates band-heads in molecular emission spectra [Herzberg, 1950]. The expression above is in fact of the quadratic form — in m^2 — referred to as a *Fortrat parabola.* Each line in the fine structure is numbered by a value of that integer m. Although beyond the scope of the current discussion, this helps visualize the origin of the shading in the emission spectrum. Plotting the above ν as the wavenumber on the abscissa and m on the ordinate results in a diagram such as Fig. 2.4 (reproduced from [Herzberg, 1950]). The head-forming branch and m may vary and lines from different branches — P and R in this graph — may coincide. The band resolved in this figure occurs at 388.3 nm in the CN spectrum. Underlying the graph is a spectrum at the same scale, demonstrating the accumulation of spectral lines around a *band-head*; towards the lower wavenumbers. What is of interest here

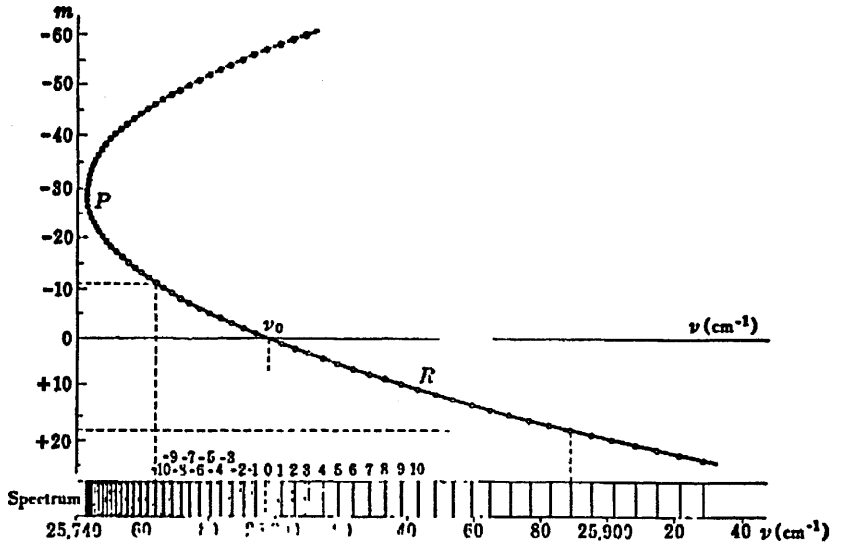

Figure 2.4: Fortrat parabola and the concept of band-head [Herzberg, 1950].

is how this results from branching. This is indeed a characteristic of the molecular system that is discussed next.

2.2.2 N_2 Second Positive System

This section focuses on one particular set of transitions in molecular nitrogen, the set that is relevant for determining gas temperature. Previously the fine structure of molecular spectra was introduced in terms of the quantization of vibrational and rotational degrees of freedom. In particular, the condition for vibrational bands occurring in sequences of constant Δv was explained as well as the appearance of band-heads. Attention is now drawn to the so-called N_2 second positive system. Its excitation and relaxation mechanisms are explained and linked to the thermal state of the neutral background gas in a plasma.

The N_2 second positive system consists of C $^3\Pi_u - $ B $^3\Pi_g$ transitions. The N_2(C) state gets populated from the vibrational ground state X $^1\Sigma_g$. Electric dipole emissions occur in the UV and visible regions (see Fig. 2.3(b)). The narrow separation

of the rotational levels allows their description in terms of a Boltzmann distribution. Therefore a *rotational* temperature, T_{rot}, can be assigned to the corresponding vibrational band. In fact, the aforementioned figure exemplifies a too-low resolution spectrum in which the rotational structure of the bands is not detected.

T_{rot} in the excited $N_2(C)$ and ground $N_2(X)$ states can be equalled under certain circumstances. Stepping back to the electronic level of the molecule, its value $\mathcal{E}_e$ depends on the interatomic distance, R. However the typical electron-neutral collision interaction time ($t_c \sim 10^{-16}$–10^{-15} s) is shorter than the molecular vibration time ($\tau_{\text{vib}} \sim 10^{-14} - 10^{-13}$ s) [Lieberman and Lichtenberg, 2005]. As a result R is assumed fixed during electron excitation in the so-called *Franck-Condon principle*. Therefore, under this excitation mechanism, the rotational quantum number of the $N_2(C)$ state is that of the original ground state. In other words $T_{\text{rot},C}$ gives a measure of $T_{\text{rot},X}$. Furthermore, the $N_2(X)$ state is in rotational-translational equilibrium with the neutral gas at the high pressures of interest in this thesis ($\sim 10^2$ torr). Consequently $T_{\text{rot},C} \approx T_{\text{rot},X} \approx T_g$.

2.2.3 Gas Temperature Coupling

This section explains how the above N_2 SPS characteristics are applied to extract the gas temperature in a nitrogen-containing discharge. A common limitation is also presented.

With its second positive system N_2 offers a convenient diagnostic tool. Nitrogen in the discharge can either come as an impurity or added to the background gas. A fraction of a percent is enough to conduct gas temperature measurements. The resulting emission in the near UV is prominent and therefore easily detected. Various transition sequences are available for this type of study. The most intense lines

corresponding to $\Delta v = 0, 1, 2, 3, 4$ were highlighted in red in Fig. 2.3(b).

The gas temperature is obtained by fitting simulated and experimental spectra. The former is generated by computing the relative positions and intensities of the P, Q and R branches of the N_2 emission from molecular constants. An initial value of T_{rot} is given to the algorithm as an input fitting parameter. Then the algorithm iterates over new values until a best fit is achieved with the measured spectrum. Under the coupling conditions outlined above, the final value is therefore equivalent to T_g.

Limitations of this technique are known in the presence of argon. In this case the assumption of $N_2(C)$ excitation driven by direct electron excitation of $N_2(X)$ is flawed. Indeed in the discharge, the energy of argon metastables, Ar_m^*, matches the excitation energy of the latter. This mechanism of heavy-paticle collisions is all the more important at high pressure. Various studies have recently focused on this phenomenon. Building on previous studies that showed the prominent influence of argon at high values of J', [Wang et al., 2007] developed a two-temperature fitting method for their experimental data. The resulting better agreement at low J' improved the confidence in the model results. In [Friedl and Fantz, 2012] experimental spectra were studied for N_2-Ar mixtures ranging from 0.1 to 100 % of nitrogen. The dependence on pressure of various reactions was also investigated and all results were compared with a model.

The general conclusion of these works is that evaluating the gas temperature via the N_2 SPS with argon present leads to an overestimation of T_g. The thermal studies reported in Chapter 5 were conducted in argon as well as helium and so this problem does not concern the latter. Its significance will be discussed in the next chapter in section 3.5 *N2SPS Fitting*.

Chapter 3

METHODS

This chapter presents the experimental methods for the operation and characterization of the microplasmas. Describing the microplasma behaviour can be done in a number of ways, prompting the following chapter structure.

Section 3.1 *General Set-Up* introduces the laboratory environment designed for the current research. Section 3.2 *Electrical System* details the electrical aspects of experimental measurements. In Section 3.3 *Optical Imaging*, the equipment for the visual observation of the microdischarges is described. A more specific set-up is the topic of Section 3.4 *Optical Emission Spectroscopy.* The results of the latter serve as input for the temperature measurement technique. For that purpose, section 3.5 *N2SPS Fitting* describes the algorithm employed to extract the gas temperature from N_2 spectra.

3.1 General Set-Up

The present section lists the general tools and parameters used to conduct all the studies reported in this thesis. A more specific description of the various microplasma reactors is the topic of the following chapter.

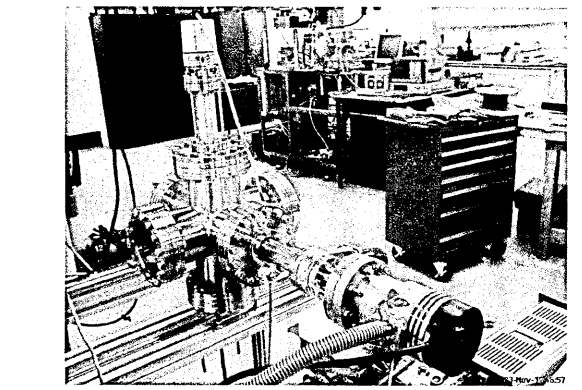

(a)

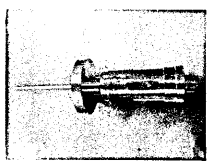

(b)

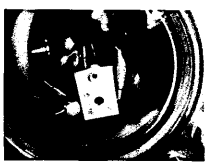

(c)

(d)

Figure 3.1: General set-up for microplasma operation and study.

The vacuum chamber assembled for this research is depicted in Fig. 3.1. It consists of a stainless six-way cross, with the following items:

- all evacuation components are localized in the foreground. A turbo-pump (LEYBOLD VAKUUM: Turbovac 50, 1200 Hz) is identified by its black cylindrical power supply unit. It is connected via the flexible hose to a backup roughing pump (EDWARDS: 5 Two stage E2M5); not visible. These items can be isolated from the vacuum rig by a gate valve (VAT: A-594306); offering pressure control with minimal handling of the pumps.

- a pressure gauge (PFEIFFER VACUUM: Compact FullRange Gauge PKR251) sits on top of the rig as a white cylinder. Its "Dual Gauge" controller (PFEIFFER VACUUM: TPG262) cannot be seen.

- a flange (facing the red chest of drawers) contains a linear translator (MDC VACUUM LTD.), depicted in Fig. 3.1(b). This offered control on the distance between the micro-device and the measuring apparatus, fine-tuned with a micrometer scale.

- at the bottom left of the photograph and across the chamber from the previous flange, a viewing port (window flange) is visible. All diagnostic equipments were set up on an adjacent optical table. Fig. 3.1(c) shows a white device holder at the end of the translator; with the red and yellow electrode clips (more on this later).

All of the microdischarge operation was conducted inside a controlled atmosphere. The above equipment could achieve very high vacuum. However its sole purpose was to offer a controllable and reproducible working environmnent. Prior to microdischarge ignition, the vacuum chamber was evacuated to 1×10^{-5} torr then backfilled with the required gas (mixture). Research grade argon or helium were supplied to the chamber via a system of overhead taps. During temperature measurement experiments, 0.5% per volume of nitrogen were added. Between two experiments at different pressures, the power supply was always turned off and the chamber evacuated.

3.2 Electrical System

The electrical equipment and measurements are now presented.

The electric circuit was made up of a high-voltage power supply (STANFORD RESEARCH SYSTEMS: PS325/2500V-25W), a micro-reactor connected inside the chamber and two 68 kΩ wire-wound carbon film resistors (RS COMPONENTS: nr 132-933, 0.5W) in series. Electrical contact with the micro-device electrodes was achieved by mechanically pressing 8-μm tantalum foil (ADVENT RESEARCH MATERIALS: TA213911) strips against the corresponding surface. These strips were in turn connected to the circuit wiring through crocodile clips. In Fig. 3.1(c), the yellow and red clips connected the back and front electrodes, respectively. Halfway between those, the microplasma device is made apparent by a cutout in the white holder.

PTFE holders were purpose built to house the microplasma devices inside the vacuum chamber. Their dual goal was to offer mechanical support and ensure consistent and reliable electrical connections. Once mounted, the microplasma reactor system comprised the following sandwich, from front to back in Fig. 3.1(c): a PTFE layer (white in the photograph), a tantalum foil, the micro-device, a tantalum foil, a PTFE layer. Mechanically, four plastic screws pressed the PTFE layers together, thereby immobilizing the reactor and ensuring good electrical contacts. Electrically, the device holder increased the separation between opposite contact polarities, thereby ensuring that breakdown would occur inside the cavity, e.g. as opposed to between the crocodile clips. As can be seen in Fig. 3.1(c), a 10-mm diameter circular cutout allowed continuous observation of the cavity.

The electrical characterization was conducted via a digital oscilloscope (TEKTRONIX: TDS 2014 B). High-voltage probes continuously read the gap voltage: the potential difference between the powered electrode and ground. The applied voltage was increased in 10 V maximum increments until breakdown was reached. Subsequent increments depended on the experimental goals and constraints, ranging from 10 to 100 V. All steps of voltage and current were recorded. The latter came from the power supply read-out, compared to concurrent output of a digital multimeter (FLUKE: 27 II).

3.3 Optical Imaging

In this section, the optical gear is described, along with the good practice established to perfect the development and characterization of microplasma reactors and sources.

All imaging was conducted with the device held face-on behind the viewport of the vacuum chamber. The set-up in Fig. 3.1(c) is shown magnified during microplasma operation in Fig. 3.1(d). An optical table lay adjacent to the general set-up presented above. This isolated the diagnostic hardware mechanically from the operating equipment. The stable, bread-board type table enabled an accurate and reproducible horizontal and vertical alignment of all the optics.

A USB digital microscope (ANMO ELECTRONICS CORPORATION: Dino-Lite AM-4013 TL) served as the general tool for visual characterization. Offering photographic, video and live feed functions, it facilitated the set-up, calibration and visual control of every experimental procedure. Its built-in magnification was sufficient to study the development of a microplasma in and around the cavity; e.g. when coupling observation with electrical measurements for investigating the cathode side expansion.

More accurate imaging was carried out with intensified charge-coupled device (ICCD) cameras. The two models used were the STANFORD COMPUTER OPTICS 4 Picos-DIG and the ANDOR 460 model DH534-18F-01. Both allowed time-resolved measurements. They were used behind magnifying optics in order to characterize the spatial distribution of the microplasma inside the reactor.

Magnification of the microplasma source during operation was achieved through the following combination of optical elements. A 1″, f=50.0 mm visible achromat (THORLABS: AC254-050-A-ML) was maintained 75 mm from the object under observation. A 10x microscope lens (OLYMPUS: Plan N) was 115 mm away from the achromat. The magnified image was focused 270 mm behind the front of the 10x lens. In this configuration, the magnification was determined by substituting

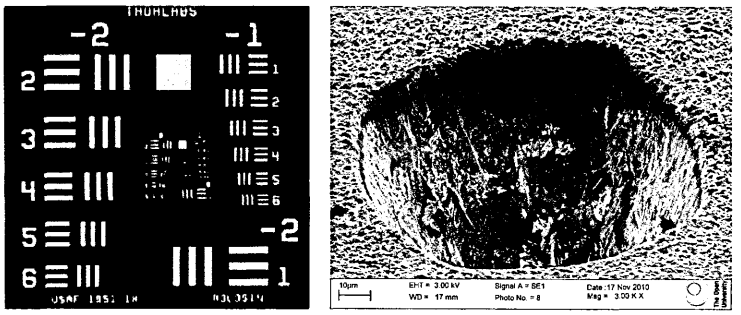

(a) (b)

Figure 3.2: (a) Test target for calibrating and measuring the magnification of the optical system. (b) SEM of a diamond-based micro-reactor.

a $3'' \times 3''$ negative test target (THORLABS: USAF1951, R3L3S1N) for the object. Fig. 3.2(a) illustrates the increasingly smaller periodic pattern occurring on the target. A look-up table converts the identification number of the smallest grid being in focus into an optical resolution. Under back-illumination, the magnification for the above optical system worked out to $\times 14$. This value offered the best compromise between image size, number of optics and length of the complete optical train.

When further magnification was necessary, a *Scanning Electron Microscope* (SEM) was employed (ZEISS: SUPRA 55VP). Fig. 3.2(b) depicts a micro-cavity prototype for this research. The SEM was used to identify the various layers of CVD diamond:

- from the bottom nearly all the way up, the B-doped diamond wafer (obtained commercially) is more or less uniform
- the top surface and rim consist of microcrystalline B-doped diamond deposited by CVD by this research consortium
- between the two, a thin dark band (most visible on the right- and left-hand sides of the rim in the above picture) was identified as the undoped diamond layer, also deposited for this work.

Such high-resolution micrographs assisted in the resolution of device breakdown problems. Having linked the latter with a too thin dielectric layer, subsequent

consortium meetings ordered that CVD start with a (250-μm) thick commercially available undoped wafer. The electrodes were then applied, as described in the next chapter. The various coloured patches on the cavity walls were not unambiguously identified. However they led to the critical decision of systematically acid-cleaning the reactor holes as the ultimate packaging step. This was designed to remove any potential unwanted conductive graphite patches resulting from laser ablation of diamond.

The signal-to-noise ratio was maximized for optical as well as spectroscopic measurements (discussed next). Indeed, from the viewing port to the entire optical table, the laboratory area was kept under a shroud during all operation. The individual lenses were further obscured by connecting them with an optical tube (THORLABS).

3.4 Optical Emission Spectroscopy

This final section on experimental equipment discusses *Optical Emission Spectroscopy* (OES). The hardware is first described, followed by its calibration and resolution.

The following monochromator was used in conjuction with either of the ICCD presented above: HORIBA JOBIN-YVON Triax 320, nr 07435D-04-05. A low resolution 300-mm^{-1} and a higher resolution 1800-mm^{-1} gratings were available, blazed at 500 nm. Alignment (horizontal and vertical) with the optical system and source was carried out with a laser. It was first shone from the approximate position of the centre of the ICCD, i.e. behind the monochromator. In so doing, the internal mirrors of the latter, the optics in front of it and the micro-cavity inside the vacuum chamber were all aligned. Next the laser was substituted for the micro-reactor, allowing a fine adjustment of the x-y position of the ICCD.

The entrance slit width was optimized by measuring the spectral resolution with visible He-Ne laser at 632.8 nm. It was set up behind a ground glass diffuser (THORLABS: 1.0″, 120 GRIT, DG10-120-MD), again at the position of the microplasma. Openings from 30 to 100 μm were compared on the basis of the full width at half maximum of the ICCD signal. The resolution was sensibly less at 100 μm and the signal significantly weaker for the 30 μm opening. The best resolution of 0.1 nm was obtained with the final slit width of 50 μm. Equally importantly, it turned out that, over the whole range of microplasma operation, the signal was too weak for smaller openings and overexposed at larger ones.

The signal-to-noise ratio was optimized, as explained above for optical imaging. In addition, between every spectrum recording, a background signal was acquired and subtracted from the corresponding data.

3.5 N2SPS Fitting

The algorithm used to obtain the gas temperature results reported in this thesis is now described. From the emission spectrum of the N_2 SPS, data extraction follows the technique explained at the end of the previous chapter. The model was used under the guidance of one of its authors, P. C. Johnson.

An algorithm, which shall be referred to as `N2SPS`, computes rotational and vibrational temperatures; T_{rot} and T_{vib}. It uses the sequence with $\Delta v = 2$ in the C $^3\Pi_u$ – B $^3\Pi_g$ system. In particular the lines corresponding to $v' - v''$ transitions $0-2$ (at 380.5 nm) and $1-3$ (375.5 nm) are analyzed. With transition probabilities studied by the model authors in [Hartmann and Johnson, 1978], T_{vib} is derived from the relative intensities of the vibrational band-heads. Furthermore, T_{rot} is computed from the shapes of those vibrational bands. The P, Q and R branches are evaluated,

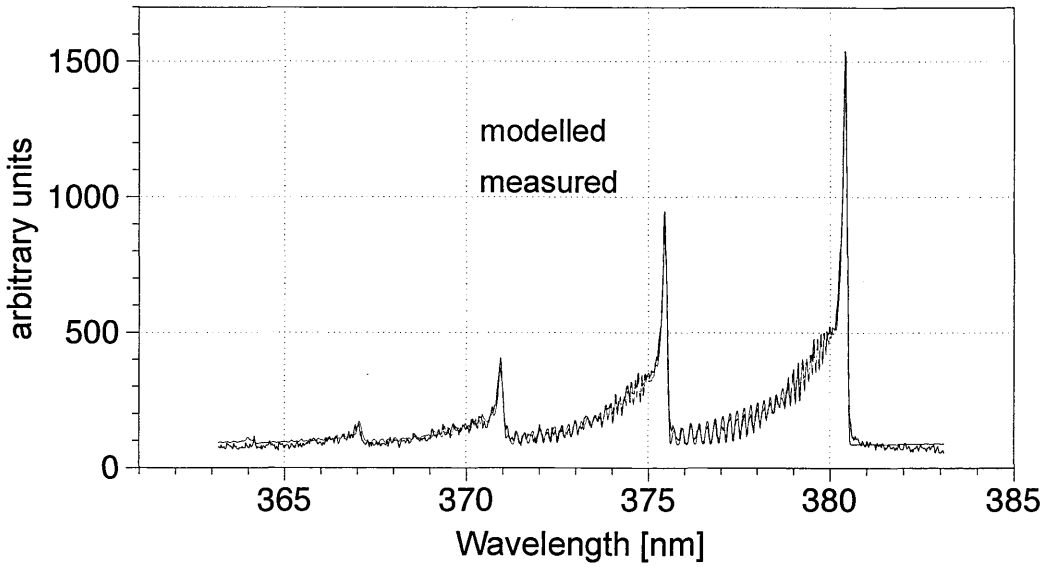

Figure 3.3: Example from the current research of a model fit (red) of the measured spectrum (black) of the N_2 Second Positive System. Between the vibrational band-heads, the rotational levels are resolved.

based on rotational terms from [Herzberg, 1950], up to rotational terms $J = 80$. The resolution of the rotational levels can be seen in Fig. 3.3 between the peaks or *vibrational band-heads.*

The position and resolution of the spectral lines are analyzed prior to the actual fitting. A MATHCAD program detects the band-heads in the output data from the ICCD and corrects their wavelengths. A slit function is automatically applied, starting from an initial input value, that iteratively determines the spectral line broadening that corresponds to the measured spectrum. The limit in spectral resolution was attributed to the optical system.

Another MATHCAD program, that calculates the model-data best fit, does so with four parameters. The values of T_{rot} and T_{vib} are provided as input and subsequently iterated over. The background emission level is determined and subtracted in the early stages of the simulation. The population of the $N_2(C)$ state provides a

measure of the emission intensity. Finally a Levenberg-Marquardt algorithm (run by the MATHCAD Genfit function) combines those parameters to fit the resulting model spectrum to experimental data. The algorithm was tested in a previous research at the Open University with the same measuring equipment [Sutton, 2011] against an established model (Specair) and another Levenberg-Marquardt method. An average uncertainty of 7% was then determined from test spectra comparisons. This is taken in later chapters as the uncertainty in the temperature values. In addition, given the limitations arising for N_2 SPS coupling with argon-based measurements (see end of the previous chapter), the corresponding values will be interpreted as maxima.

Chapter 4

MICRODISCHARGES IN DIAMOND SUBSTRATES

4.1 Introduction

The aim of the research reported in this chapter was to achieve the first operation of diamond-based devices and make preliminary comparison of their operating characteristics with those obtained from similar microhollow cathode devices by other researchers. Part of this work has been reported more concisely in [Mitea et al., 2012]. A key aim was to confirm the suitability of diamond-based reactors for this and future microplasma research.

Prior to any experimental study, the design and fabrication of the aforementioned devices was the result of a consortium comprised of partners based at the University of Bristol and the STFC Rutherford Appleton Laboratory (RAL). In the School of Chemistry at the former, a team of diamond experts led by Professor Paul W. May[1] were in charge of the diamond insulators and electrodes in the microplasma

[1]Dr Neil A. Fox, Dr Judy Hart and PhD student Monika Zeleznik (EPSRC grant EP/G069980/1).

reactors. At RAL, work in the Micro and Nanotechnology Centre[2] was conducted by Professor Robert Stevens[3] and Chantal Fowler on the use of novel techniques for laser drilling microcavities and device packaging.

The current author's contribution to the design and packaging consisted of discussion and feedback on device performance rather than direct fabrication. A brief description of this process is nevertheless necessary. This is given in Section 4.2.

The rest of this chapter is divided as follows. Section 4.3 presents observations and measurements of the performance of the first diamond-based devices. Section 4.4 contains a discussion of these results, including comparisons with experiments and theoretical descriptions reported by other research teams.

4.2 Diamond-Based Micro-Reactors

4.2.1 Fabrication

The diamond-based devices were based on 250 μm-thick substrates of polycrystalline diamond insulator. The two principal designs are represented schematically in Fig. 4.1. Their common substrate, formed of insulating diamond and shown as the larger black square in the figure, was obtained from Element Six as mechanical-grade freestanding 10×10 mm^2 wafers[4]. This determined the dimensions of the final devices. The undoped substrate was therefore the central part of the electrode-dielectric-electrode sandwich.

The device shown in Fig. 4.1(a) consists of the insulating substrate with additional layers of boron-doped diamond deposited on each side of the wafer. The boron-doped diamond is semiconducting and so these layers act as the electrodes

[2]EPSRC grant EP/G060886/1
[3]Now Professor in Smart Materials and Devices - Nottingham Trent University.
[4]Product code 145-500-0015.

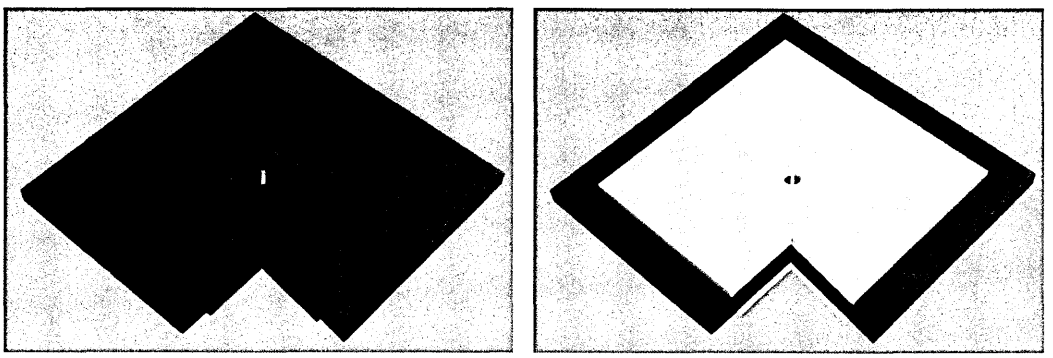

(a) (b)

Figure 4.1: Diagram of diamond devices. A central hole is shown, along with a cut-out of the electrode-dielectric-electrode sandwich. (a) B-u-B, B-doped–undoped–B-doped diamond and (b) G-u-G, gold–undoped diamond–gold.

in the final microhollow cathode device. The discharge cavity was formed by laser drilling a hole through the three-layered substrate. For the rest of this thesis, these devices, formed of a B-doped diamond layer, the undoped insulting diamond substrate and a second B-doped conducting layer, will be referred to as B-u-B reactors.

The device shown in Fig. 4.1(b) has a similar geometry but the electrode layers are formed of titanium-gold layers deposited onto the insulating diamond substrate. These devices, consisting of a thin metal electrode, the insulating substrate and a second metal electrode, will be referred to as G-u-G devices; a mnemonic for "gold-undoped-gold".

Some preparation of the wafers was necessary prior to the addition of the electrodes. Their first treatment was a warm bath of concentrated nitric acid in order to clean off any residue from polishing. The latter was a default post-production operation on one of the wafer faces by the supplier. Depending on the type of electrode, a different team and deposition technique was involved. For the final step a central cylindrical through-hole was drilled.

The following process was used to fabricate the B-u-B devices. The boron-doped

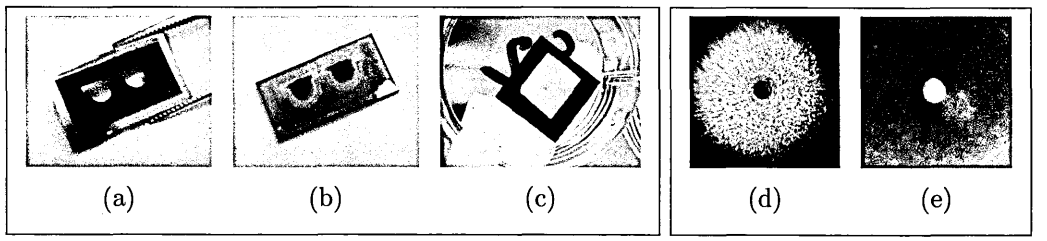

Figure 4.2: The mask in (a) prevented contamination of the substrate during deposition of the B-doped layer, which has matching shape in (b). Similarly, the substrate edges were covered during metal layer deposition (c). Close-up top view of the final micro-reactors and holes: (d) B-u-B and (e) G-u-G.

semiconductor electrodes were added by chemical vapour deposition by the Bristol team. Accidental contamination of the undoped substrate by boron impurities needed to be avoided to prevent short-circuits between the upper and lower B-doped diamond layers. Inside the CVD reactor, a silicon mask was therefore applied to cover the edges while the zone intended for diamond growth was exposed through cutouts. A photograph of a mask is presented in Fig. 4.2(a), with the resulting B-doped regions on an undoped wafer in Fig. 4.2(b). The rectangular shape follows from tests carried out on various packaging formats. Further precaution consisted in laser trimming the outer edge of the sample. The final thickness of the B-doped layer could vary between 2 and 3 μm. A 300-μm diameter hole was drilled with a Nd:YAG laser-based micro-machining system[5] and is shown magnified in Fig. 4.2(d). The sample was cleaned in $\sim$ 80°C sulfuric acid (90%) and potassium nitrate (2 g in 40 ml of acid) for 15 minutes. This was aimed to remove possible surface contamination by graphite from laser etching; offering conduction. Hydrogen termination was obtained by exposition of the device to a hydrogen atmosphere for a few minutes.

The G-u-G reactors were fabricated using the following process. Metal electrodes were added to the undoped diamond substrate by the RAL team. First, a 30-minute dehydration bake of the wafer on a hot plate removed any prior contamination. A layer of titanium (100 nm) then gold (500 nm) were deposited in an SVS E-Gun

[5]Alpha, Oxford Lasers, UK.

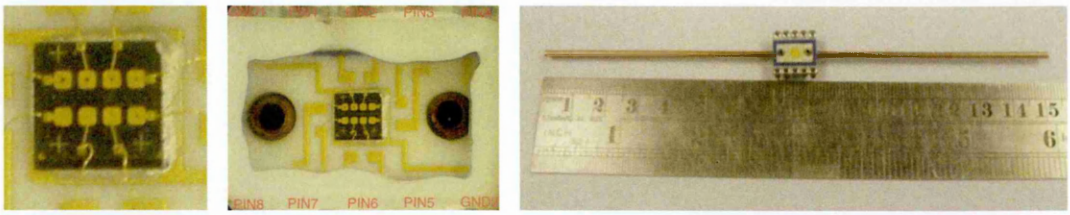

(a) (b) (c)

Figure 4.3: (a) The first prototype integrated eight microplasma reactors on a single chip. (b) They were addressed through a set of independent surface tracks and pins. (c) The whole chip was sealed and fed with copper gas pipes.

evaporator. Titanium improved the stability of the gold-diamond interface. The edges of the wafer were protected with a Kapton® adhesive tape. As with the silicon mask above, this resulted in an electrode-free border, which is visible on the face-on photograph of a G-u-G device in Fig. 4.2(c). The yellow region is gold, surrounded by the underlying black undoped diamond. Residual metal stress from the film deposition was removed by rapid thermal annealing at 500°C for two minutes. A hole was drilled with a micro-machining system based on a 355 nm diode-pumped solid-state laser[6] with a diameter of 100 or 200 μm. A magnified example is shown for the latter in Fig. 4.2(e). Finally, each device was exposed to an oxygen plasma[7] for 60 minutes in order to clean off any contamination of the diamond substrate from the fabrication process.

4.2.2 Failures and Modifications

In order to facilitate set-up and limit handling of the reactors, early designs allowed the device chips to be integrated into a single package. The result was a microplasma reactors-on-chip reminiscent of a surface mount microchip. Such a device is shown in Fig. 4.3, where 8 devices have been fabricated on a single 10×10 mm^2 wafer, complete with pads for electrical connections. The black square in Fig. 4.3(a) is overlaid by eight square gold electrodes arranged in two rows. Some of the larger

[6]This task was outsourced to Micronanics Ltd, based on the RAL premises.
[7]PVA TePla America Inc.

holes are visible in the centre of the respective electrodes, with the largest having a diameter of 70 μm. Small connecting gold wires can be seen to bond to contact pads, which look like smaller electrode squares. In Fig. 4.3(b) conductive tracks radiate from the diamond wafer, connecting each electrode (through gold bond wires) to a pin (labelled in red). The back of the diamond wafer was taken to be the ground electrode. The two rows of five pins, for mounting on a printed circuit board, can be seen above and below the blue-framed microchip holder in Fig. 4.3(c). This configuration was meant to allow switching between microplasma reactors via the corresponding pin-circuit, i.e. without handling the diamond chip itself. A sealed quartz window created a confined environment. Long copper gas pipes (left and right on Fig. 4.3(c)) were added to feed the gas in and out via the left and right circular openings in Fig. 4.3(b).

Although early designs promised simple handling and operation, there were several practical problems. In the reactors-on-chip device, discharges would occur around the wire-bonds instead of inside the cavity. It was not clear whether the failure was due to a fault in the electrical wiring or in the diamond wafer. This uncertainty was addressed by adopting single device chips, such as the G-u-G one depicted in Fig. 4.2(c). Subsequently, a single holder and electrical connection arrangement was used, as described in Section 3.2, for all devices; making fault tracking easier.

The B-u-B and G-u-G devices described earlier were both based on an insulating diamond substrate, with conducting electrodes deposited on both sides of the wafer. Another early design consisted of a conducting B-doped diamond substrate, coated with an insulating diamond layer on one side and then another conducting layer on top of that. This device had a very thin insulating layer, typically < 5 μm, decided in part to compensate for the very slow deposition rates achieved within

our consortium. It promised different operating characteristics to the devices based on a thick insulating layer. However this appeared to favour device breakdown before any possible microplasma ignition, linked to pinholes bridging the undoped diamond crystal. Also, surface conductive pathways were detected along the insulator. The above issues were identified on single devices. As a result it was agreed to base all subsequent reactors on commercially available thicker (250 μm) undoped wafers and to use the aforementioned masking procedure.

4.2.3 Success Milestones

The previous section described some problems faced during development of diamond-based microplasma devices. However, the fabrication problems were overcome with the designs shown in Fig. 4.2 and successful electrical connection was achieved with both types of discharge device. For the gold electrode devices, the electrodes were connected mechanically by pressing tantalum foils onto the gold surface, using a specially designed PTFE holder (see Section 3.2). For the boron-doped diamond electrodes however, their semiconducting nature meant that reproducible reliable contact was required. This was achieved by building on the patterning techniques from the reactors-on-chip. Contact pads in (titanium-)gold were deposited in a corner of the diamond. In addition the diamond electrode films were doped to near metallic conductivity with a measured boron concentrations of 3×10^{27} m^{-3} (estimated from calibrated SIMS analysis [May et al., 2008]).

The type of microdischarges generated inside both types of diamond-based reactors were typical of those observed in MHCD's by other teams. The operating window was confirmed by repeated operation under the intended conditions of study. The results of subsequent electrical and optical studies are reported in the next section.

4.3 Results

Electrical and optical measurements were carried out to determine the type of (micro-)discharge obtained inside the reactors described above. They also served to characterize the ignition stage and the influence of key parameters on the behaviour of steady state microplasmas. The following results were obtained in helium and argon at pressures from a few torr to beyond atmospheric pressure. In order to validate this microplasma study, the first to use diamond as the substrate material, results are benchmarked in the Discussion section against reports by other teams using similar microdischarge devices.

4.3.1 Paschen Curves and Ignition Mechanism

Paschen curves were obtained in both helium and argon microplasma and indicated conventional glow discharge ignition mechanisms. When ignition and sustainment are driven by electron avalanche between the electrodes and secondary electron emission at the cathode, the typical skewed U shape is obtained[8]. Experimental plots are displayed in Fig. 4.4 for G-u-G reactors and Fig. 4.5 for B-u-B reactors. The ordinates represent V_b, corresponding to the applied voltage at which ignition was detected visually (bright light turning on) and confirmed electrically (simultaneous current rise and voltage drop). On the abscissa is the product pd, in torr cm. Each point corresponds to a different experiment for which the breakdown conditions were recorded. The legend to the graphs indicates the diameter of the devices ranging from 100 to 300 μm. The same linear-logarithmic scale was used as in Fig. 1.4 that served to introduce the Paschen relationship. The corresponding theoretical curve appears as a black solid line, matching the A, B parameters (taken in [Lieberman and Lichtenberg, 2005]) and γ coefficients to the gas and cathode material in each graph.

[8]first presented in Figs.1.4 and 1.8, with the theoretical expression in Eq.1.21 (p. 26).

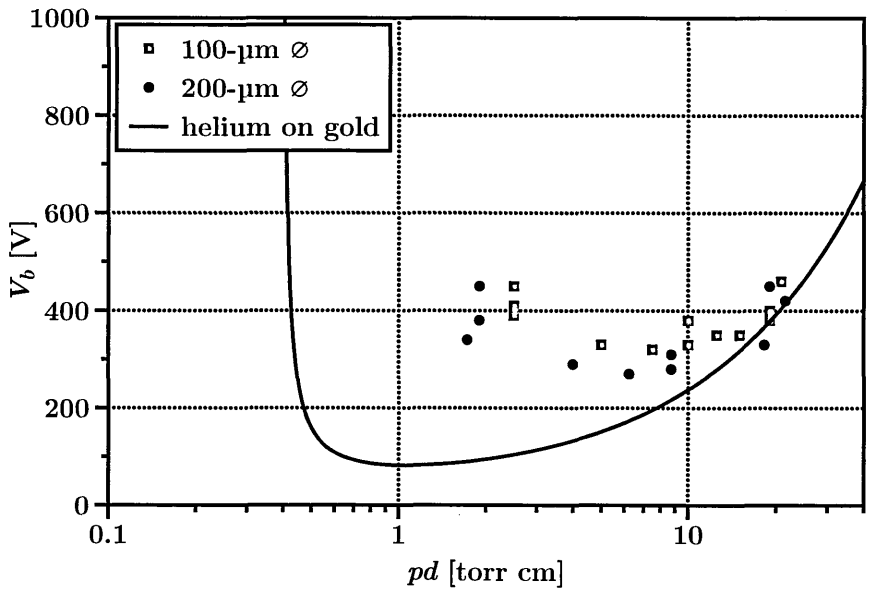

(a) helium

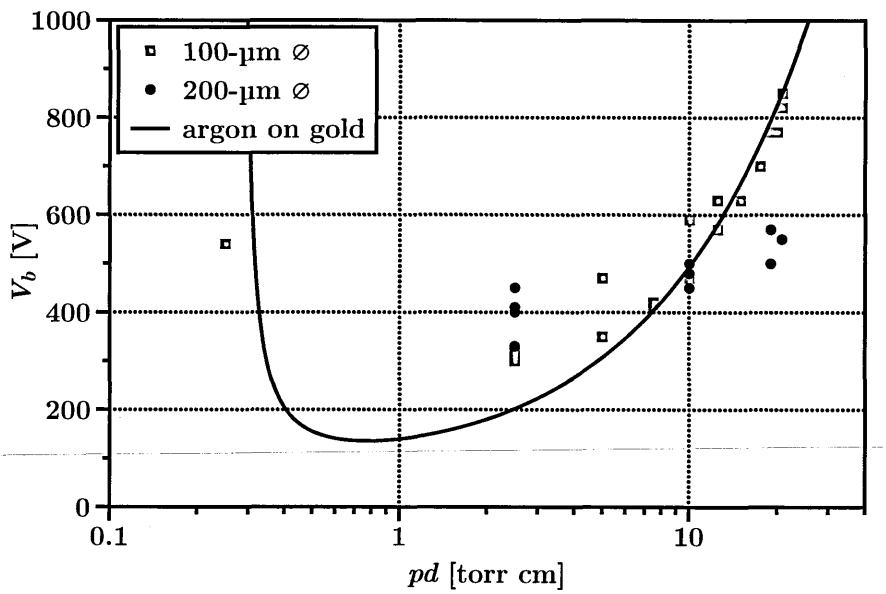

(b) argon

Figure 4.4: Paschen curves for G-u-G reactors of various diameters, D.

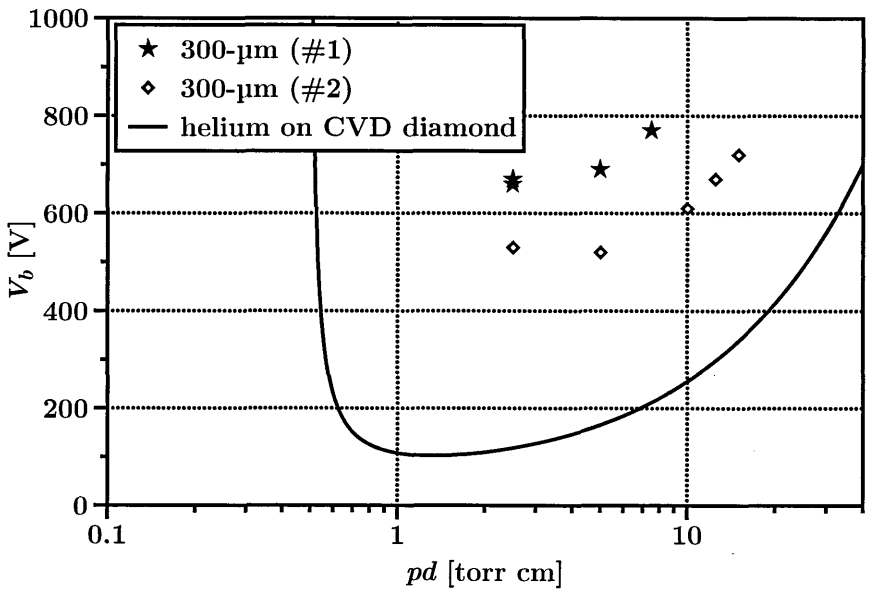

(a) helium

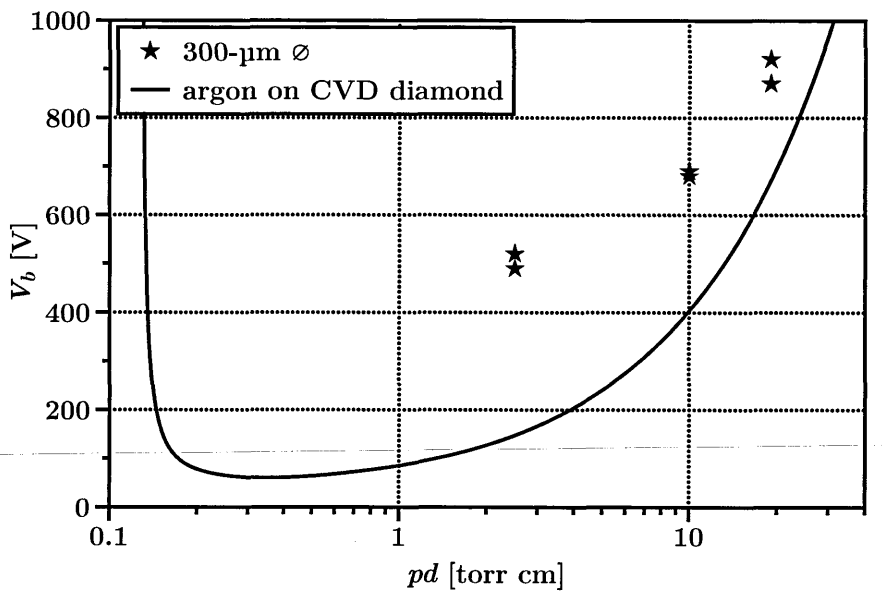

(b) argon

Figure 4.5: Paschen curves for B-u-B reactors with $D = 300$ μm.

The case of helium microplasma in G-u-G devices is illustrated in Fig. 4.4(a). The value of $\gamma = 0.5$ was taken from [Hayden and Utterback, 1964]. Results for argon microplasma in G-u-G reactors are shown in Fig. 4.4(b). The value for $\gamma = 0.04$ comes from [Lakits et al., 1990]. A minimum is observed, although it appears shifted towards higher pd and V_b relative to the theoretical curve. The shape of the curve and similarity with that of other glow discharges (discussed in the next section) nevertheless confirm the manifestation of conventional breakdown mechanisms of electron avalanche and secondary electron emission.

An overvoltage at ignition contributes to the higher experimental V_b. The microplasma can turn on at a higher voltage than its *true* breakdown value. Indeed, despite every precaution to reach the breakdown voltage gradually (10 V or less increments in this work) the microplasma would often be detected with current in the mA range.

Helium and argon microplasma data generated with B-u-B reactors is presented in Fig. 4.5. The values of $\gamma = 0.34$ for helium and $\gamma = 0.3$ for argon were taken from [Matsunaga et al., 2003]. There is a stronger discrepancy with the theory than for the case of gold cathode. The only other difference was the diameter of the cavity. On the one hand all of the graphs adopt the shape of the theoretical Paschen curve, i.e. the same evolution along the pd axis. On the other hand there is overall a significant increase in V_b. This is specifically linked to the semiconductive nature of the electrodes in Section 4.4. Still, the B-u-B reactors remain governed by the same breakdown mechanisms as above.

4.3.2 V-I Characteristics and Normal Glow Mode

In the normal mode, the V-I characteristic takes on a flat gradient. This corresponds to a constant current density mode, in which the current increase at higher

input power is accompanied by the expansion of the discharge, hence its surface area, on the cathode surface. Once the latter electrode is fully covered, any further current rise can only be sustained by a voltage increase. The resulting positive V-I gradient signals the abnormal glow mode.

Fig. 4.6 presents V-I data for three reactor configurations, obtained at 400 torr. Two G-u-G (diameters 100 and 200 μm) and one B-u-B devices are compared. The legend to each graph specifies the materials and hole diameters. Voltage (in V) is plotted against current (in mA). The value of the former corresponds to the gap or inter-electrode voltage, expressing the total potential drop across the entire microplasma. The data points were obtained by a high-voltage probe connected between the ground and the powered electrode. Alternatively, subtracting the potential drop across the series ballast resistor (132-kΩ here) from the applied voltage yielded a close value. The excess voltage obtained with the latter calculation is displayed as one-sided uncertainty bars in Fig. 4.6. Contributions to it were not systematically investigated but include a potential drop at the imperfect electrode contacts and a higher than nominal resistance due to ballast heating.

In helium, Fig. 4.6(a), the gradients for all reactors are flat or slightly positive for most of the operating range. Argon data in Fig. 4.6(b) also supports the operation in normal glow mode. The curves indeed show a flat V-I gradient. In both conditions the voltage rise is not sufficient to characterize the glow mode as abnormal, as was further confirmed by visual inspection of the microplasma growth outside its cavity.

Consistently with operation in the normal glow mode, the microplasma was actually seen to gradually cover the cathode surface with increasing current. The situation in helium is pictured at three different pressures in Fig. 4.7 and Fig. 4.8

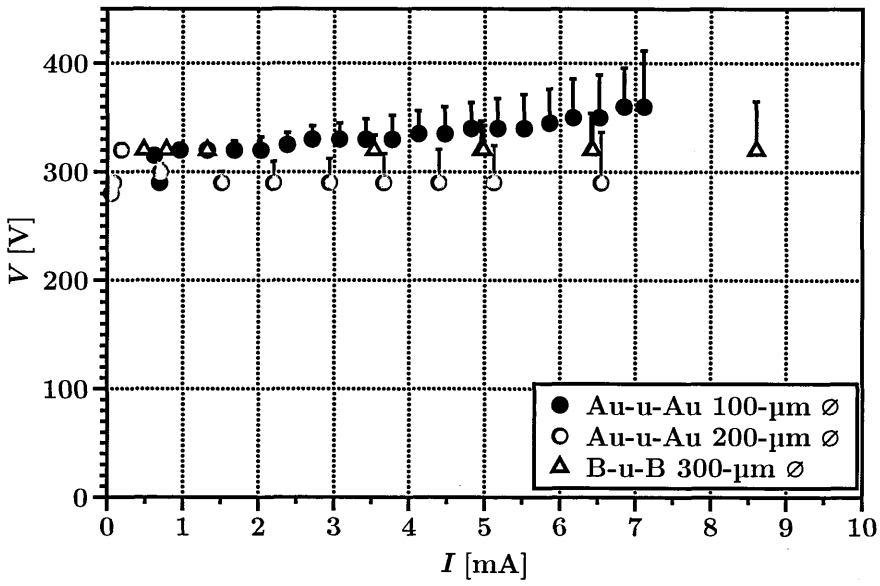

(a) helium microplasma

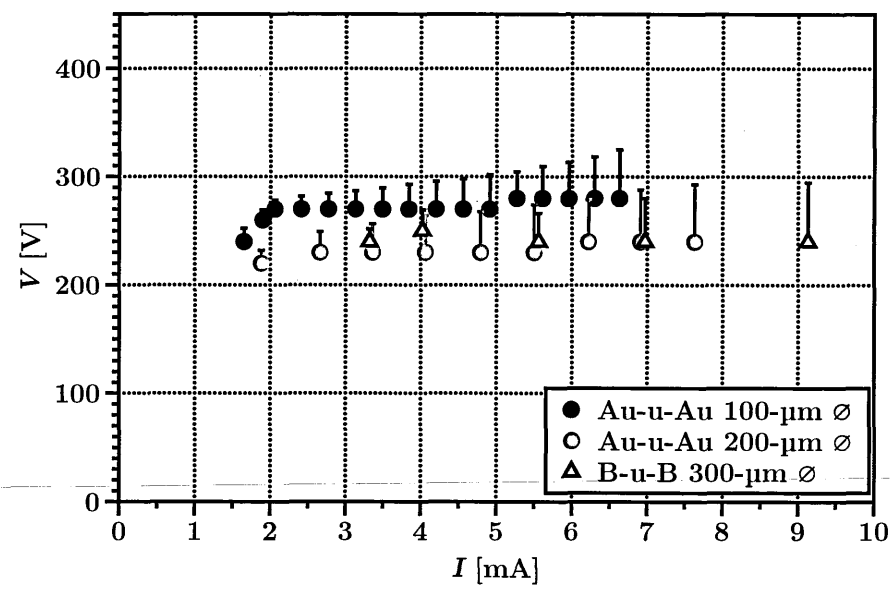

(b) argon microplasma

Figure 4.6: Gap voltage V against discharge current I, obtained by increasing the input power during discharge operation. The gas pressure was 400 torr. The reactor type and hole diameter are labelled in the key to each figure.

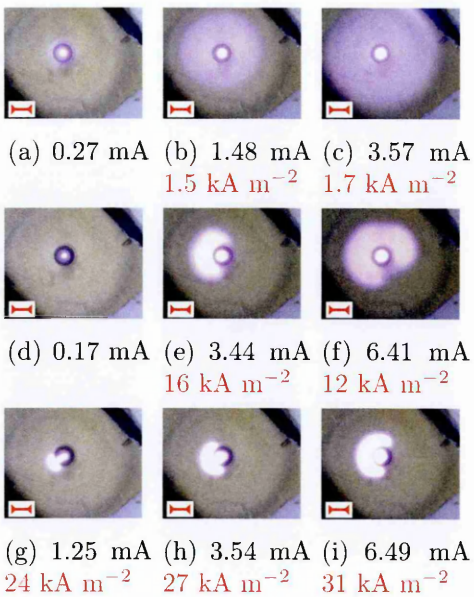

Figure 4.7: Cathode-side expansion of a helium microplasma in a 100-μm diameter G-u-G reactor at (a-c) 100 torr, (d-f) 400 torr and (g-i) 760 torr. A 100-μm red scale is visible at the bottom left of each picture.

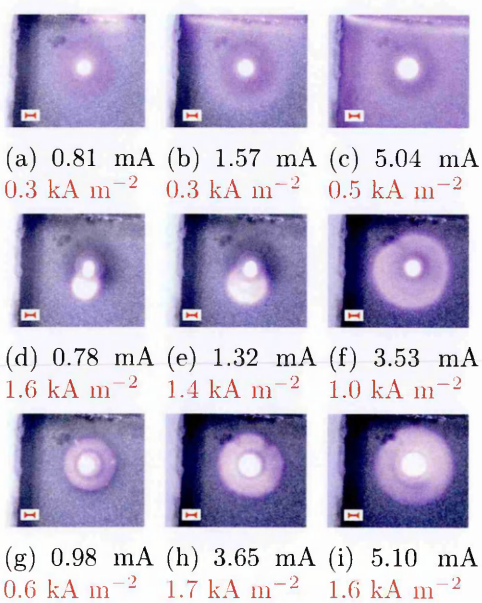

Figure 4.8: Cathode-side expansion of a helium microplasma in a 300-μm diameter B-u-B reactor at (a-c) 100 torr, (d-f) 400 torr and (g-i) 760 torr. The bright horizontal line at the top of (a–c) signals the presence of the tantalum foil used for electrical contact. A 300-μm red scale is visible at the bottom left of each picture.

for the G-u-G and B-u-B reactors, respectively. Each row of photographs was obtained by increasing the input power at constant pressure: 100, 400 or 760 torr. The caption indicates the current; in black. The current density, in red, was obtained by dividing the discharge current by the cathode area covered by the microplasma. For the area, the cross-section of the discharge inside the hole was excluded in order to emphasize the role of the cathode material around the hole (discussed next). The diameter of the hole was 100 μm for the G-u-G reactor in Fig. 4.7 and 300-μm diameter for the B-u-B device in Fig. 4.8. The same behaviour was observed in argon.

These results show that the discharge behaviour depends on the background gas pressure and on the current density of the plasma generated in the device. These two trends are examined in more detail in the next two subsections.

4.3.3 Metal vs. Semiconducting Electrodes

Current density differentiates strongly between metal and boron-doped diamond electrodes. The values in red in the caption of Figs.4.7 and 4.8 are now compared. In order to isolate the material dependence of the cathode surface outside the hole, the cross-sectional microplasma area inside the cavity was excluded in computing the density tabulated below. The area was extracted from the magnified optical images using the built-in tool for surface area computation from a microscopy software[9]. Table 4.1 compares experimental data from three different reactors: 100-μm diameter G-u-G (Fig. 4.7), 200-μm diameter G-u-G and 300-μm diameter B-u-B (Fig. 4.8). Three stages are plotted (Nr 1–3) with row colours matching the gas (helium) pressure for every device configuration.

Boron-doped diamond electrodes maintain a lower current density than gold electrodes. Microplasma expansion was more significant on the semiconducting dia-

[9]Macnification by Orbicule.

Table 4.1: Current density in helium with gold and B-doped cathodes.

Device type [⌀ μm]	**Pressure** [torr]	J [A m^{-2}] Nr 1	J [A m^{-2}] Nr 2	J [A m^{-2}] Nr 3
G-u-G [100]	100	hole limited	1.5×10^3	1.7×10^3
	400	hole limited	1.6×10^4	1.2×10^4
	760	2.4×10^4	2.7×10^4	3.1×10^4
G-u-G [200]	100	7.2×10^5	1.1×10^6	1.0×10^6
	400	2.4×10^6	5.4×10^6	5.9×10^6
	760	1.1×10^7	1.2×10^7	1.3×10^7
B-u-B [300]	100	300	300	500
	400	1.6×10^3	1.4×10^3	1.0×10^3
	760	600	1.7×10^3	1.6×10^3

mond cathode than on the gold cathode, at identical pressure and current. The red captions in Figs.4.7-4.8 suggested current densities an order of magnitude smaller for boron-doped diamond relative to gold. However they concerned a variation of cathode material as well as hole diameter. In order to study further the effect of the cathode material, Table 4.1 incorporates data from a more similar geometry, i.e. 200-μm diameter G-u-G. Comparing the latter to the 300-μm diameter B-u-B results, the current density excess in the case of the metal cathode increased to three to four orders of magnitude.

The (semi-)conductivity of the electrodes controls the behaviour of microplasma. Although the above analysis characterized the discharge as a normal glow in the various conditions and reactor types, boron-doped electrodes ensured a more uniform discharge behaviour over the three pressures being considered. Visually, the microplasma on the metal (gold) cathode evolves in Fig. 4.7 from a glowing disc (100 torr) through a gradually completed disc (400 torr) and finally a near filamentary discharge (760 torr). But on diamond, the plasma maintains a glowing appearance of seemingly constant brightness at all pressures. In fact, the only non-circular extra-cavity component at 400 torr is more reminiscent of an off-centred disc than

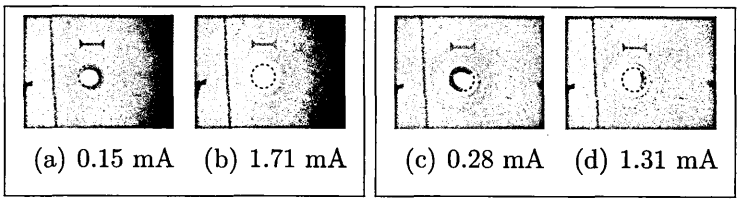

(a) 0.15 mA (b) 1.71 mA (c) 0.28 mA (d) 1.31 mA

Figure 4.9: Radial symmetry of the microplasma present at low pressure (70 torr) helium (a-b) but not at higher pressure (550 torr) (c-d). The 200-μm hole is outlined in red and surmounted by a 200-μm scale.

the moon crescent observed on metal. Electrically, the range of current densities for G-u-G reactors increases sensibly from 100 to 400 and 760 torr. On the other hand, the rise is less evident for semiconducting diamond.

4.3.4 Behaviour with Increasing Pressure

A higher pressure causes a decrease in the collision mean free paths, resulting in smaller microplasma volumes. In Figs.4.7 and 4.8 this appeared as smaller extra-cavity regions for similar currents. This high pressure confinement also leads to a breakdown of the radial symmetry. Indeed at the low hundreds of torr, the micro-discharge appears to take on the cylindrical geometry of the cavity throughout the range of operating current. This is evident for the region on the cathode surface for which the radial symmetry at 100 torr is absent at 400 and 760 torr. For the intra-cavity region, this is more easily observed by looking at the anode side, where the discharge is limited to the interior of the hole. Fig. 4.9 compares the situation for a 200-μm diameter G-u-G reactor operated in helium at two pressures: 70 torr for the left pair and 550 torr for the right pair of images. Some marks on the surface, visible here on the left of the hole, are scratches or similar slight imperfections in the metal film. They were present ever since the devices were delivered and did not influence the operation. Throughout the experiment at 550 torr, the microplasma was radially asymmetric. The orientation could change during operation but without creating a perfect cylinder as for 70 torr.

An increase in pressure also decreased the operating voltage. This results from the multiplication of targets for ionization collisions. It was shown (Chapter 1) that to the right of the Paschen curve minimum — i.e. increasing pressure at fixed electrode separation d — a higher breakdown voltage was required to offset the electron energy lost in more frequent collisions. But once the discharge has been established, these more frequent collisions mean that similar ionization rates can be maintained at higher p with lower voltages. Fig. 4.10 shows data from a G-u-G reactor with diameter $D = 100$ μm. The gap voltage is plotted against current as the applied voltage was increased after ignition. Data sets are coloured according to the operating pressure (see figures' legend). The range of pressures and current plotted are representative of the overall range covered in this research. As pressure increased from 100 to 830 torr, the corresponding curves were shifted to lower operating voltages in both helium and argon microdischarges.

4.3.5 Behaviour with Increasing Current

The microplasma becomes brighter at higher current density. In the previous section this translated into a more diffuse, less bright discharge component on the cathode surface for the lower current density in B-u-B reactors. This is most striking when comparing the gold- and diamond-based expansion at 760 torr; third row of Fig. 4.7 and 4.8, respectively. By way of explanation, higher current requires more ionization collisions, the corollary being more light-emitting recombination and de-excitation events. When it comes to the interior of the cavities, since the cross-sectional area of the microdischarges is similar in all the reactors, identical currents yield identical brightness levels.

With increasing current, the microplasma grows. This does not refer to the cathode-side expansion anymore. In fact it is more clearly observed when looking at the anode side; where any growth is confined to the hole. Fig. 4.11 represents

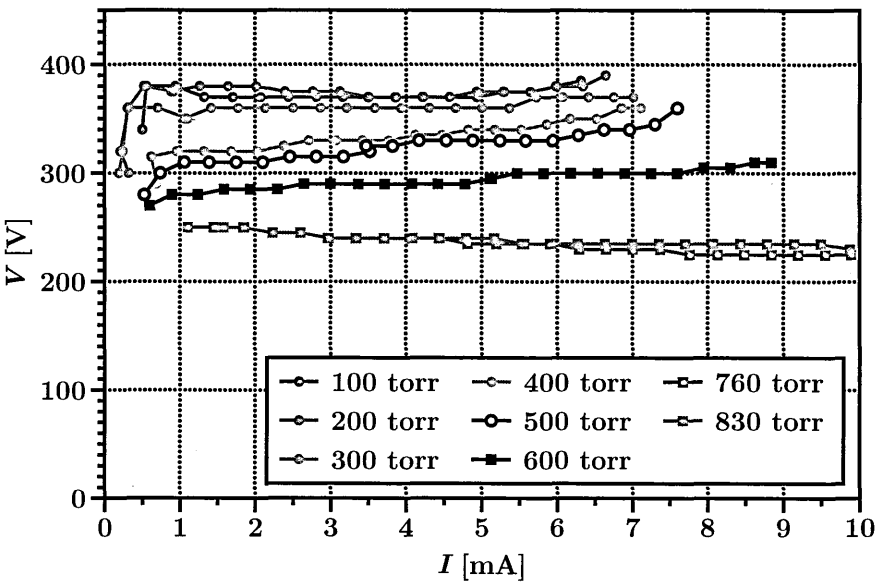

(a) helium microplasma

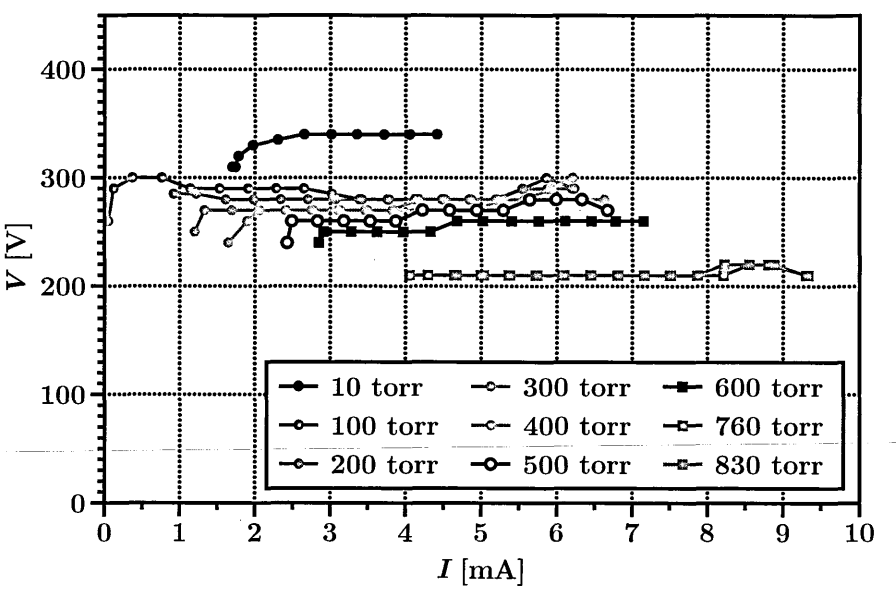

(b) argon microplasma

Figure 4.10: V-I curves for a G-u-G reactor ($D = 100$ μm).

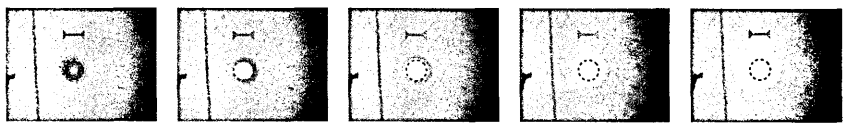

(a) 0.04 mA (b) 0.18 mA (c) 0.36 mA (d) 1.71 mA (e) 3.85 mA

Figure 4.11: As more current is drawn through the microplasma it grows, here inside a 200-μm diameter G-u-G reactor at 100 torr helium; viewed from the anode side. In red, the outline of the hole is surmounted by a 200-μm scale.

Figure 4.12: Schematic set-up for face-on microplasma observation.

photographs of the anode of a 200-μm diameter G-u-G reactor operated in helium at 100 torr; each labelled with the discharge current. As more current is drawn through the hole, the ionization region grows and gradually fills the cylindrical cavity.

4.4 Discussion

The results presented earlier coupled optical imaging of the microplasma with electrical measurements as a means to valuable insight into its operation. Indeed the dependence of (micro-)discharges on current and pressure, characteristic of their operating mode, were best described with these combined diagnostics. When imaging the diamond-based devices, concurrent observation of the microplasma inside the hole and quantification of its extra-cavity expansion were made possible by the set-up presented in the previous chapter and schematically represented in Fig. 4.12. Inside the vacuum chamber, behind a window flange, the hole was magnified and its axis aligned with and centred on the optics.

In the previous section, the first successful operation and characterization of diamond-based microplasma reactors was presented. The optical and electrical re-

sults acquired with G-u-G and B-u-B devices are now compared to similar results reported by other microplasma research teams.

4.4.1 Ignition and Stability of MHCD's

Here the ignition parameters reported earlier are compared to equivalent conditions reported for glow discharges in general and microplasma research in particular.

A first general observation of the Paschen diagrams above shows that microscopic discharges of various configurations share a small $V_b - pd$ region. For point-to-plane gaps — a cathode needle and a plane anode — [Slade and Taylor, 2002] studied the breakdown between electrical contacts in air; confirming the Paschen relationship for $d > 6$ μm. The resulting V_b was between 300 and 400 V for a pd range[10] of $0.5 - 1.5$. [Park et al., 2001] operated blind MHCD devices in the shape of an inverted pyramid, with an opening 50×50 μm^2 and 35 μm deep. The breakdown voltages in neon lied between 200 and 300 V over the range[11] $0.56 < pd < 0.96$ torr cm. [Petrović et al., 2008] studied the breakdown between parallel plates of variable separation. The d value closest to the diamond-based configuration (250 μm) was 100 μm. For the range of pd in common with that research, namely 2 to 5 torr cm, the reported V_b agrees very well with Fig. 4.4(b). Numerous articles have treated the strong departure from theory to the left of the Paschen curve minimum and/or at much smaller d. The aforementioned article is no exception, but since that parametric space is out of reach for the experiments in this thesis, that departure falls out of the scope of this discussion. The ignition parameters of the current diamond-based devices are therefore consistent with other microscopic sources.

The helium curves in Fig. 4.4(a) on page 82 are consistent with other glow discharges. In MHCD's with a blind silicon cathode and open nickel anode, [Schwaederlé et al., 2012] studied the breakdown in helium from 100 to 1000 torr.

[10]Taking 760 torr and $6 < d < 20$ μm from Fig. 3 in the corresponding article.
[11]Taking $700 < p < 1200$ torr and a dielectric spacer with $d \sim 8$ μm.

The electrode separation was a mere 6-μm and the diameter 100-μm, to be compared with, respectively, 250 μm and diameters of 100 or 200 μm for diamond-based metal-dielectric-metal devices in this thesis. The resulting pd region is distinct from that populated in the corresponding diagram above. In their Fig. 7 (a) for the single device case, V_b was more or less constant at $310 - 330$ V at $0.12 < pd < 0.6$ torr cm, increasing to 400 V when going down to $pd \gtrsim 0.06$ torr cm. Two differences with the G-u-G results above are a Paschen curve shifted to < 1 torr cm and a flat gradient in the right-hand branch. Nevertheless, they also reported (their Fig. 13 (a)) a stronger gradient either side of the Paschen minimum in reverse polarity; i.e. with the open cathode and blind anode. The resulting minimum appeared slighly shifted to higher pd, but still lower than with G-u-G devices. An experimental curve was presented in [Lieberman and Lichtenberg, 2005] (their Fig.14.4 (a)) for low pressure parallel plate glow *macro*-discharges. Similarly to the G-u-G results, the Paschen minimum was shifted to higher V_b relative to the theoretical value and the (near-vertical) left-hand branch was confined to $pd > 1$ torr cm.

The case of argon, in Fig. 4.4(b), also agrees with other microplasma results. An overvoltage was suggested, as in the work of [Sismanoglu et al., 2010]. Micro-devices identical to the G-u-G reactors[12] were operated with several electrode materials. V_b was consistently higher than the theoretical values of the black solid line in Fig. 4.4(b). In breakdown studies by [Petrović et al., 2008] with gaps $d < 100$ μm, overvoltage was discarding all but the lowest breakdown voltages. No such filtering of data was applied here, making the fidelity of the Paschen curve for argon G-u-G microplasmas all the more encouraging.

The cathode material is a key factor in the discharge breakdown, especially at microscopic dimensions. Field emission has long been cited to explain the departure

[12]Diameter $D = 200$ μm and inter-electrode spacing $d = 250$ μm.

from the Paschen curve to the left of its minimum [Llewellyn Jones and Morgan, 1951, Boyle and Kisliuk, 1955]; again, out of reach for the current experiments. Recently, [Go et al., 2009] described the use of highly-graphitic polycrystalline diamond to significantly enhance the field emission hence reduce the voltage throughout the *pd* range. However their devices were operated in pre-breakdown mode. Given that diamond has on top of that a high γ coefficient, the V_b values for B-u-B reactors in Fig. 4.5 seem surprisingly high.

A contact resistance between the tantalum foil and the semiconducting B-doped electrode contributes to the aforementioned V_b overestimation. The intrinsic resistivity of the semiconductor film was experimentally determined for a B-u-B device with a four-point probe. The resulting value of 9×10^4 Ω m was then used to determine the extra voltage drop between the edge (location of the tantalum contact) and the centre (location of the cavity) of the device. Assuming constant parameters for the conductive pathway, that voltage was subtracted from the values reported earlier. Fig. 4.13 was adapted with that correction from the helium results of Fig. 4.5(a). The general downward shift brings the curves in the same region as their counterpart reactors with the metal electrodes. This confirms that a contact resistance exists for B-u-B devices and that it can be accounted for. Further parameters could be considered like contact potential of metal on B-doped diamond, spatial distribution of the charge carriers in the CVD thin film around the micro-cavity and their dependence on the operating conditions. But this could form an entire research project and falls outside the scope of the current microplasma characterization. For the remainder of this thesis, the corrected gap voltage can satisfactorily be assumed to have the same meaning for both metal and semiconducting electrodes.

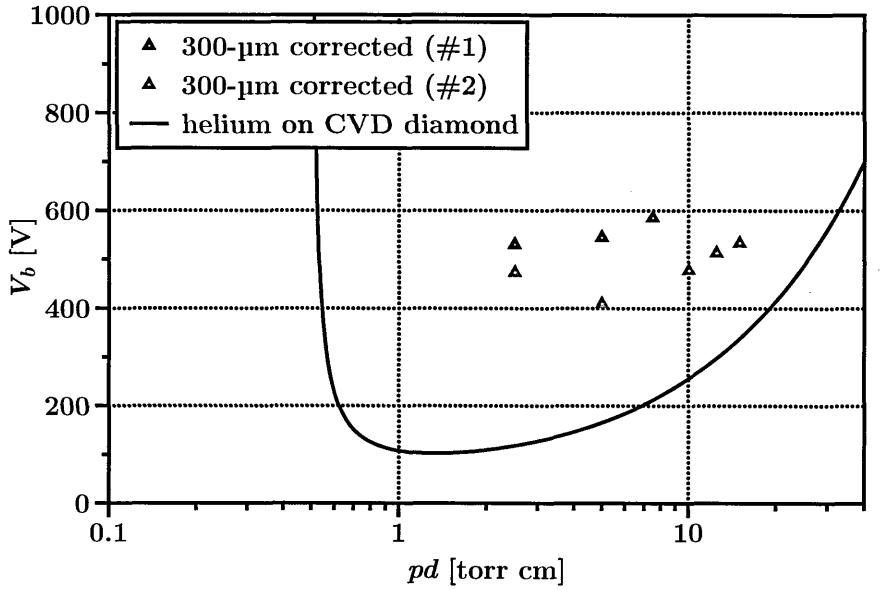

Figure 4.13: Paschen curves for B-u-B reactors in helium, corrected for surface resistance.

4.4.2 Microplasma Modes and Pressure Dependence

The V-I characteristics of similar microdischarges indicate that they usually operate in normal or abnormal glow mode. In the seminal work by [Schoenbach et al., 1996], a 700-μm diameter and 2.1 mm deep blind molybdenum cathode was surmounted by a 250 μm thick mica dielectric and a molybdenum anode. In argon below 16.5 torr, positive differential resistance was maintained throughout the current range. While at 56 torr a negative slope appeared above 30 mA. The positive slope was associated to low current density Townsend mode, which precedes the glow mode. The positive-to-negative discontinuity was linked with the onset of the normal glow mode governed by the hollow cathode effect, i.e. more efficient ionization by pendulum electrons. A similar kink in the V-I was observed in Fig. 4.10.

Later [Schoenbach et al., 1997] argon microplasma was generated with a blind anode surmounted by a 250 μm mica layer and 100 μm cathode with a range of openings: 200, 350 and 700 μm. A similar V-I transition was observed. This was accompanied with discharge expansion on the cathode and followed, at higher

current, with a very faint gradient. K. H. Schoenbach found another interpretation in [Boeuf et al., 2005] for the transition: namely an abormal glow discharge inside the hole turning into a normal glow discharge spreading on the cathode.

Similar experiments were conducted by [Kulsreshath et al., 2012] with 150-μm diameter helium and argon microplasmas at 370 torr inside a blind cavity, 200 μm deep. A hollow silicon substrate and a thin film of nickel were the electrodes, separated by a $\sim$ 6 μm SiO_2 layer. With the blind hollow silicon cathode, the V-I characteristic was positive and the discharge confined to the hole, a clear indication of an abnormal mode. But when using the open nickel electrode as the cathode, the microplasma spilled over it at higher current, maintaining a very slight gradient; both hallmarks of the normal glow mode. These results agree with the coupled optical-electrical measurements in the previous section, in which the onset of a normal glow mode was confirmed by microplasma growth on the cathode surface.

The microdischarge shrinks and loses its radial symmetry at higher pressure. Similarly to the results obtained in G-u-G reactors, [Schoenbach et al., 1997] published photographs of 200-μm diameter argon microdischarges at 56, 250 and 896 torr. As in Fig. 4.9, the circular glow at the lowest pressure took the form of a gradually completing disc with increasing pressure.

The mechanism controlling the spatial distribution of the microplasma inside the hole is the cathode sheath shrinkage. The phenomenon was experimentally studied and modelled by [Lazzaroni et al., 2010] and also in [Kushner, 2005] in argon for metal-dielectric-metal MHCD's. As the collisionality in cathode sheath enhances ionization, the microplasma gets more tightly confined against the electrode. Under microscopic dimensions, rough electrode patches would locally magnify the electric field. This could explain the *selection* of a discharge orientation when the cathode sheath is so close to the metal at higher pressure.

The lower current density in B-u-B devices could be explained by a lower sput-

tering of the diamond electrode. Spectral measurements in [Schoenbach et al., 1996] indicated that the transition to high current mode was accompanied with stronger emission by the cathode metal vapour. Furthermore, it was established by [Gill and Webb, 1977] that the HCD geometry strongly favoured vapour emission. On the other hand diamond is hardly affected by the nearby discharge, either chemically or thermally. This was confirmed in the current research by post-operation visual inspection of the reactors. Without the added contribution of cathode vapour, the microplasma operates at lower current density on semiconducting diamond electrodes. The combined role of diamond *and* semiconductivity is compounded by silicon-based device failures due to excessive cathode material redeposition [Kulsreshath et al., 2012] or too high injected current [Dussart et al., 2010].

4.5 Summary

The research reported above achieved the first successful operation and characterization of diamond-based microdischarges [Mitea et al., 2012]. Two families of devices were designed, fabricated and tested; based on two electrode-dielectric-electrode sandwiches:

- boron doped-undoped-boron doped diamond (labelled B-u-B)
- gold-undoped diamond-gold (G-u-G)

The conclusions reached about the microplasma operating mode were compared with published research results obtained in MHCD's. The same observations could be made based on V-I and optical diagnostics of the discharge. This allowed the description of the effect of various parameters: pressure, current, electrodes' (semi)conductivity and breakdown condition.

Diamond substrates show encouraging potential as a new microplasma technology. Based on reports by other teams as well as comparison with non-diamond practice

devices employed for this work, the data showed good reproducibility. In terms of lifetime, all of the diamond-based reactors are still in good working condition after several hours operation in various experiments. Even beyond one hour continuous operation, no failure has been detected yet. This represents an improvement from the DC silicon-based reported in the literature. It is worth emphasizing that no precaution was taken to alleviate the impact of heat or plasma degradation, such as was customarily reported in the literature: short DC pulses, sub-mA current limitation, gas flow,...

The positive reception of diamond-based research by the microplasma community was the ultimate milestone for this project. It offered a modest answer to the paucity of publications focusing on the role of wall materials that had been highlighted by [Pitchford, 2011]. In particular, the contribution of the current devices is evidenced by the upcoming investigation of the effect of the superlative thermal properties of diamond in Chapter 5 *MICROPLASMA-DIELECTRIC INTERFACE.*

More encouraging still were the numerous comments received by the author following oral and poster presentations at several UK and international plasma physics conferences, lauding the arrival of more reliable devices based on an otherwise elementary construction. It was even suggested that this could pave the way to all-important standardization and better data matching between research teams, owing to the reduced variations over operation time or between identical devices.

Chapter 5

MICROPLASMA-DIELECTRIC INTERFACE

5.1 Introduction

This chapter covers temperature studies of microplasma inside diamond-based reactors. It falls in line with the overarching scope of this thesis to assess this novel microplasma substrate material. A key aim was to better understand the role of the dielectric spacer in a microdischarge. The work reported here is being evaluated for publication.

We observed the evolution of the gas temperature when changing various experimental parameters, with the aim to compare diamond and glass dielectric. The parameters were the input power, gas type, pressure and hole size. We assumed that the microplasma-dielectric interface was a fundamental reactor element for the following reasons. From a design perspective, it serves literally as the central mechanical support for the micro-device. During operation, its relative thickness — typically hundreds of micrometres compared to sub-micrometre electrode thin films — make it the main confining boundary for the plasma.

We intended to correlate temperature with other parameters as well as evaluate the relative influence of the dielectric material. Gas temperature is known to be correlated with plasma properties such as electron density and temperature. We expect that gas temperature would increase with power and this served as the starting point for our research. By changing the other parameters over a set power range, we tested the response of that expected positive gradient. In parallel, we conducted the same experiments with diamond and glass as the dielectric spacer. The goal was to assess to what extent the influence of the dielectric competed with that of other operating parameters.

The structure for this chapter is as follows. In Section 5.2 the motivation for these temperature studies is presented, followed by a description of the reactors used and experimental methods. Experimental results are the subject of Section 5.3, subdivided to reflect the various ranges of operating parameters. These results are then analysed in Section 5.4.

5.2 Research Description

The core of the experiments reported here consisted of remote temperature measurements of the background gas during the operation of a microplasma. The motivation for this type of investigation was triggered by the intrinsic characteristics of the substrate material, as explained below.

In order to put diamond-based results in perspective, an equivalent study was conducted in a material with markedly different thermal properties. These alternative micro-reactors are thus presented later.

Table 5.1: Thermal conductivity, k, of some materials used in microplasma devices (in **bold** for this research). Reproduction of Table 1.1.

Material	k / W m^{-1} K^{-1}	References
Kapton® †	0.12	DuPont [kap, 2006]
Glass	1.38	[Incropera and DeWitt, 1996]
Alumina	36	[Incropera and DeWitt, 1996]
Silicon	148	[Incropera and DeWitt, 1996]
Copper (pure)	401	[Incropera and DeWitt, 1996]
Diamond‡	2050	[Wörner et al., 1996]

Finally, the use of the relevant techniques introduced in Chapter 3 and the collection of data are described under the Methods heading.

5.2.1 Motivation

The thermal properties of diamond opened up the opportunity to study the interaction of heat with the dielectric. Table 5.1[1] compares the thermal conductivity k of diamond with that of common dielectric materials used in microplasma reactors. Our initial assumption was that the highest value of k for diamond could affect the heat balance of the discharge and its surroundings. Therefore a comparison was envisaged of the temperatures obtained with a poor thermal conductor such as glass, with the expectation to detect significant differences over our experimental range. Of interest for this thesis was the resulting assessment of the heat transfer in a microplasma and the role of the dielectric.

The superlative properties of diamond further lent themselves to the characterization of operational advantages such as stability and lifetime. It is clear that the brunt of the plasma-surface interaction would occur at the electrodes in the form of ion/electron-wall collisions in the high-energy environment of the sheaths. Nevertheless, it was thought that the thermal stability of diamond could prove beneficial,

[1]reproduction of Table 1.1 on page 45.

certainly compared to glass. Its chemical inertness and, in the case of all-diamond B-u-B devices, the use of a single solid material were further considered advantageous for mechanical stability. If confirmed, this would translate into more robust reactors exhibiting more reproducibility for diamond than with glass.

5.2.2 Reactors

The first micro-devices studied here belong to either of the families introduced in Chapter 4, namely: G-u-G (gold electrodes and undoped diamond insulator) and B-u-B (same insulator but boron-doped semiconducting electrodes). The hole diameters were 100, 200 and 300 μm. The substrate thickness was 250 μm.

The comparison material, glass, was the substrate in Ta-glass-Ta reactors. An 8-μm tantalum foil was glued by us to a 200 μm thick glass substrate. Similar diameter holes as with diamond were laser-drilled by our partners at the University of Bristol: 100 and 300 but not 200 μm. Besides the much smaller k, the melting point is also lower, at 1883 K [Incropera and DeWitt, 1996].

The relative thickness of the dielectric in the current MHDC design led us to assume that it was a driving site for heat transfer through the reactor. A first reasoning is based on the direction of heat exchange. In the axial direction, heat transfer only occurs in the gas phase, with no interaction with the micro-device, whereas radially, the gas/plasma volume is confined by a solid boundary. For the latter, electrodes are typically an order of magnitude thinner than the dielectric; respectively < 10 μm versus ≥ 200 μm. A second reasoning is related to the major reactions involving gas/plasma particles. The surface interactions — reviewed in Chapter 1, Section 1.2.2 — take place at three interfaces schematically represented in Fig. 5.1. On the one hand, energetic charged particles interact primarily with electrode surfaces — even when the plasma is contained inside the hole — under

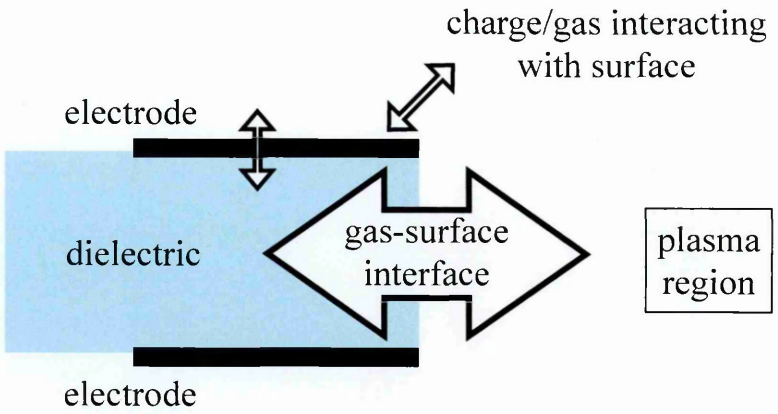

Figure 5.1: Various interfaces for surface reactions. The big double arrow emphasizes the relative importance of dielectric for heat transfer.

the influence of the high potential difference in the anode/cathode sheaths. On the other hand, energetic neutrals interact primarily with the dielectric due to the large surface area presented in the radial direction. As a result, where heat transfer between gas/plasma and the micro-device is concerned, the dielectric is expected to have the major influence; this is symbolized by the bigger double arrow in the figure.

5.2.3 Methods

The equipment and data collection techniques were described earlier in Sections 3.4 *Optical Emission Spectroscopy* and 3.5 *N2SPS Fitting*. Once the discharge was ignited, each subsequent data point of temperature was recorded after the same incremental increase in the applied voltage. The discharge would be kept continuously on until measurements at all the desired voltages were completed. A background image was taken prior to each spectroscopic measurement. This, combined with the handling of the high voltage power supply, resulted in an effective stabilization interval of about 10 seconds at every new input power value prior to the collection of OES data. As explained towards the end of Chapter 3, the uncertainty in the temperature fitting had been computed in a previous research with the same

measuring equipment to be 7%. In addition for measurements of T_{rot} in argon, the presence of N_2 meant that temperature values could only be considered a maximum, i.e. $T_{\text{gas}} \leq T_{\text{rot}}$.

The pressure was continuously monitored inside the vacuum chamber, but not inside the micro-cavity. Therefore the pressure readings reported in the upcoming plots and discussions represent nominal values, irrespective of the gradient arising from the operation of the microplasma. Once a series of measurements was completed at a certain gas pressure, the power supply was turned off and the chamber fully evacuated before filling with gas at the next pressure of interest.

Generally, the same experimental conditions were replicated between diamond- and glass-based devices. However the limited lifetime and lower reliability of the latter resulted in some data plot conditions being differently populated for the two materials. Thus these differences do not reflect any intentional planning.

Where the knowledge of the surface area of a microdischarge outside the reactor hole is reported, it was obtained via optical imaging, as explained in Section 3.3. The corresponding data was obtained by replicating the pressure and power conditions for the temperature experiments.

5.3 Results

The forthcoming results report the gas temperatures measured when varying three sets of parameters. First the microplasma was ignited in either helium or argon, at a range of pressures. Next came a variation in the microplasma dimensions; the reactor size and the microplasma volume (current-controlled). The third relationship links the gas temperature to the dielectric material. The structure of this section

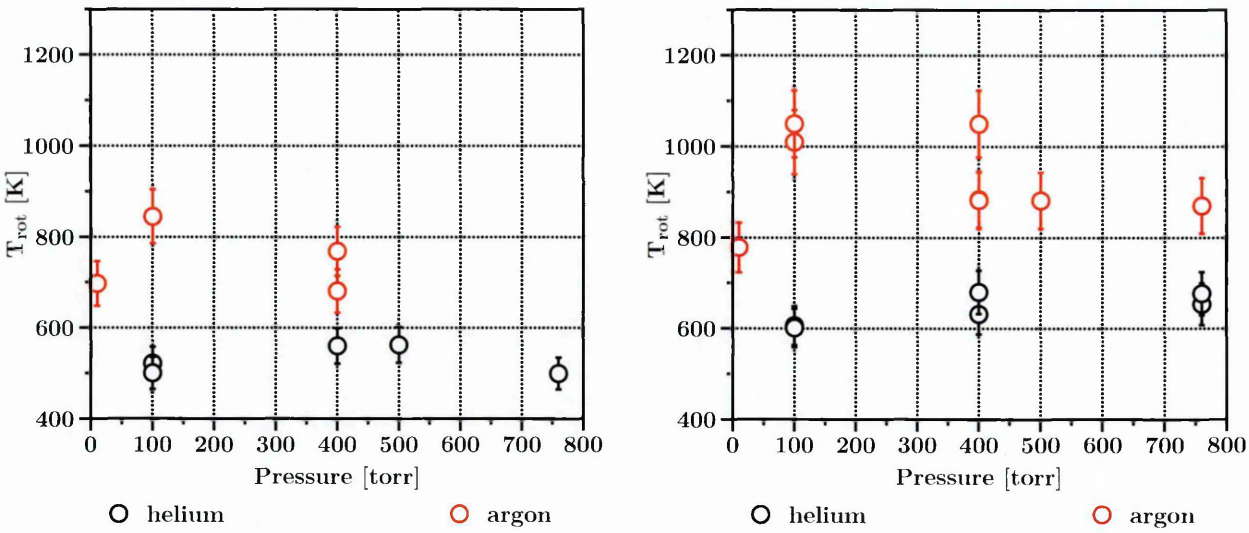

(a) 0.5 ± 0.1 W

(b) 1.5 ± 0.1 W

Figure 5.2: Gas temperature against pressure in **helium** (black open circles) and **argon** (red open circles) inside a 100-μm diameter G-u-G reactor.

adopts the same parametric division.

5.3.1 Temperature against Input Power

Before presenting results of the parametric study, the dependence of gas temperature on input power is demonstrated. For any electric discharge, the power to heat conversion is driven by the numerous collisions between the charged particles, accelerated by the plasma field, and the neutral atoms.

In order to visualize the thermal effect of power, plots of temperature results at two power levels are shown in Fig. 5.2. The y-axis shows the rotational temperature (in Kelvin) of the N_2 second positive system — indicative of the background gas temperature — and the x-axis the pressure (in Torr).

It can be seen from the figure that the gas temperature increases with power. Between Fig. 5.2(a) at 0.5 W and Fig. 5.2(b) at 1.5 W, helium heats up by about

100 K. For the same power difference argon sees its temperature rise by 100 to 200 K.

The direct response of the background gas temperature to electrical input power is the common thread throughout this Results section. Indeed, differences in this proportionality are useful sources of information about the influence of other parameters. In particular, the upcoming sections address the effect of such parameters as: the gas type and pressure, the reactor diameter, the dielectric material. These will best be expressed via temperature–power plots.

5.3.2 Temperature against Gas Type and Pressure

Microdischarges in argon cause the neutral gas to get hotter than in helium. As can be observed in Fig. 5.2, helium data points remain closer to the ambient temperature value at 0.5 W. At higher power, argon heats up significantly more, with its red markers departing even more from the helium ones at 1.5 W. The argon data generally seems more spread out than that for helium, as expected from the inherent uncertainty in temperature measurements in N_2-argon mixtures[2].

The temperature responds directly to a change in the background pressure, as displayed in Fig. 5.3. Covering the same range of nominal pressures as in the previous figure, helium is singled out here, because of the richer data enabling more parametric combinations. In diagrams (a) to (d), data for three reactor diameters (100, 200 and 300 μm) are overlaid. Only a subset of the same data was represented in Fig. 5.2.

For a given input power, the gas temperature response varies non-linearly with pressure. Data for 400–500 torr seems to suggest slightly higher temperatures than at lower pressures. It is the most evident at 0.5 W (Fig. 5.3(a)) and 100 μm: T_{rot},

[2]see Section 2.2.3; N_2 was 0.5% by volume throughout this research

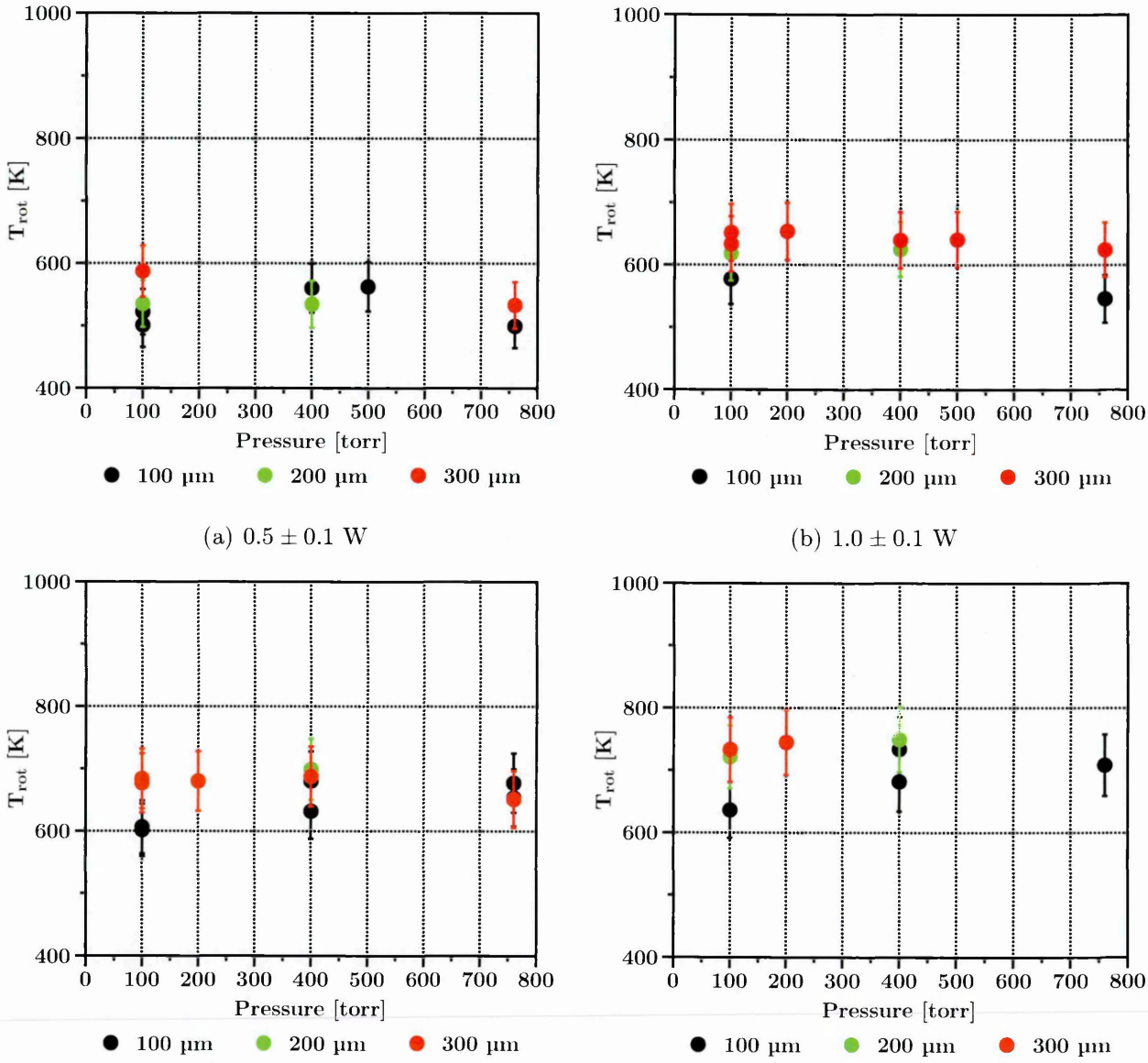

(a) 0.5 ± 0.1 W

(b) 1.0 ± 0.1 W

(c) 1.5 ± 0.1 W

(d) 2.0 ± 0.1 W

Figure 5.3: Gas temperature against **helium** pressure at four input powers: (a) 0.5 to (d) 2.0 W. Data for three reactor diameters are overlaid: 100-μm G-u-G (black), 200-μm G-u-G (green) and 300-μm (red) B-u-B.

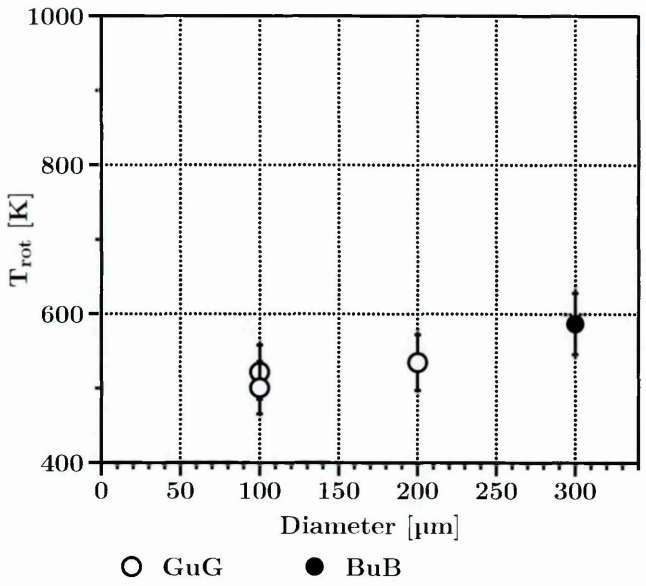

Figure 5.4: Gas temperature versus reactor diameter in 100 torr **helium** and an input power of 0.5 W. Two families of micro-devices are differentiated: G-u-G (100 or 200 μm) as open circles and B-u-B (300 μm) as a closed circle.

rising about 50 K between 100 and 400 torr. In this case, the same decrease is observed from 500 to 760 torr. More generally, temperature seems to level off at the highest pressure rather than continue to increase from the lower pressures. This is an important result that will be discussed in Section 5.4.

5.3.3 Temperature against Microplasma Dimensions

The three available reactor diameters — 100, 200 and 300 μm — responded differently to the pressure increase discussed previously: see Fig. 5.3. Only for 100 μm does the curve seem to go to a maximum at medium pressures. The 300-μm reactors seem to maintain the temperature across the pressure range, being slightly cooler at 760 torr. The lack of temperature values for 200 μm precludes any extensive comparison.

The maximum temperature appears to be affected by the reactor diameter. For 100 torr helium at 0.5 W, this is depicted in Fig. 5.4. The higher the diameter, the

hotter the gas. Between 100 and 300 μm, the difference is about 100 K. It can also be seen in Fig. 5.3, although less distinctly at higher pressures. As for the diameter of 200 μm, the temperature is undistinguishable from 300 μm.

In Fig. 5.5 the temperature–power relationship can also be seen to be sensitive to the reactor diameter. First, at 100 torr helium (Fig. 5.5(a)), the temperature is consistently higher when the diameter is 300 μm than in 100 μm. The latter seem to be indistiguishable from the values for 200 μm. This trend continues through the power range 100 mW $< P \lesssim$ 2500 mW.

Secondly, at pressures between 400 and 500 torr, the differences between various reactor diameters becomes insignificant over the entire power range (Fig. 5.5(b)).

Finally, at atmospheric pressure (760 torr) the temperature ranges for 100 and 300 μm (with no data available for 200 μm) overlap completely (Fig. 5.5(c)).

5.3.4 Diamond vs. Glass Dielectric

This section aims to identify differences due the dielectric material, by replicating the above studies in glass substrates instead of diamond. The electrode-dielectric-electrode sandwich is now tantalum-glass-tantalum, referred to as Ta-glass-Ta devices. As earlier, temperature–power dependence is first observed in argon and helium. Next, the effect of gas type, pressure and microplasma dimensions are studied. The intrinsic reliability of all types of micro-reactors in this research will be the topic of the following subsection.

It can be seen in Fig. 5.6 that the gas temperature increases with power. Results for 300 μm diameter are plotted for a power of 0.5 W and 1.0 W. The paucity of corresponding data, in particular in argon, is the reason for not choosing 1.5 W here, as opposed to previously. As it happens, this was a direct consequence of the limited durability of the glass substrate. From now on, square markers are used to

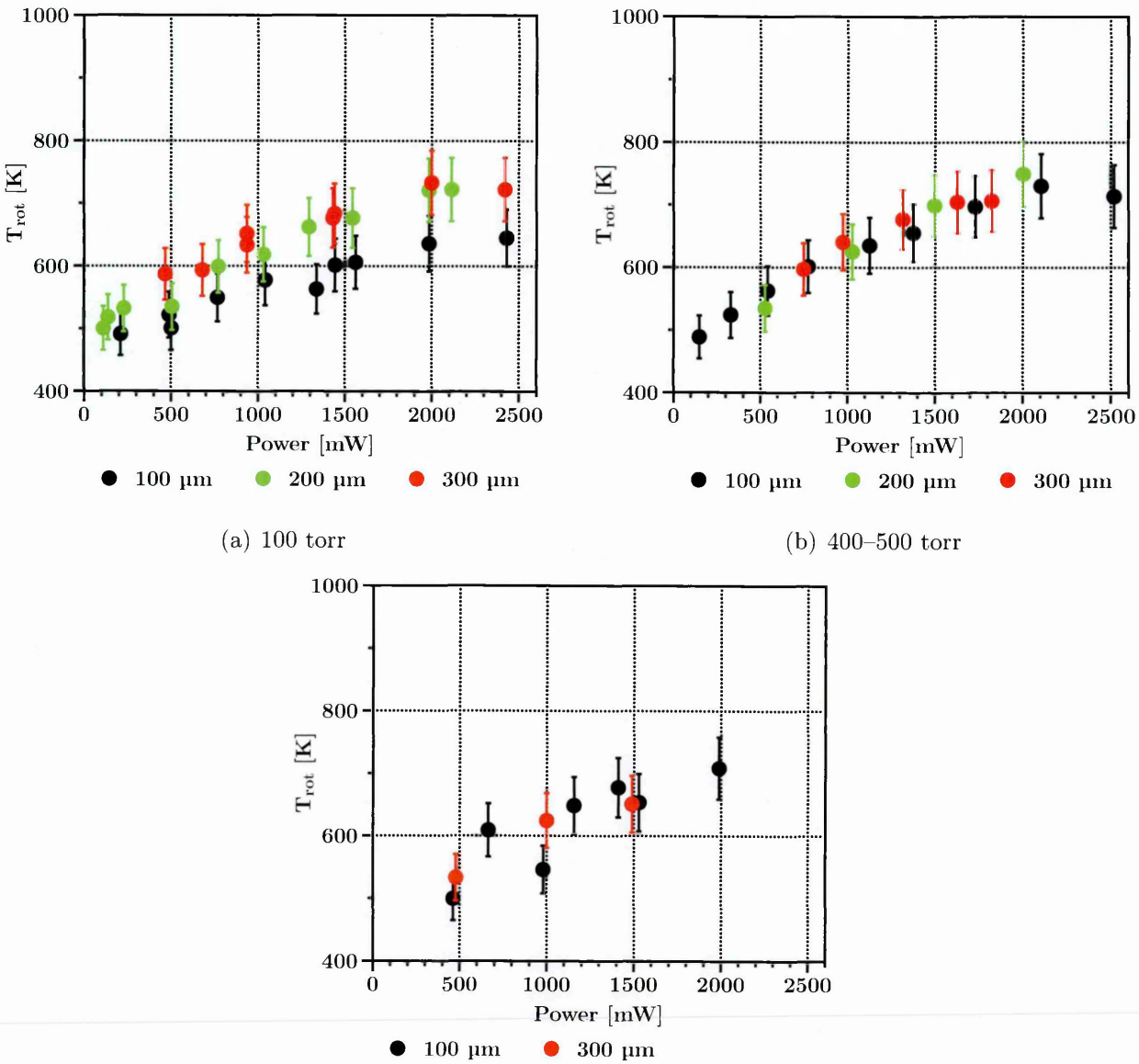

(a) 100 torr

(b) 400–500 torr

(c) 760 torr

Figure 5.5: Temperature–power relationship for three reactor diameters: 100-μm G-u-G (black), 200-μm G-u-G (green) and 300-μm (red) B-u-B. The **helium** pressures studied are: (a) 100, (b) 400–500 and (c) 760 torr.

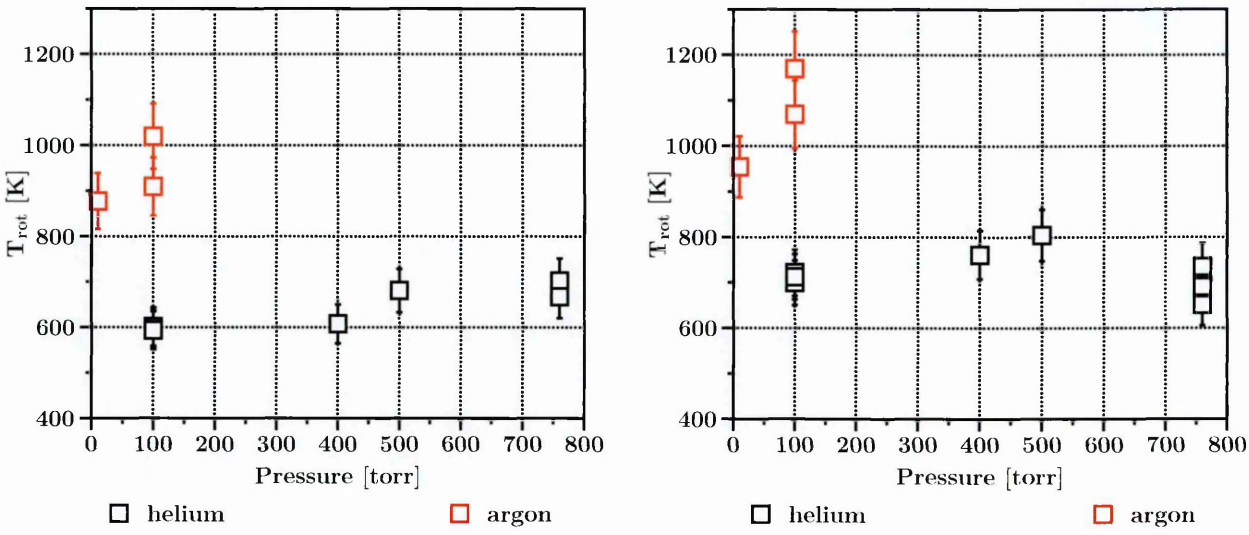

(a) 0.5 ± 0.1 W

(b) 1.0 ± 0.1 W

Figure 5.6: Gas temperature against pressure in **helium** (black open squares) and **argon** (red open squares) inside 300-μm diameter Ta-glass-Ta reactors.

differentiate from diamond-based results. For both argon and helium, the difference due to a rise from 0.5 to 1.0 W is between 100 and 200 K. This represents a rise of around 200 K for argon and 100 K for helium compared to diamond. Although for the latter the diameter was 100 μm versus 300 reported here. Nevertheless, trebling the size of the diamond reactors did not lead to such temperature changes.

A microplasma in argon is hotter than its helium counterpart, as can be seen in Fig. 5.6. For want of results at higher pressure, argon data is limited to ≤ 100 torr. Temperature values are about 300 K higher in argon than in helium at 100 torr. As indicated above, this is thus significantly more than when diamond is the dielectric.

With glass as the dielectric substrate, Fig. 5.7 shows that the gas temperature responds differently to pressure than in diamond. For helium microplasma inside the two available diameters — 100 and 300 μm — temperature data is plotted against pressure at 0.5 and 1.0 W input power. The limitation in the power range, compared

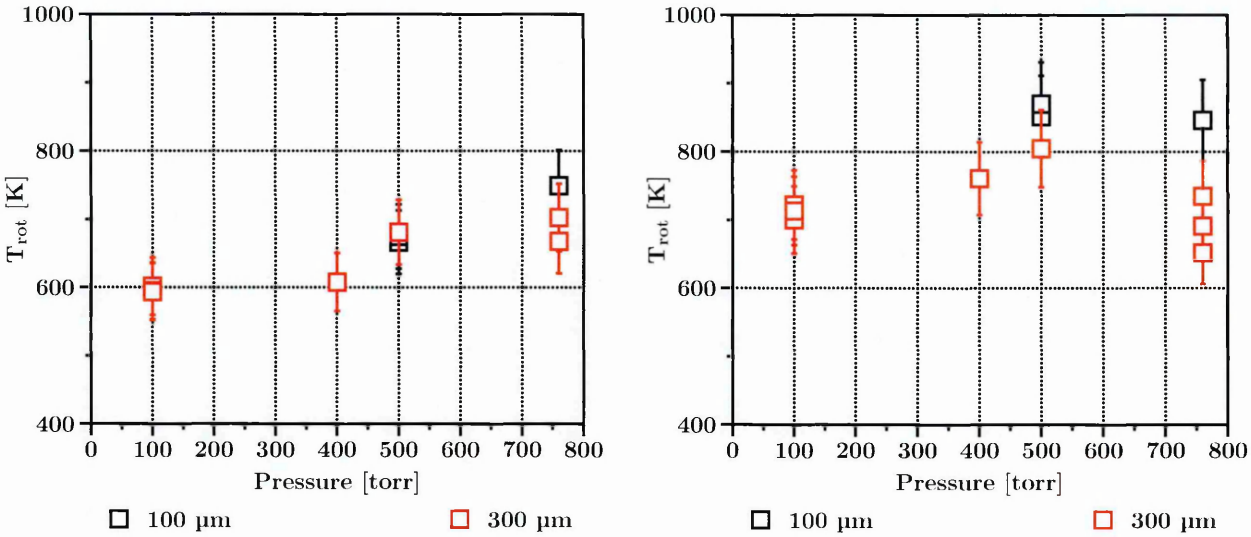

(a) 0.5 ± 0.1 W

(b) 1.0 ± 0.1 W

Figure 5.7: Gas temperature against **helium** pressure at two input powers: (a) 0.5 and (b) 1.0 W. Data for two diameters are overlaid: 100 μm and 300 μm Ta-glass-Ta.

to the graph for diamond (Fig. 5.3) follows from the fact that the glass-based devices could not sustain operation up to the same electrical input power.

The differences with the diamond results are detected at every operating pressure. For 100 μm at 0.5 W, the temperature does not show signs of levelling off at higher pressures. With 300-μm reactors, temperature increases steadily with pressure at 0.5 W. And at 1 W the temperature seems to peak at medium pressure. In diamond, the latter was observed in the smaller diameter *and* the lower power value. In this limited pressure range, temperature data is higher with 100 than with 300 μm.

Fig. 5.8 shows that the influence of diameter on temperature is also different in glass-based reactors with respect to diamond. No data is available for 200-μm and, in general, less data could be obtained with Ta-glass-Ta devices due to their inferior durability. First, at 100 torr, only the larger diameter could be studied. Secondly, for pressure between 400 and 500 torr, the 100-μm reactor led to slightly higher temperatures. Finally, even at atmospheric pressure does the smaller diameter sustain

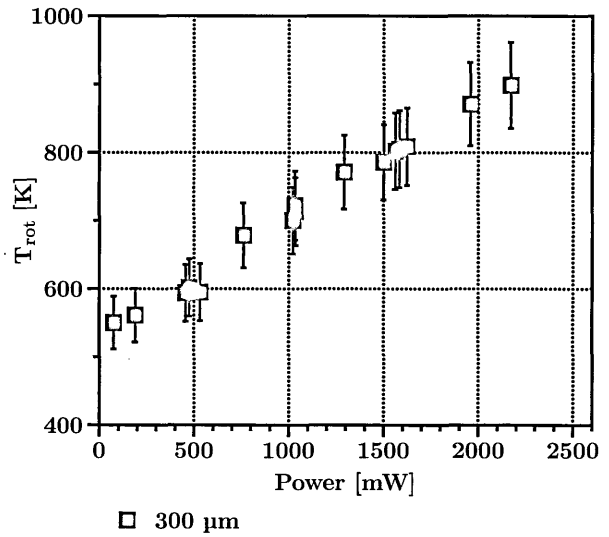

(a) 100 torr

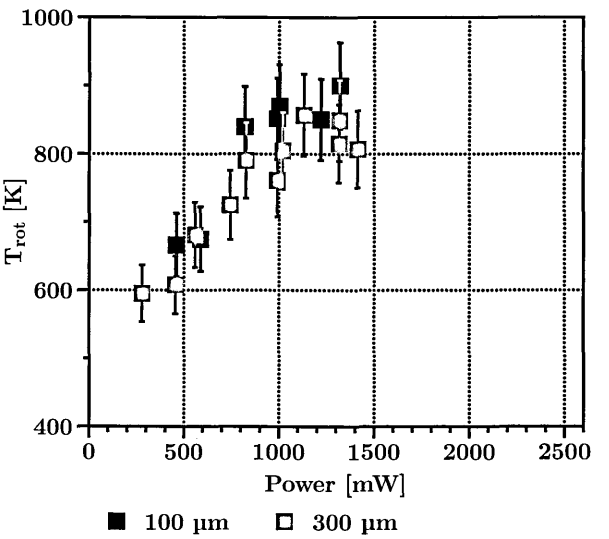

(b) 400–500 torr

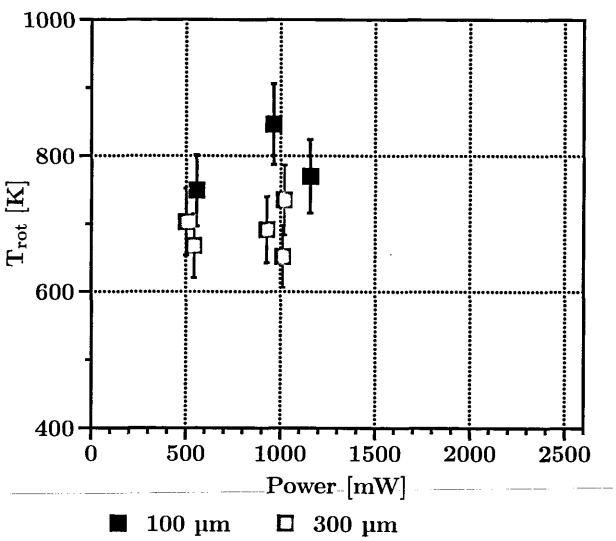

(c) 760 torr

Figure 5.8: Temperature–power relationship for three reactor diameters: 100 μm (black) and 300 μm (red) Ta-glass-Ta. The **helium** pressures studied are: (a) 100, (b) 400–500 and (c) 760 torr.

higher temperatures. In diamond, the difference was hardly noticeable for either condition. Also noteworthy is the steeper gradient of Fig. 5.8(a). All the latest diagrams show this stronger response of gas temperature to input power compared with diamond.

The reasons for these temperature effects are discussed in Section 5.4. The next section compares results from different devices with the aim of understanding device lifetime.

5.3.5 Reproducibility & Lifetime of Micro-Reactors

Issues of reproducibility and lifetime of microplasma reactors are regularly reported in and between research groups, though conspicuously rare in the literature. Their reliability, hence that of the collected data, cropped up regularly in our lab meetings as well as at every conference that the current author attended. What follows is an introduction to issues with and the potential of the diamond-based micro-devices. They seem promising for future research or technology owing to their reproducibility and the lifetime of our first generation of devices. The data presented here was not specifically collected with the intention of a reproducibility study. Had time and resources permitted, a bespoke lifetime experiment would have been set up. The corollary is that the few available results represent a picture of the durability of the reactors in *actual* operating conditions.

The operating range and duration of each experiment was chosen freely by the author for diamond but constrained by the stability and lifetime of the glass-based devices. This is reflected in the number of corresponding data points. Table 5.2 provides an exhaustive list of the operating times for all the micro-reactors employed for this thesis. The left-hand half reports the cumulative operation time of diamond-based reactors. The differences are merely due to the availability of

Table 5.2: Operating times of the devices († = lifetime, for failed ones) used in this thesis. E-D-E refers to the electrode-dielectric-electrode sandwich.

E-D-E — DIAMOND-BASED	**Time**	**E-D-E** — NON-DIAMOND	**Time**
G-u-G (code S1)	14 h 55'	Ta-glass-Ta (code 1) †	1 h 30'
G-u-G (code S2)	2 h 15'	Ta-glass-Ta (code 2) †	4 h 15'
G-u-G (code S3)	6 h	Ta-glass-Ta (code 3) †	0 h 45'
G-u-G (code 100)	23 h 15'	Ta-glass-Ta (code 100) †	55'
B-u-B (code S51)	4 h 35'		
B-u-B (code S85)	1 h 30'		
B-u-B (code array)	1 h 45'		

the corresponding devices for the experiments at hand. On the other hand, the times reported in the right half of the table are the maximum period before glass-based reactors started to fail. They would unexpectedly extinguish the microplasma while operating. Moreover they showed signs of short-circuits when subsequently attempting to set them up and operate them again.

Same device

Data reproducibility *with the same device* was studied by looking at the variation of the V-I characteristics over operating times. For each of the three families of micro-devices, results are presented in Fig. 5.9 for a similar working condition. Data was obtained with a single device from those categories: (a) 100-μm G-u-G, (b) 200-μm G-u-G, (c) 300-μm B-u-B and (c) 300-μm Ta-glass-Ta reactors. Only one 100-μm Ta-glass-Ta reactor existed and it could not be operated in more than one experiment. Each subfigure was traced from data of one and the same micro-device for consistency. The gas was helium at a pressure of 100 torr. As already pointed out, obtaining comparable data was not facilitated by the variability of operating conditions and times. The latter were the result of an arbitrary experimental programme, and lifetime issues for glass-based reactors. The *total operating times* give the cumulative hours over several days of weeks. The gaps can be explained by the fact that some of this time was used to test the experimental set-up, perform

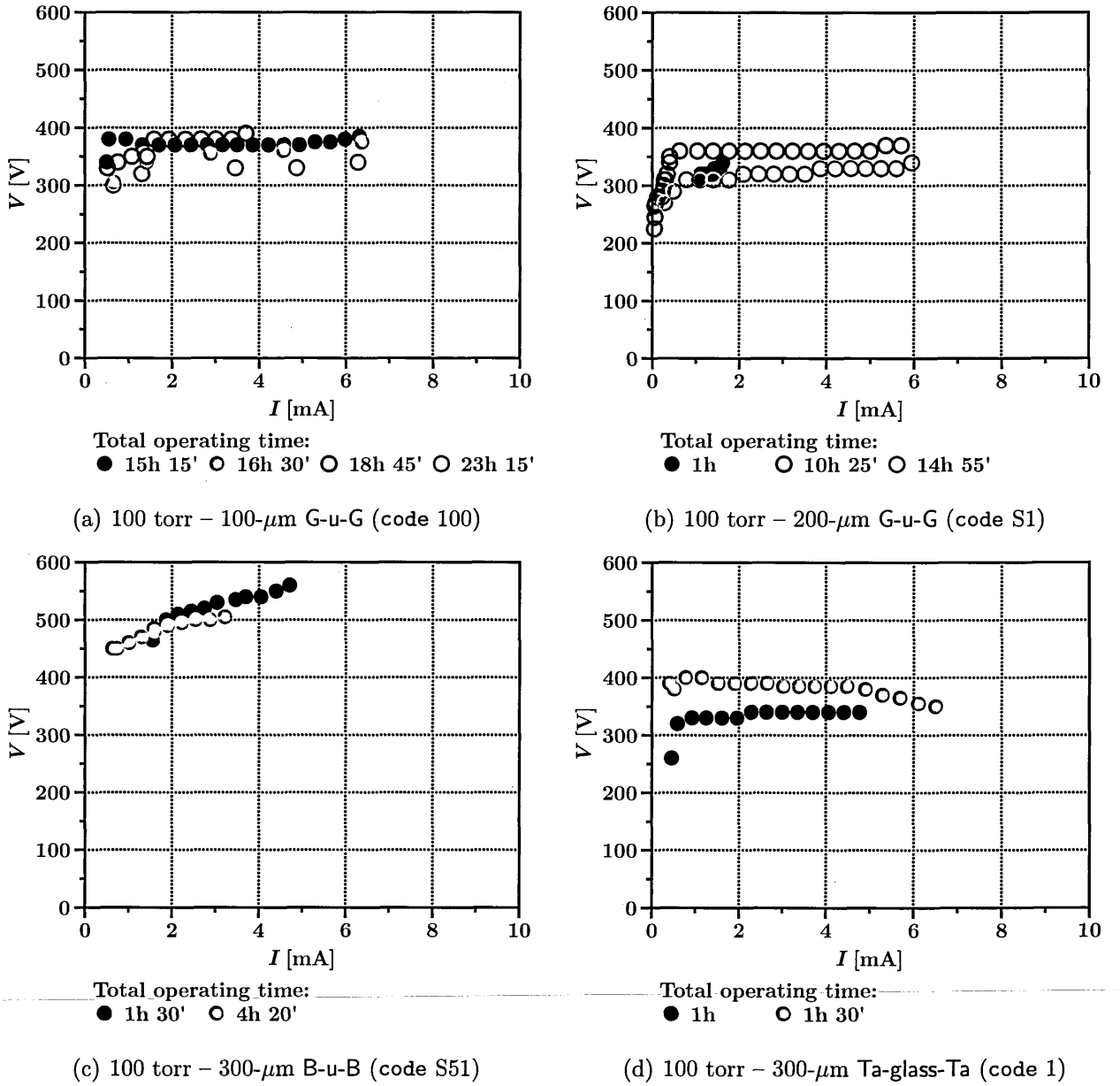

(a) 100 torr – 100-μm G-u-G (code 100)

(b) 100 torr – 200-μm G-u-G (code S1)

(c) 100 torr – 300-μm B-u-B (code S51)

(d) 100 torr – 300-μm Ta-glass-Ta (code 1)

Figure 5.9: V-I variation (for the same reactor) over time for 100-torr helium microplasmas. After the pressure value underneath each diagram, the specification describes the reactor diameter and type, as well as an internal reference code. Different data symbols are used to differentiate between the total operating times.

non-V-I measurements or ignite microdischarges in different gas and/or pressures.

A general trend of Fig. 5.9 is that the V-I curves maintain their shape within a graph but differ between graphs, i.e. between the type of micro-reactor. The G-u-G traces in each of Figs. 5.9 (a) and (b) have the same profile but they are spread apart over a range of $>$ 50 V. The results were collected over 8 hours (100-μm G-u-G in 5.9(a)) and 14 hours (200-μm G-u-G in 5.9(b)). For the all-diamond reactor S51 the voltage variation is less than 50 V (5.9(c)) over a time span of 3 hours. Data for glass-based device Ta-glass-Ta 1 are also separated by about $>$ 50 V for the glass-based device. Although, remarkably for the latter, this occurred over as short a period as 30 minutes. Equally noteworthy is the fact that the glass-based device became inoperable at the end of these experiments, contrary to all of the diamond-based reactors.

Between identical devices

Data reproducibility *between identical devices* could be conducted in each of the device families under the same conditions as above: 100 torr helium. Table 5.2 lists the three groups of identical reactors, which are:

- G-u-G reactors S1, S2 and S3
- B-u-B reactors S51 and S85, although they are more appropriately considered *similar* than *identical* since the fabrication was significantly upgraded between the two
- Ta-glass-Ta reactors 1, 2 and 3

Only one 100-μm G-u-G existed, explaining that one fewer diagram is provided in Fig. 5.10 on page 120.

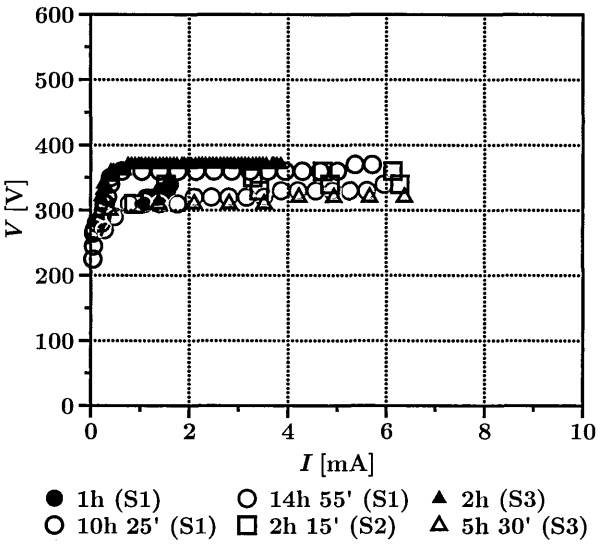

(a) 100 torr – 200-μm G-u-G (code x)

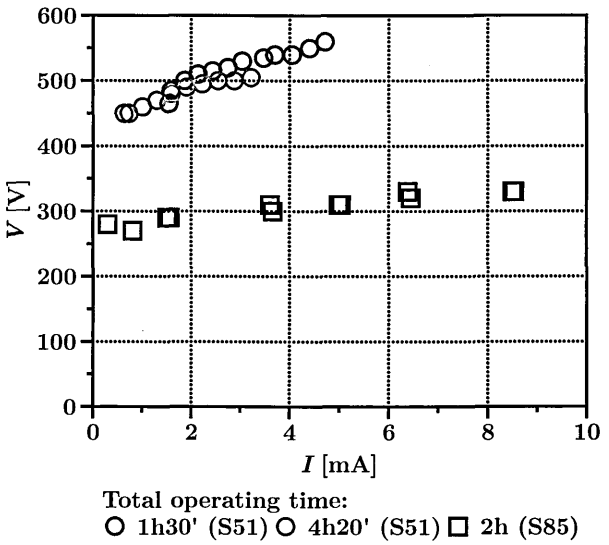

(b) 100 torr – 300-μm B-u-B (code x)

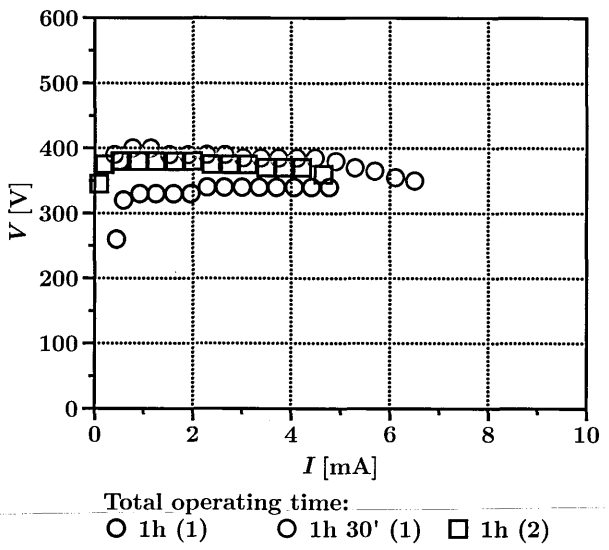

(c) 100 torr – 300-μm Ta-glass-Ta (code x)

Figure 5.10: V-I variation (comparing identical reactors) over time for 100-torr helium microplasmas. The pressure, reactor diameter and type are written underneath each diagram. Different data symbols are used to differentiate between the total operating times.

The most striking feature is the discrepancy between the V-I characteristics of the two B-u-B micro-devices (5.10(b)). S51 was operated at nearly double the voltage necessary to sustain a microplasma inside S85. Apart from that, they both gave rise to a slightly positive gradient throughout the operating range.

All three G-u-G micro-devices operated in the same current and voltage range, with no more differences between devices than there is for a single device (see corresponding Fig. 5.9(b)).

Glass-based devices similarly occupy together the same region of their graph (Fig. 5.10(c)). As before, the main difference resides in the short time span over which the measurements were and could be performed. According to Table 5.2, device number two was actually operated subsequently, but not in 100 torr helium. Nevertheless, the ultimate outcome was a failure of all glass-based devices and no diamond-based ones.

5.4 Discussion

The results above are now analysed in the light of the microplasma-dielectric interface for steady-state glow microdischarges. For the gas phase, the temperature dependence on the gas type and pressure is discussed. This is followed, considering the solid dielectric, by the influence of its dimensions and substrate material. In fact, the latter affects the lifetime of the micro-reactors, hence the time-span and reproducibility of the data collection. This will be the concluding topic of this section. But first, the basic relationship between gas temperature and input power is demonstrated.

5.4.1 Temperature–Power Relationship

The results shown earlier indicate that the gas temperature rises with input power. This dependence is plotted in Fig. 5.2 p. 107 for a diamond-based reactor and in Fig. 5.6 p. 113 for glass.

The basis for gas heating in an electric discharge was given in Eqs.1.16–1.18 [Fridman and Kennedy, 2004]. In so-called Joule heating, n_e/m^3 electrons are accelerated into collisions with neutral molecules at a rate of $\nu_{\mathrm{el}}/\mathrm{s}$ by the electric field E at a volume rate of:

$$\frac{n_e e^2 E^2}{m_e \nu_{\mathrm{el}}} = n_g c_p (T - T_0) \nu_T \tag{5.1}$$

with the equality corresponding to the steady state. The brackets contain the rise in temperature from the ambient value. It depends on the specific heat c_p, the density of neutral targets n_g/m^3 and the rate of heat transfer ν_T. The latter is made up of contributions from conduction and convection.

The above two figures confirm gas heating as the input power rises from 0.5 to 1.5 W or 1.0 W. Qualitatively, this is the case irrespective of the gas type or pressure in the vacuum chamber. This temperature–power relationship is analysed in the context of various parametric studies.

5.4.2 Effect of Gas-Phase Phenomena

There is a clear dependence of the temperature on the type of background gas. For a given power, argon consistently produces higher temperatures than helium. Fig. 5.2 for diamond and Fig. 5.6 for glass agree.

This can be explained by helium's higher thermal conductivity. The coefficient

of conduction, k, is a component of ν_T in Eq. 5.1. The respective values are 0.0177 W m^{-1} K^{-1} for argon and 0.1513 W m^{-1} K^{-1} for helium. Their specific heats are $c_{\mathrm{He}} = 5193.1$ J kg^{-1} K^{-1} and $c_{\mathrm{Ar}} = 520.33$ J kg^{-1} K^{-1}. With comparable densities (electrons and neutrals), electric fields and electron-neutral collision rates, those higher values for helium impose a smaller rise $T - T_0$ than in argon. Thermal conductivity of the wall material is expected to become important the more the microdischarge is confined inside the hole, i.e. when not spilling over the cathode.

If pressure was the driving factor controlling the temperature, the latter would steadily increase between 100 and 760 torr; in contradiction to the earlier diamond-based results. As *nominal* pressure (i.e. momentarily disregarding local gas rarefaction during operation) increases, so does the density of target neutrals for the heat inducing collisions by charged particles. As an estimate, from Section 1.2, the rate of momentum transfer collisions ranges from 0.4 GHz at 100 torr to 3 GHz at atmospheric pressure. The higher mobility of electrons in the bulk of the plasma — broadly speaking, inside the hole — ensures that Joule heating is driven by them, as expressed in the above formula from [Fridman and Kennedy, 2004]. However near the cathode — at and beyond the rim of the micro-cavity — thermalization of the background gas originates in collisions with ions [Revel et al., 2000]. Accelerated in the sheath, the latter transfer energy to *fast neutrals*, which subsequently distribute it in their population. This transfer increases with charge density, which itself increases with pressure, as modelled for argon microdischarges with the same MHCD geometry in [Kushner, 2005]. Whatever the heating mechanism, pressure limited results would therefore have a constant temperature–pressure gradient. This picture was offered by Kushner *et al.* and confirmed by experimental measurements in argon microplasmas from 40 to 300 torr [Penache et al., 2002]. Unfortunately the most apparent departure from this trend in the current thesis only occurs closer to atmospheric pressure. Another key difference with the work by Penache *et al.*

was their limitation to a low input power: constant current of 0.5 mA and 200 V sustaining voltage. Over the operating range of interest here, results cannot be said to be pressure limited.

The microplasma excursion out of its hole is an important factor controlling the background gas temperature. Varying power helps interpret the departure of our results from the pressure limited case. In the mode of operation of the diamond-based reactors, as reported in Chapter 4, as the input power increases the microplasma expands; initially out of the hole then onto the cathode surface. One direct consequence is the increased surface area for heat transfer. For a 200-μm diameter MHCD, convective axial heat flow up to 23.6 m s^{-1} was computed in 250 torr argon at 2 mA [Kushner, 2005]. The peak was inside the hole and speed dropped off to < 5 m s^{-1} over less than 100 μm from the cathode rim. Convection is thus significant along the axis between the electrodes. Conduction will also play a role, mainly over the off-axis outer microplasma volume. These mechanisms compete with the temperature rise due to higher pressure/density, thus putting a cap on the gradient of Fig. 5.3.

The thermodynamical (above) over collisional (*pressure limited*) control is favoured by the diamond dielectric. In [Kushner, 2005] they compared the aforementioned situation with the case of two stacked MHCD's. The anode of one was further separated from the cathode of the other by a dielectric. Of interest to the current discussion is the slower convective flow (new maximum of 20 m s^{-1}) and a marginal decrease in the maximum temperature (577 K from 581 K); both resulting from better heat transfer through the solid walls. A first noticeable difference in their double-MHCD geometry was that the flow around one cathode was fed into the other down the flow. A second difference is in the thicknesses of the reactor layers: 100 μm for the electrodes and 200 μm for the dielectric. Diamond dielectric in the current micro-reactors provide excellent thermal conduction — without the extra

MHCD in the above simulation — with the added favourable relative thickness: < 5 μm for the electrodes and 250 μm for the dielectric.

When heat transfer by convection-conduction through solid and gas is hindered, the temperature is more sensitive to pressure changes. Comparing the corresponding results with diamond (5.3 (a-b)) and glass (5.7 (a-b)), the temperature-pressure gradient is somewhat increased in the latter. Moreover the glass-based data pointed to hotter gas inside the smaller diameter, i.e. the converse of the diamond situation. This also agrees with the temperature being controlled mainly by gas-phase (pressure) phenomena for a poor thermal conducting dielectric.

5.4.3 Effect of Reactor Dimensions and Material

Differences between the results with various reactor diameters are now examined. So far the discussion was based on 0.5 and 1.0 W of input power. This section highlights an interesting diameter-dependent response at higher powers, with the aim to link it to key microplasma phenomena. Where available, this analysis will make use of results obtained with both dielectric materials.

With increasing input power, thermodynamical temperature control gives way to collisional control; in priority in the smaller reactors. It was explained previously that the temperature was mediated by convection-conduction in the solid and gas phases provided that the system presented a high enough heat transfer coefficient. At 0.5 and 1.0 W, it translated into somewhat flat temperature-pressure gradients for all the diamond devices. Whereas the gradients were slightly positive for glass-based reactors. Concentrating on 1.5 and 2.0 W — data only available for diamond — in Fig. 5.3, the slope for 100 μm becomes slightly positive. But the same cannot be said for 300 μm. This is consistent with the earlier view that, as the intrinsic heat transfer capability of the microplasma-reactor system is overwhelmed by input

power, the temperature returns to a pressure limited situation. This happened at low power for glass, i.e. 0.5 and 1.0 W. And now it happens for the smaller diameter but not (yet) for the larger ones, since the power density is higher in the former.

The surface to volume ratio of microdischarges accentuates the effect of the wall material. Indeed, when the microplasma is more confined, the temperature is more material-dependent. Figs.5.5 and 5.8 compare the response of temperature to diameter. At 100 torr only diamond data is available and shows a sensibly lower temperature range for 100 μm. Remaining with diamond, at medium then atmospheric pressre the smallest diameter shows an upward shift in temperatures that is hardly detected for the larger diameters. On the other hand with glass as the dielectric, the temperatures are generally higher (for both 400–500 and 760 torr), with the smallest diameter showing the more pronounced difference with equivalent diamond results.

5.4.4 Wall Materials and Microplasma Stability

Besides their influence on the microplasma behaviour discussed previously, the wall materials are determinant for the operation itself. The interest of this thesis lies with characterizing the reproducibility of the experimental data as well as the lifetime of the micro-reactors. Singling out diamond as a high durability material addresses a dual interest of our research consortium and the current author:

- establish the useful potential of CVD diamond as microplasma material
- pave the way for more sustained Science and Enterprise innovations based on microplasma research.

Microdischarges, though *non-thermal*, pose a substantial thermal threat to their confining reactors; less so to diamond-based ones. As seen from Table 5.2 p.117, Ta-glass-Ta reactors all suffered failures that G-u-G and B-u-B did not. Also, their

operating times were comparable, even shorter than some diamond reactors. Neither were glass-based devices operated at significantly higher temperatures. In general, they were shown to yield higher temperatures and the bulk of the results and discussion covered helium microplasma. However the diamond devices were operated, in argon, at temperatures comparable to the ones attained with Ta-glass-Ta devices; see Fig. 5.2 (p.107). The thermal properties of diamond never got caught out throughout the experimental conditions.

The thermal load of microplasma operation is a lifetime limiting factor for microreactors. On the other hand, the cover glasses used as the dielectric were made from borosilicate glass. It is sometimes used in the technique of *anodic bonding*, in which Na^+ ions are diffused away from the anode, leaving oxygen ions available to diffuse to and react with the atoms in the material to bond to. Typical bonding conditions at atmospheric pressure are 10^2 V and $\lesssim 10^3$ K [Rogers and Kowal, 1995]. The current experimental conditions would therefore explain the dielectric breakdown and observed short-circuits. In [Dussart et al., 2010], MHCD arrays were operated in helium at high pressure. They all showed signs of thermal damage of the nickel film and had lifetimes of 10 minutes with direct current input between 1 and 20 mA. Their structure consisted of a nickel electrode "a few microns" thick, a 5-μm thick SiO_2 dielectric and a semiconducting silicon substrate. A blind cavity was etched, about 60 μm deep and 50 or 100 μm in diameter. Such reports about the durability of microplasma reactors are rare. And for most microplasma research reports with direct current, precautions are explicitly mentioned for limiting the thermal load on the reactors, such as pulsing the current. The thermal impact of microplasma operation is thus a serious though underinvestigated topic, and diamond proves promising.

Data reproducibility seems comparable in diamond- and glass-based reactors. In Fig. 5.9 p.118 each device maintained the V-I characteristic shape throughout its

total operating time. A voltage shift of little more than 50 V was observed for G-u-G and Ta-glass-Ta reactors, but significantly less than that for B-u-B. Nevertheless this was observed for the glass-based reactor over less than an hour, to be compared with between 3 and 14 hours for the other substrate material. The discrepancy between data obtained with identical devices was the subject of Fig. 5.10 p.120. It appeared to be of the same magnitude as it was for individual devices, with the notable exception of B-u-B reactors.

The striking dissimilarity of the V-I curves of B-u-B reactors (Fig. 5.10(b)) requires an explanation. The lack of experimental results for the S85 precludes a thorough comparison of their variability. But the difference can be understood from the difference in their fabrication. As emphasized in the previous chapter — Section 4.2 Diamond-Based Micro-Reactors — the CVD deposition of the semiconducting B-doped layer was an iterative process throughout the lifetime of this and the associated thesis by Monika Zeleznik (University of Bristol). Reactor S85 was produced nearly a year after S51, after an optimization of the process. Their specifications are also slightly different, with the following layer thicknesses:

- S51: 4 μm B-doped, 250 μm undoped, 4 μm B-doped diamond
- S85: 1.5 μm B-doped, 250 μm undoped, 1.5 μm B-doped diamond

From the point of view of microplasma operation, S85 is deemed an improvement over S51 thanks to its lower operating voltage. The two are therefore more appropriately considered similar than identical.

5.5 Summary

This chapter investigated the role of the dielectric through studies of the gas temperature during microplasma operation. The dielectric spacer is both structurally

critical and offers a plasma boundary with the highest surface to volume ratio. Material dependent phenomena were isolated through the comparative study of diamond- and glass-based micro-devices.

The neutral gas temperature increases with power but is also controlled by various other parameters. The thermal conductivity of the background gas affects the maximum temperature as well as its pressure. With increasing collisions, the temperature tends to increase as pressure rises from less than 100 to 760 torr. However as the microplasma expands out of the micro-cavity, convection and conduction are favoured, limiting the temperature-pressure dependence. The thermal conductivity of the dielectric also contributes to enhancing heat transfer out of the microdischarge. It was observed to be especially important the smaller the diameter.

The choice of dielectric also affects the durability of and data reproducibility by a microplasma device. Diamond-based reactors showed a high level of both and did not hint at any limit to their lifetime. Conversely, glass-based devices all terminated with failures, probably due to electrical breakdown of the dielectric at high temperature and voltage. The reproducibility with Ta-glass-Ta was comparable with G-u-G and B-u-B.

The superlative thermal properties of diamond seem to translate into extremely durable microplasma reactors. This represents serious potential by allowing more extensive microplasma research without worrying about the long-term reliability of the data. More replicable results will be beneficial to the scientific community as much as for technological applications. Its merits also lie in shedding light on the reliability of micro-reactors, more often discussed than published.

Chapter 6

CONCLUSION AND FUTURE WORK

The aim of this project was to characterize microdischarges inside diamond-based reactors. This was achieved in two phases:

1. comparing CVD diamond with common microplasma materials
2. studying the influence of CVD diamond on microplasma behaviour

For the first phase, electrical and optical results from micro-reactors having diamond as the dielectric and/or the electrode material were compared with data from the literature. The role of CVD diamond on microplasma operation was then studied via gas temperature measurements.

A summary of the findings and general conclusions are presented below, followed by suggestions for further work.

6.1 CVD Diamond vs. Other Materials

The initial motivation for this thesis' work was to characterize a microplasma inside a novel reactor material: insulating and semiconducting CVD diamond. This con-

cludes a consortium research project aimed at deciding if and how CVD diamond could become the next generation of microplasma reactor substrate[1]. The preliminary steps for creating the reactors described in this thesis were recently published in a thesis written concurrently by Monika Allen[2]:"Fabrication of diamond-based microplasma devices" [Allen, 2014]. Microdischarges were characterized inside the micro-devices provided by this student colleague from the University of Bristol and the first results published in [Mitea et al., 2012]. A further comparison with data obtained with more commonly used materials was conducted in this thesis. Two families of microhollow cathode discharges were fabricated and successfully operated for the first time by combining boron-doped and undoped diamond:

- boron doped – undoped – boron doped diamond (tagged B-u-B)
- gold – undoped diamond – gold (tagged G-u-G)

CVD diamond offers interesting flexibility as a microplasma substrate material. During deposition, obtaining a seminconducting thin film is as straightforward as injecting a few percent of diborane per volume of the carbon-containing gas mixture. The result is a p-type extrinsic semiconductor that can achieve metallic-type conduction with carrier mobility at least as favorable as silicon values. Among the other strengths of diamond are its very high breakdown voltage, beyond the MV/m and its superlative thermal conductivity and stability. Consequently, homogeneous electrode-dielectric-electrode sandwiches from the same material were made possible. This represents an advantage with respect to heterogenous structures that rely on a variety of materials and fabrication techniques [Park and Eden, 2003, Dussart et al., 2010].

A few challenges, some inherent to CVD diamond, were also identified from fabrication through to operation. Substrate contamination was countered by acid-

[1]Under the EPSRC grant EP/G057176/1.
[2]Monika Allen previously published as Monika Zeleznik.

cleaning prior to CVD deposition and careful handling with non-metallic tweezers throughout the device lifecycle. Contamination sources include organic material and metallic objects that can deposit conducting material when scraped off by the harder diamond. Unwanted conductive pathways along the surface and in the bulk of the reactors were combatted by masking the edges in the deposition chamber and making precautionary cut-outs after the deposition of the B-doped layer. For the addition of gold electrodes, titanium was required to ensure the stability of the interface with diamond. Finally, for fear of contamination such as graphitization resulting from laser-drilling of the microplasma hole, the reactors were cleaned off in either acid or an oxygen plasma. During operation, dielectric layers as thin as 5 μm or less appeared to favour device breakdown without microplasma ignition. As they were assumed to come from pinholes bridging the crystal, the insulating layers were from then on obtained commercially, with a thickness of 250 μm.

The ignition conditions observed in diamond-based devices were similar to those reported in the literature. The experimental Paschen curves matched those of comparable micro- and macro-discharges for G-u-G in argon and helium. However for B-u-B V_b was consistently overestimated, which was attributed to a contact resistance between the semiconductor and the mechanically pressed metal connector.

The V-I characteristics and optical diagnostics agreed well with results previously reported with other MHCD materials. At pressures up to about 500 torr, a steep positive slope at low current was followed by a nearly flat gradient beyond a threshold current. This was linked to an abnormal glow mode inside the hole turning to a normal glow mode upon expansion of the microplasma onto the cathode surface. Furthermore, the cylindrical glow at lower pressures was shown to become a radially asymmetric discharge at higher pressures. With enhanced ionization in the cathode sheath at higher pressure, the microplasma is drawn closer to the electrode.

This would magnify any local electric field non-uniformity due to a rough surface, explaining the asymmetry.

Interestingly, B-u-B reactors maintained a lower current density for an equivalent gas pressure. The lack of cathode material sputtering and an excellent thermal stability were used to explain these lower current densities. This would also explain the robustness of all-diamond devices to high current and absence of device breakdown caused by long operation.

To conclude the assessment of CVD diamond as a novel microplasma substrate material, our reactors have shown uncompromised robustness. In terms of lifetime, all of the devices reported here are still in good working condition after several hours total operation or beyond one hour continuous operation. Also useful for DC powered discharges, no protective measures against heat or plasma degradation were put in place, such as short pulses, sub-mA current limitation, gas flow,... As a material of choice for microfabrication like silicon, CVD diamond therefore seems better poised to endure the microplasma environment than the latter [Park et al., 2001, Dussart et al., 2010]. In this thesis, the durability of diamond surpassed that of glass. Only the latter consistently led to failures, apparently due to electrical breakdown of the dielectric at high temperature and voltage. Nevertheless, the reproducibility with Ta-glass-Ta sandwiches was comparable to that in G-u-G and B-u-B.

6.2 Influence of CVD Diamond on Microplasma

Neutral gas temperature measurements were used to study the influence of the substrate material on microplasma behaviour. Our first starting assumption was that heat transfer through the MHCD geometry would be driven by the dielectric; hav-

ing electrodes < 10 μm thick versus more than 200 μm for the dielectric. Another assumption was that the superlative thermal properties of diamond would lead to distinguishable result features. With that in mind, results were compared with those in glass; a material at the opposite end of the thermal conductivity spectrum. The neutral gas temperature increased with power but was further controlled by other experimental parameters.

The neutral gas temperature was shown to depend on the gas species and pressure. Argon consistently led to higher temperatures than helium, all else being equal. This was linked to the thermal conductivity and specific heat of argon being an order of magnitude smaller. With identical power inputs, increasing the pressure from 100 to 760 torr also increased the temperature. As more frequent momentum transfer collisions occur between the electrons and neutrals, Joule heating increases.

However pressure was not as effective at controlling temperature as the excursion of the microdischarge outside of its hole. Indeed, from the onset of microplasma expansion on the cathode surface, the temperature-pressure dependence weakened. This is consistent with an increase in the surface area for heat transfer to the surroundings.

Diamond favoured the departure from a pressure-controlled temperature increase. With CVD diamond as the dielectric substrate, heat transfer through the plasma-wall interface is enhanced. At higher power values, the temperature-pressure relationship was maintained in glass but decreased in diamond. Increasing the volume of gas/plasma would lead to a diminishing role of the solid-based heat exchanges. That is exactly what was observed in larger diameter diamond-based holes, yielding a steeper temperature-pressure gradient. The influence of the dielectric was further compounded by the observation of hotter gas the smaller the diameter for

glass-based reactors; whereas in diamond the smaller diameters gave lower temperatures. Therefore, gas temperature is controlled by gas phase phenomena in poor thermal conductors. Whereas very good thermal conductors compete with the gas phase for heat transfer.

A CVD diamond substrate maintains more favourable microplasma operating conditions and longer reactor lifetimes. Even though the discharges studies in this thesis are referred to as non-thermal, the microscopic dimensions and high surface-to-volume ratios magnify the impact of gas temperature on the reactors. In that respect, the better control of temperature by diamond was discussed above. On top of that, diamond-based reactors lasted longer, not even suffering a single operation induced failure. This can be linked to the very good thermal conductivity and stability of the material. But also, the use of a single material, in the case of B-u-B reactors, precludes any thermal mismatch between layers; a pursuit of the semiconductor industry in general.

6.3 Future Work

The microplasma research reported here opens up interesting opportunities for academic and societal enterprises.

6.3.1 Academic Research

CVD diamond lends itself well to more thorough studies of the link between reactor materials and microplasma behaviour. Studies of this link have been highlighted as strategic for further developments by the Microplasma community [Pitchford, 2011]. They can be hard to set up for several reasons, that could now be addressed following the validation of CVD diamond-based microplasma reactors:

- Microplasma results are hard to compare. The literature is rich in materi-

als, geometries, dimensions and other parameters that can hardly be directly compared, unless research groups developed or crafted their reactors together. With few fabrication steps and highly reproducible techniques from the semiconducting industry (for design, drilling and cutting, packaging), diamond CVD can produce a more standard set of micro-reactors that could be adopted by many research groups. In fact the current author enquired in a private discussion with N. St. J. Braithwaite (2012) about the appeal for a microscopic equivalent of the GEC RF Reference Cell, that has boosted the microelectronic research and industry since 1988 [Olthoff and Greenberg, 1995].

- Microplasma is contaminated. Micro-reactors can contain materials that can interfere with microplasma operation such as glue, leftovers from etch masks or sputtered electrodes. Reactors of the B-u-B family are both homogeneous in composition and resistant to sputtering, with the exception of oxygen-based plasma.

- The time and input power are limited by the reactor material. Although no extensive lifetime studies were conducted on the current CVD reactors, they show promising signs. In fact, a systematic lifetime study is a short-term research necessity in order to explore the full potential of diamond as a viable research platform.

Until such standardization is attained, further work based on the same two families of G-u-G and B-u-B devices could expand the range of parameters. Extending the range of power, gas types and dimensions would offer more overlap for comparing the results with similar devices in the literature. Moreover, it has been suggested inside our consortium that oxygen would be detrimental to the diamond, being the main source of CVD diamond etching. In the hope of operating unconfined atmospheric pressure microdischarges in air, it is essential that the right ratio of background gas to ambient air could be established by using oxygen containing mixtures.

The current diamond micro-devices can be upgraded for an enhanced research portfolio. Early in this research, our consortium postulated that an optical link could be built in during the diamond deposition process. Having established in this thesis the driving role of heat transfer through the dielectric, it would be interesting to correlate data from the dielectric region with electrical or other measurements. With several dielectric thicknesses hence several possible axial positions for the optical link, the temperature and discharge position could be more accurately described with respect to the separation from either electrode. This could represent a step towards benchmarking results by [Kushner, 2005] on the axial gas velocity inside MHCD's. The role of the dielectric could further be investigated by operating a larger set of devices based on the two families of G-u-G and B-u-B devices, changing only the diameter or the dielectric thickness.

6.3.2 Societal Impact

Diamond-based microplasma provides a way to facilitate academic research and enhance its societal impact; a keen interest to the current author. Having developed expertise in logistics in another career in the private sector, the availability and reliability of the first generation of diamond devices was the subject of particular concern and interest. Other research teams also reported limited device reliability during informal exchanges. Having demonstrated satisfactory robustness over the time span of one PhD, the reactors reported here could therefore offer a route to "guaranteed" research time and data to future researchers. Also, the portability and versatility of the same devices offer the possibility of turning this cutting-edge research tool into an appealing educational one. Through a business competition[3], a workshop[4] and various exchanges with start-up business support organizations in

[3]OU-EPSRC Commercial Challenge Competition 2012

[4]Enterprisers programme 2012, Judge Business School, University of Cambridge

Belgium (2012–2014), this author has been exploring how to package ready-to-use diamond-based microplasma reactors for both research and high school institutions. The aspiration behind this is to facilitate the basic research in microplasma to a wider academic audience and to bridge the gap between classroom-based education and scientific careers.

Bibliography

[kap, 2006] (2006). Summary of properties for Kapton® polyimide films. DuPont.

[Allen, 2014] Allen, M. (2014). *Fabrication of diamond-based microplasma devices.* PhD thesis, University of Bristol.

[Ashfold et al., 1994] Ashfold, M. N. R., May, P. W., Rego, C. A., and Everitt, N. M. (1994). Thin film diamond by chemical vapour deposition methods. *Chemical Society Reviews*, 23:21–30.

[Bachmann et al., 2001] Bachmann, P. K., van Elsbergen, V., Wiechert, D. U., Zhong, G., and Robertson, J. (2001). CVD diamond: a novel high γ-coating for plasma display panels? *Diamond and Related Materials*, 10(3–7):809–817.

[Bayram and Freamat, 2012] Bayram, S. B. and Freamat, M. V. (2012). Vibrational spectra of n_2: An advanced undergraduate laboratory in atomic and molecular spectroscopy. *American Journal of Physics*, 80(8):664–669.

[Becker et al., 2006] Becker, K. H., Schoenbach, K. H., and Eden, J. G. (2006). Microplasmas and applications. *Journal of Physics D: Applied Physics*, 39:R55–R70.

[Boeuf, 2003] Boeuf, J.-P. (2003). Plasma display panels: physics, recent developments and key issues. *Journal of Physics D: Applied Physics*, 36:R53–R79.

[Boeuf et al., 2005] Boeuf, J.-P., Pitchford, L. C., and Schoenbach, K. H. (2005). Predicted properties of microhollow cathode discharges in xenon. *Applied Physics Letters*, 86(7):071501–1–071501–3.

[Boyle and Kisliuk, 1955] Boyle, W. S. and Kisliuk, P. (1955). Departure from paschen's law of breakdown in gases. *Physical Review*, 97(2):255–259.

[Braithwaite, 2000] Braithwaite, N. S. J. (2000). Introduction to gas discharges. *Plasma Sources Science and Technology*, 9(4):517–527.

[Bruzzi, 2009] Bruzzi, M. (2009). *CVD Diamond for Electronic Devices and Sensors*, chapter 8 Diamond Radiation Sensors for Radiotherapy. Number ISBN 9780470065327. John Wiley & Sons.

[Butler et al., 2009] Butler, J. E., Cheesman, A., and Ashfold, M. N. R. (2009). *CVD Diamond for Electronic Devices and Sensors*, chapter 5 Recent Progress in the Understanding of CVD Growth of Diamond. Number ISBN 9780470065327. John Wiley & Sons.

[Chapman, 1980] Chapman, B. N. (1980). *Glow discharge processes: sputtering and plasma etching.* Number ISBN 0-471-07828-X. John Wiley & Sons, Inc.

[Dufour et al., 2008] Dufour, T., Dussart, R., Lefaucheux, P., Ranson, P., Overzet, L. J., Mandra, M., Lee, J.-B., and Goeckner, M. (2008). Effect of limiting the cathode surface on direct current microhollow cathode discharge in helium. *Applied Physics Letters*, 93(7):071508–1–071508–3.

[Dussart et al., 2010] Dussart, R., Overzet, L. J., Lefaucheux, P., Dufour, T., Kulsreshath, M., Mandra, M. A., Tillocher, T., Aubry, O., Dozias, S., Ranson, P., Lee, J. B., and Goeckner, M. (2010). Integrated micro-plasmas in silicon operating in helium. *The European Physical Journal D - Atomic, Molecular, Optical and Plasma Physics*, 60(3):601–608.

[Ferro, 2002] Ferro, S. (2002). Synthesis of diamond. *Journal of Materials Chemistry*, 12(10):2843–2855.

[Foest et al., 2006] Foest, R., Schmidt, M., and Becker, K. (2006). Microplasmas, an emerging field of low-temperature plasma science and technology. *International Journal of Mass Spectrometry*, 248:87–102.

[Frame et al., 1997] Frame, J. W., Wheeler, D. J., DeTemple, T. A., and Eden, J. G. (1997). Microdischarge devices fabricated in silicon. *Applied Physics Letters*, 71(9):1165–1167.

[Fridman and Kennedy, 2004] Fridman, A. and Kennedy, L. A. (2004). *Plasma Physics and Engineering.* Number ISBN 1-560-32848-7. Taylor & Francis.

[Friedl and Fantz, 2012] Friedl, R. and Fantz, U. (2012). Spectral intensity of the n 2 emission in argon low-pressure arc discharges for lighting purposes. *New Journal of Physics*, 14(4):043016.

[Garrido, 2009] Garrido, J. A. (2009). *CVD Diamond for Electronic Devices and Sensors*, chapter 16 Biofunctionalization of Diamond Surfaces: Fundamentals and Applications. Number ISBN 9780470065327. John Wiley & Sons.

[Gill and Webb, 1977] Gill, P. and Webb, C. E. (1977). Electron energy distributions in the negative glow and their relevance to hollow cathode lasers. *Journal of Physics D: Applied Physics*, 10(3):299–301.

[Go et al., 2009] Go, D. B., Fisher, T. S., Garimella, S. V., and Bahadur, V. (2009). Planar microscale ionization devices in atmospheric air with diamond-based electrodes. *Plasma Sources Science and Technology*, 18(3):035004–1–035004–10.

[Hagstrum, 1953] Hagstrum, H. D. (1953). Electron ejection from ta by he^{+}, he^{++}, and he_2^{+}. *Phys. Rev.*, 91:543–551.

[Hartmann and Johnson, 1978] Hartmann, G. and Johnson, P. C. (1978). Measurements of relative transition probabilities and the variation of the electronic transition moment for n_2 c $^3\pi_u$–b $^3\pi_g$ second positive system. *Journal of Physics B: Atomic and Molecular Physics*, 11(9):1597.

[Hayden and Utterback, 1964] Hayden, H. C. and Utterback, N. G. (1964). Ionization of helium, neon, and nitrogen by helium atoms. *Phys. Rev.*, 135:A1575–A1579.

[Herzberg, 1950] Herzberg, G. (1950). *Molecular spectra and molecular structure*, volume 1. Spectra of diatomic molecules. D. Van Nostrand Company, Inc., second edition.

[Incropera and DeWitt, 1996] Incropera, F. P. and DeWitt, D. P. (1996). *Fundamentals of heat and mass transfer.* Number ISBN 9780471304609. Wiley, fourth edition.

[Isberg, 2009] Isberg, J. (2009). *CVD Diamond for Electronic Devices and Sensors*, chapter 2 Transport Properties of Electrons and Holes in Diamond. Number ISBN 9780470065327. John Wiley & Sons.

[Iza et al., 2008] Iza, F., Kim, G. J., Lee, S. M., Lee, J. K., Walsh, J. L., Zhang, Y. T., and Kong, M. G. (2008). Microplasmas: Sources, particle kinetics, and biomedical applications. *Plasma Processes and Polymers*, 5:322–344.

[Karanassios, 2004] Karanassios, V. (2004). Microplasmas for chemical analysis: analytical tools or research toys? *Spectrochimica Acta Part B: Atomic Spectroscopy*, 59(7):909–928.

[Kasu, 2009] Kasu, M. (2009). *CVD Diamond for Electronic Devices and Sensors*, chapter 13 H-Terminated Diamond Field-Effect Transistors. Number ISBN 9780470065327. John Wiley & Sons.

[Kim et al., 2010] Kim, G. J., Kim, W., Kim, K. T., and Lee, J. K. (2010). DNA damage and mitochondria dysfunction in cell apoptosis induced by nonthermal air plasma. *Applied Physics Letters*, 96(2):021502.

[Kitsinelis, 2010a] Kitsinelis, S. (2010a). *Light Sources Technologies and Applications*, chapter 4: Electrical discharge lamps. Number ISBN 978-1-4398-2079-7. Taylor & Francis.

[Kitsinelis, 2010b] Kitsinelis, S. (2010b). *Light Sources Technologies and Applications*, chapter 3: Electrical Incandescent Light Sources. Number ISBN 978-1-4398-2079-7. Taylor & Francis.

[Kogelschatz et al., 2005] Kogelschatz, U., Akishev, Y. S., Becker, K. H., Kunhardt, E. E., Kogoma, M., Kuo, S., Laroussi, M., Napartovich, A. P., Okazaki, S., and Schoenbach, K. H. (2005). *Non-equilibrium air plasmas at atmospheric pressure*, chapter 6: DC and Low Frequency Air Plasma Sources. Number ISBN 0-7503-0962-8 in Series in plasma physics. Institute of Physics.

[Kulsreshath et al., 2012] Kulsreshath, M. K., Schwaederle, L., Overzet, L. J., Lefaucheux, P., Ladroue, J., Tillocher, T., Aubry, O., Woytasik, M., Schelcher, G., and Dussart, R. (2012). Study of dc micro-discharge arrays made in silicon using cmos compatible technology. *Journal of Physics D: Applied Physics*, 45(28):285202.

[Kunhardt, 2000] Kunhardt, E. (2000). Generation of large-volume, atmospheric-pressure, nonequilibrium plasmas. *Plasma Science, IEEE Transactions on*, 28(1):189 –200.

[Kushner, 2004] Kushner, M. J. (2004). Modeling of microdischarge devices: Pyramidal structures. *Journal of Applied Physics*, 95(3):846–859.

[Kushner, 2005] Kushner, M. J. (2005). Modelling of microdischarge devices: plasma and gas dynamics. *Journal of Physics D: Applied Physics*, 38(11):1633–1643.

[Lakits et al., 1990] Lakits, G., Aumayr, F., Heim, M., and Winter, H. (1990). Threshold of ion-induced kinetic electron emission from a clean metal surface. *Phys. Rev. A*, 42:5780–5783.

[Langmuir, 1928] Langmuir, I. (1928). Oscillations in Ionized Gases. *Proceedings of the National Academy of Sciences of the United States of America*, 14(8):627–637.

[Lazzaroni et al., 2010] Lazzaroni, C., Chabert, P., Rousseau, A., and Sadeghi, N. (2010). The excitation structure in a micro-hollow cathode discharge in the normal regime at medium argon pressure. *Journal of Physics D: Applied Physics*, 43(12):124008.

[Lee et al., 2009] Lee, H. J., Shon, C. H., Kim, Y. S., Kim, S., Kim, G. C., and Kong, M. G. (2009). Degradation of adhesion molecules of G361 melanoma cells by a non-thermal atmospheric pressure microplasma. *New Journal of Physics*, 11(11):115026 (13pp).

[Lewin, 1965] Lewin, S. Z. (1965). Luminous gas light sources. *Journal of Chemical Education*, 42(3):A165.

[Lieberman and Lichtenberg, 2005] Lieberman, M. and Lichtenberg, A. (2005). *Principles of plasma discharges and materials processing.* Wiley-Interscience, second edition.

[Llewellyn Jones and Morgan, 1951] Llewellyn Jones, F. and Morgan, C. G. (1951). Failure of paschen's law and spark mechanism at high pressure. *Physical Review*, 82(6):970–971.

[Lu et al., 2008] Lu, M., Park, S.-J., Cunningham, B. T., and Eden, J. G. (2008). Low temperature plasma channels generated in microcavity trenches with widths of 20–150 mu m and aspect ratios as large as 10[sup 4]:1. *Applied Physics Letters*, 92(10):101928.

[Matsunaga et al., 2003] Matsunaga, Y., Kato, T., Hatori, T., and Hashiguchi, S. (2003). Evaluation of improved efficiency with a diamond coating for a plasma display panel electrode. *Journal of Applied Physics*, 93(9):5043–5052.

[May et al., 2008] May, P. W., Ludlow, W., Hannaway, M., Heard, P., Smith, J., and Rosser, K. (2008). Raman and conductivity studies of boron-doped microcrystalline diamond, facetted nanocrystalline diamond and cauliflower diamond films. *Diamond and Related Materials*, 17(2):105–117.

[Mitea et al., 2012] Mitea, S., Zeleznik, M., Bowden, M. D., May, P. W., Fox, N. A., Hart, J. N., Fowler, C., Stevens, R., and Braithwaite, N. S. J. (2012). Generation of microdischarges in diamond substrates. *Plasma Sources Science and Technology*, 21(2):022001.

[Morfill et al., 2009] Morfill, G. E., Kong, M. G., and Zimmermann, J. L. (2009). Focus on plasma medicine. *New Journal of Physics*, 11(11):115011 (8pp).

[Moselhy and Schoenbach, 2004] Moselhy, M. and Schoenbach, K. H. (2004). Excimer emission from cathode boundary layer discharges. *Journal of Applied Physics*, 95(4):1642–1649.

[Noma et al., 2008] Noma, Y., Choi, J. H., Tomai, T., and Terashima, K. (2008). Gas-temperature-dependent generation of cryoplasma jet under atmospheric pressure. *Applied Physics Letters*, 93(10):101503.

[Olthoff and Greenberg, 1995] Olthoff, J. K. and Greenberg, K. E. (1995). The gaseous electronics conference rf reference cell — an introduction. *Journal of Research of the National Institute of Standards and Technology*, 100(4):327–339.

[Park et al., 2001] Park, S.-J., Chen, J., Liu, C., and Eden, J. G. (2001). Silicon microdischarge devices having inverted pyramidal cathodes: Fabrication and performance of arrays. *Applied Physics Letters*, 78(4):419–421.

[Park and Eden, 2003] Park, S.-J. and Eden, J. (2003). Electrical characteristics and lifetimes of microdischarge devices having thin dielectric films of aluminum oxide,boron nitride, or barium titanate. *Electronics Letters*, 39(10):773–775.

[Park et al., 2004] Park, S.-J., Eden, J. G., and Park, K.-H. (2004). Carbon nanotube-enhanced performance of microplasma devices. *Applied Physics Letters*, 84(22):4481–4483.

[Park et al., 2000] Park, S.-J., Wagner, C. J., Herring, C. M., and Eden, J. G. (2000). Flexible microdischarge arrays: Metal/polymer devices. *Applied Physics Letters*, 77(2):199–201.

[Paschen, 1916] Paschen, F. (1916). Bohrs Heliumlinien. *Annalen der Physik*, 355(16):901–940.

[Penache et al., 2002] Penache, C., Miclea, M., Bräuning-Demian, A., Hohn, O., Schössler, S., Jahnke, T., Niemax, K., and Schmidt-Böcking, H. (2002). Characterization of a high-pressure microdischarge using diode laser atomic absorption spectroscopy. *Plasma Sources Science and Technology*, 11(4):476.

[Petrović et al., 2008] Petrović, Z. L., Škoro, N., Marić, D., Mahony, C. M. O., Maguire, P. D., Radmilović-Raenović, M., and Malović, G. (2008). Breakdown, scaling and volt–ampere characteristics of low current micro-discharges. *Journal of Physics D: Applied Physics*, 41(19):194002.

[Pitchford, 2011] Pitchford, L. C. (2011). Oral presentation. In *6th International Workshop on Microplasmas (IWM), 3-6th April, Paris, France.*

[Portsel et al., 2009] Portsel, L. M., Lodygin, A. N., and Astrov, Y. A. (2009). Townsend-like discharge: the suppression of instabilities by a semiconductor electrode. *Journal of Physics D: Applied Physics*, 42(235208):1–9.

[Revel et al., 2000] Revel, I., Pitchford, L. C., and Boeuf, J.-P. (2000). Calculated gas temperature profiles in argon glow discharges. *Journal of Applied Physics*, 88(5):2234.

[Rogers and Kowal, 1995] Rogers, T. and Kowal, J. (1995). Selection of glass, anodic bonding conditions and material compatibility for silicon-glass capacitive sensors. *Sensors and Actuators A: Physical*, 46(1–3):113–120.

[Schoenbach et al., 1997] Schoenbach, K. H., El-Habachi, A., Shi, W., and Ciocca, M. (1997). High-pressure hollow cathode discharges. *Plasma Sources Science and Technology*, 6(4):468–477.

[Schoenbach et al., 1996] Schoenbach, K. H., Verhappen, R., Tessnow, T., Peterkin, F. E., and Byszewski, W. W. (1996). Microhollow cathode discharges. *Applied Physics Letters*, 68(1):13–15.

[Schwaederlé et al., 2012] Schwaederlé, L., Kulsreshath, M. K., Overzet, L. J., Lefaucheux, P., Tillocher, T., and Dussart, R. (2012). Breakdown study of dc silicon micro-discharge devices. *Journal of Physics D: Applied Physics*, 45(6):065201.

[Shi et al., 1999] Shi, W., Stark, R., and Schoenbach, K. H. (1999). Parallel operation of microhollow cathode discharges. *IEEE Transactions on Plasma Science*, 27(1):16–17.

[Sismanoglu and Amorim, 2008] Sismanoglu, B. N. and Amorim, J. (2008). Microhollow cathode discharge and breakdown in micron separations. *The European Physical Journal - Applied Physics*, 41(2):165–172.

[Sismanoglu et al., 2010] Sismanoglu, B. N., Grigorov, K. G., Caetano, R., Rezende, M. V., and Hoyer, Y. D. (2010). Spectroscopic measurements and electrical diagnostics of microhollow cathode discharges in argon flow at atmospheric pressure. *The European Physical Journal D - Atomic, Molecular, Optical and Plasma Physics*, 60(3):505–516.

[Slade and Taylor, 2002] Slade, P. and Taylor, E. (2002). Electrical breakdown in atmospheric air between closely spaced (0.2 mu;m-40 mu;m) electrical contacts. *Components and Packaging Technologies, IEEE Transactions on*, 25(3):390–396.

[Sussmann, 2009] Sussmann, R. S., editor (2009). *CVD Diamond for Electronic Devices and Sensors*. Number ISBN 9780470065327. John Wiley & Sons.

[Sutton, 2011] Sutton, Y. (2011). *Electro-acoustic coupling in a plasma gas*. PhD thesis, The Open University.

[Tachibana, 2006] Tachibana, K. (2006). Current status of microplasma research. *IEEJ Transactions on Electrical and Electronic Engineering*, 1(2):145–155.

[Townsend, 1900] Townsend, J. S. (1900). The conductivity produced in gases by the motion of negatively-charged ions. *Nature*, 62(1606):340–341.

[Wang et al., 2007] Wang, Q., Doll, F., Donnelly, V. M., Economou, D. J., Sadeghi, N., and Franz, G. F. (2007). Experimental and theoretical study of the effect of gas flow on gas temperature in an atmospheric pressure microplasma. *Journal of Physics D: Applied Physics*, 40(14):4202.

[Wörner et al., 1996] Wörner, E., Wild, C., Müller-Sebert, W., Locher, R., and Koidl, P. (1996). Thermal conductivity of cvd diamond films: high-precision, temperature-resolved measurements. *Diamond and Related Materials*, 5(6–8):688–692. Proceedings of the 6th European Conference on Diamond, Diamond-like and Related Materials Part 2.